Correcting multiyear sea ice concentration estimates from microwave satellite observations with air temperature, sea ice drift and dynamic tie points

Dissertation zur Erlangung des akademischen Grades

Doktor der Naturwissenschaften (Dr. rer. nat.)

dem Fachbereich für Physik und Elektrotechnik

der Universität Bremen

vorgelegt von

Yufang YE

geb. in Ganzhou, China

May 20, 2016

1. Reviewer: Prof. Justus Notholt

2. Reviewer: Prof. Thomas Jung

Declaration

I, Yufang YE, declare that this thesis titled, "Correcting multiyear sea ice concentration estimates from microwave satellite observations with air temperature, sea ice drift and dynamic tie points" and the work presented in it are my own. I confirm that Chapters 5 to 7 are adapted from the following three manuscripts.

- **Chapter 5:** Ye, Y. and G. Heygster (2015). "Arctic Multiyear Ice Concentration Retrieval from SSM/I Data Using the NASA Team Algorithm with Dynamic Tie Points". In: *Towards an Interdisciplinary Approach in Earth System Science: Advances of a Helmholtz Graduate Research School*. Ed. by G. Lohmann et al. Cham, Germany: Springer International Publishing Switzerland, pp. 99-108.

- **Chapter 6:** Ye, Y., G. Heygster, and M. Shokr (2016). "Improving multiyear ice concentration estimates with reanalysis air temperatures". In: *Geoscience and Remote Sensing, IEEE Transactions on* 54.5. pp. 2602-2614.

- **Chapter 7:** Ye, Y. et al. (2016). "Improving multiyear sea ice concentration estimates with sea ice drift". In: *Remote Sensing* 8.5, pp. 397.

Abstract

Arctic sea ice cover is an important component of the global climate system and at the same time a sensitive climate indicator. Its area has decreased dramatically in the Arctic over the past three decades. The decrease is most pronounced in September when the annual sea ice minimum occurs, and particularly so for the area of multi-year ice (MYI), i.e. ice which has survived at least one summer. MYI strongly differs from first-year ice (FYI) in physical, radiative and dynamic properties. Spatial distribution of MYI in the Arctic is required for climate modeling, numeric weather forecast and sea ice prediction. The MYI distribution has been retrieved based on microwave satellite observations. However, the retrieval shows flaws under specific weather conditions. The current thesis is motivated by the need of better MYI estimates and introduces three methods to improve and correct the MYI concentration estimates from microwave satellite observations.

The first method builds upon the NASA Team algorithm and uses dynamic tie points to compensate the temporal variations of tie points (typical brightness temperatures of each surface type at all the channels). MYI concentrations are retrieved with the original and modified NASA Team algorithm with the Special Sensor Microwave Imager (SSM/I) data in winters (October-May) of the years 1989–2012. The method with dynamic tie points yields higher estimates in most years. Both methods show a clearly declining trend of the MYI area from 1989 to 2012. Furthermore, the MYI area in most years decreases within each winter, reflecting the loss of MYI by export and deformation to lower latitudes. This study shows that the MYI concentration retrieval with the NASA Team algorithm is most sensitive to the tie points of MYI and FYI at $19\,\mathrm{GHz}$ vertical polarized channel. These tie points need to be determined more accurately if dynamic tie points are used.

The second and third methods are two correction schemes used to account for radiometric anomalies that trigger the erroneous MYI concentration retrievals from microwave satellite observations. The second correction is based on air temperature

records. It is introduced to restore the underestimated MYI concentration under warm conditions. The third correction is mainly based on ice drift records. It is introduced to correct the overestimated MYI concentrations that are impacted by factors such ice deformation, snow wetness and metamorphism.

Warm-cold air temperature cycles trigger wet-dry cycles of the snow on MYI surface, leading to anomalous brightness temperature and backscatter from MYI, which are similar to those from FYI. The retrieved MYI concentrations are therefore underestimated under such conditions. The second correction utilizes the fact that the warm spell in autumn lasts for a short period of time (a few days) and replaces the erroneous MYI concentrations with interpolated ones. It is applied to MYI concentration retrievals from the Environment Canada Ice Concentration Extractor (ECICE) using inputs from QuikSCAT and the Advanced Microwave Scanning Radiometer-Earth Observing System (AMSR-E) data, acquired over the Arctic region in a series of autumn seasons (September-December) from 2003 to 2008. The correction works well by identifying and correcting anomalous MYI concentrations. For September of the six years, it introduces over 1.0×10^5 km^2 MYI area except for 2005, when there are less warm air spells.

Factors such as ice deformation, snow wetness and metamorphism can cause significant changes in brightness temperature and backscatter, leading to misidentification of FYI as MYI, hence increasing the retrieved MYI concentrations suddenly. The third correction utilizes ice drift records to constrain the MYI changes within a predicted contour and uses two thresholds of passive microwave radiometric parameters to account for snow wetness and metamorphism. It is applied to MYI concentration retrievals from ECICE over the Arctic in winters (October-May) from 2002 to 2009. Qualitative comparison with Radarsat-1 SAR images and quantitative comparison against results from previous studies show that the correction works well by removing the anomalous high MYI concentrations. On average, the correction reduces 5.2×10^5 km^2 of the estimated MYI area in the Arctic except for the April-May time frame, when the reduction is larger as the warmer weather prompts the condition of the anomalous snow

radiometric signatures.

Both corrections can be used as post-processings to any the microwave-based MYI concentration retrieval algorithm. Due to the regional effect of weather conditions, they could be important in operational applications. In addition, both corrections take the spatial and temporal continuity of MYI into account, which gives a new insight that instantaneous observations alone of sea ice may lead to ambiguities in determination of partial ice concentrations. This approach may be applicable to the retrieval of other sea ice parameters as well.

Contents

Chapter 1

Introduction

1.1 Motivation and goals of the study

Arctic sea ice is an important component of the global climate system and at the same time a sensitive climate indicator (Vihma, 2014). On one hand, sea ice covers sea surface and is the barrier between the ocean and the atmosphere. It prevents the exchange of heat, momentum, water vapour, and other material between the atmosphere and ocean. On the other hand, because of its high albedo, sea ice reflects most of the solar radiation, leading to low temperature of the sea ice surface. When temperatures decrease, the sea ice extent increases. It leads to increasing surface albedo thus reinforces the cooling. This positive ice-albedo feedback works in the opposite direction as well. When air temperature increases, sea ice starts to melt, and more solar radiation is absorbed, which makes the air temperature increase in turn. Therefore, a small increase in air temperature can lead to significant global warming (Wadhams, 2000). It has been found that the climate change in terms of surface air temperature increases in the Arctic has been at least twice as fast as the global coverage (Blunden and Arndt, 2012).

Arctic sea ice extent has decreased by over 4% per decade from 1979 to 2010 (Cavalieri and Parkinson, 2012), while the declining rate for the multiyear ice (MYI), ice that survives at least one summer melt, is much larger, $10 - 15\%$ per decade in the past three decades (Comiso, 2012; Comiso et al., 2008; Stroeve et al., 2007; Comiso, 2002; Johannessen, Shalina, and Miles, 1999). In late 1970s, MYI occupied two thirds

of the Arctic Basin. Now this ratio has reversed, large parts of the MYI has been replaced by the increasingly dominated thin first-year ice (FYI) (Kwok, 2007; Kwok and Untersteiner, 2011), leading to a rapidly changing Arctic marginal ice zone, which has cascading effects in the Arctic biogeochemical cycles and marine ecosystems (Barber et al., 2015). The reversal in the ratio of ice types area impacts the weather and climate through different radiation and dynamic properties, which has consequences for the Arctic and also for mid-latitude regions (Perovich and Richter-Menge, 2009; Vihma, 2014; Overland et al., 2015; Petrie, Shaffrey, and Sutton, 2015).

During summer in the Arctic, seasonal ice that is thick enough can survive the melt and turn to MYI. This ice replenishes the reservoir of MYI that was depleted by ice export and summer melt. From 2005 to 2008, the Arctic MYI area has decreased drastically by 42% (Kwok et al., 2009), but the decline is not monotonic during the past decade. The reduction of MYI area leads to increases in heat and mass exchanges between the ocean and the atmosphere. When MYI melts, it releases freshwater to the ocean, which alters the ocean stratification. More replenishment of thinner ice (young ice(YI) and FYI) is expected. Thinner ice is more liable to deform and melt and therefore allows larger heat and moisture flux exchange with the atmosphere (Stroeve et al., 2012). This ice also allows greater mobility of the ice in the Arctic Basin. Positive trends of ice drift speed are common in regions with decreased MYI cover (Kwok, Spreen, and Pang, 2013). Today, in years with enhanced MYI export out of the Arctic the exported MYI cannot be replenished during the following winters and this, in turn, allows more opening and mobility of the remaining ice. This positive feedback mechanism results in even less MYI coverage over the years in the northern polar seas (Notz, 2009; Shokr and Dabboor, 2013; Haas and Howell, 2015). In addition, thinner ice is easier to fracture under wind forcing, giving rise to formation of leads and cracks. All these factors may lead to a different composition of the Arctic sea ice as the trend of MYI decrease and its replenishment with FYI continues. From the climate point of view, it has become critical to estimate the area of these two sea ice categories accurately. A physically consistent MYI time series is needed to ascertain trends of climate change.

Accurate information of MYI at small and meso-scale is also important for marine operational applications. As marine activities are expected to increase along the Northwest Passage that passes through the Canadian Arctic Archipelago (CAA) and the Beaufort Sea, information about MYI in these regions is becoming increasingly required for oil and gas exploration as well as for other natural resources exploitation. Based on the results presented in Howell et al., (2013), the MYI flow in the CAA has increased since 2005 due to the increase of open water area in the region, which provided more leeway for the MYI inflow from the central Arctic. This should also lead to more migration of MYI from the central Arctic to lower latitudes, and that would be another reason, in addition to the warming trend of the Arctic environment, to decrease the MYI area in the central region.

For more than three decades, sea ice has been monitored with microwave satellite observations, e.g., radiometers and scatterometers. Total sea ice concentration (i.e. combining all ice types) can be derived reliably from microwave remote sensing data due to the distinct difference of microwave signatures between open water and sea ice. However, the discrimination of ice types (including MYI) poses difficulties. Brightness temperature and backscatter observations are influenced by key factors of ice surface and snow cover properties such as temperature, salinity, surface roughness, snow moisture content, and changes in snow grain structure. These factors are triggered by meteorological events, particularly warm and cold spells. Other wind-driven factors influenced by the mobility of floating ice include surface roughness and ice deformation. All these factors impact the observed microwave observations in ways that cause significant temporal and spatial variability as well as overlap of brightness temperature and backscatter between different surface types (i.e. ice types with different snow cover) under different meteorological and oceanic conditions. Consequently, this results in ambiguities in estimating concentration of certain ice types, including MYI, which is the subject of this study.

In order to improve the MYI concentration estimates from microwave satellite observations, we have made our efforts from the following aspects: (1) using a retrieval

algorithm that takes account of the variability of tie points (typical radiometric values for each surface type and each radiometric parameter), (2) using microwave scatterometer data along with the radiometer data, which could complement each other when defining ice types, and (3) applying correction schemes to account for the anomalous changes of microwave signature, e.g., under warm air temperature.

1.2   Thesis outline

The thesis is outlined as follows. Chapters 2 to 4 provide the background information necessary for the three main studies that are presented in Chapters 5 to 7. Chapter 8 summarizes the main results and conclusions of the thesis and gives an outlook for future research.

In Chapter 2 an introduction of sea ice formation, sea ice classes along with the physical properties is presented. Additionally, the physical basis for passive and active microwave remote sensing is introduced. Typical microwave signatures and scattering of different ice types are also described based on the physical and dielectric properties. Chapter 3 describes the data used in this work. Chapter 4 presents the algorithms that are commonly used for MYI concentration estimation from microwave remote sensing observations.

In Chapter 5, a modified NASA Team algorithm with dynamic tie points is used to retrieve MYI concentration from SSM/I data. The dynamic tie points are derived daily from the selected samples to account for the temporal variability of tie points. Results from this method are compared with those from the original NASA Team algorithm. A sensitivity study of the tie points is also presented.

Chapter 6 presents a correction scheme to restore the underestimated MYI concentration under warm conditions. The correction is based on air temperature records. It utilizes the fact that warm spell in autumn lasts for a short period of time (a few days), and replaces the underestimated ones with interpolated values. Chapter 7 presents another correction scheme to correct the overestimated MYI concentration under certain

conditions. This correction utilizes ice drift records to constrain the MYI concentration changes within a predicted contour and uses threshold on two passive microwave radiometric parameters to account for snow wetness and metamorphism. These two corrections are applied to the MYI concentration retrievals from the Environment Canada Ice Concentration Extrator (ECICE) using inputs from QuikSCAT and AMSR-E observations, acquired over the Arctic in a series of winter seasons (October to May) from 2002 to 2009. In addition, the Radarsat-1 SAR images and results from previous studies are used to qualitatively evaluate the performance of the corrections. Finally, Chapter 8 presents the conclusions and outlook of the thesis.

Chapter 2

Fundamentals

2.1 Sea ice formation

Sea ice arises when seawater freezes. The freezing of seawater differs from that of freshwater in two ways due to the inclusion of salt (Tucker et al., 1992). First, salt depresses the freezing temperature of seawater as a function of the salinity of water (Neumann and Pierson Jr, 1966; Pickard and Emery, 1990; Steele, Thorpe, and Turekian, 2009; Talley, 2011). The freezing temperature decreases from $0\,°C$ at a salinity of $0‰$ to $-1.8\,°C$ at $34‰$ (approximately the salinity of the Arctic Ocean). Second, the temperature for the maximum density of seawater is lower than the freezing temperature when the salinity is above $24.7‰$. When temperature is approaching the freezing point (cooling of seawater), density of seawater increases, leading to convective overturning. Due to the oceanic density, this convection is limited to a relatively shallow layer. The well-mixed layer, about $10 - 40$ m thick (Doronin and Kheisin, 1977), must cool to the freezing point before freezing begins.

Formation and growth of sea ice includes three main stages (Shokr and Sinha, 2015): (1) initial formation when minute ice crystals are nucleated in the seawater and grow sufficiently to recognizable sizes and shapes in the form of needles or tiny discs, called frazil ice, (2) lateral growth of the spicular crystals to form small rounded discs or flat patches, and coagulation of crystals to form a soupy layer on the surface, known as grease ice, (3) vertical growth or ice congelation.

2.2   Sea ice classes

There are different sets of sea ice classes based on the criteria. The criteria include ice thickness, ice form, ice concentration, and ice surface (Shokr and Sinha, 2015). Among them, ice thickness, which is associated with ice age, is most commonly used for operational ice monitoring and climate-related purposes. As described in Chapter 2.1, vertical growth of ice is an important stage in sea ice formation. The thickness-based ice classification system has been developed by the World Meteorological Organization (WMO) and also known as the system based on the stage of ice development. Table 2.1 (adapted from Shokr and Sinha, (2015)) shows the main stages of ice development, within which various subtypes exist, depending on the internal structure of the ice.

TABLE 2.1: Sea ice types based on stage of ice development.

Stage of development	Subtype	Definition	Thickness
New ice	Frazil	Fine spicules suspended in water.	
	Grease	Crystals have coagulated to form a soupy layer.	
	Slush	Snow mixed with water on ice surface after heavy snowfall.	
	Shuga	Accumulation of spongy white ice lumps formed from grease ice.	
Nilas	Dark nilas	A thin elastic crust of ice. Dark in color.	$< 5\,\text{mm}$
	Light nilas	Lighter in color.	$> 5\,\text{mm}$
Young ice (YI)	Grey	Less elastic than nilas, usually rafts under pressure.	$0.1 - 0.15\,\text{m}$
	Grey-white	It is more likely to ridge than to raft under pressure.	$0.15 - 0.3\,\text{m}$
First-year ice (FYI)	Thin FYI	Sea ice of not more than one winter growth, developing from YI	$0.3 - 0.7\,\text{m}$
	Medium FYI		$0.7 - 1.2\,\text{m}$
	Thick FYI		$1.2 - 2\,\text{m}$
Old ice	Second-year ice	Ice survived one summer melt.	
	Multiyear ice (MYI)	Ice survived more than one summer melt.	

In most microwave remote sensing studies (Cavalieri, Gloersen, and Campbell, 1984; Steffen and Schweiger, 1991; Lomax, Lubin, and Whritner, 1995; Comiso et al.,

1997; Kwok, 2004; Wang et al., 2009; Ye and Heygster, 2015), sea ice is categorized into two ice types: first-year ice (FYI) and multiyear ice (MYI), where MYI is defined as the ice that has survived at least one summer. In some other studies (Shokr, Lambe, and Agnew, 2008), there is another ice category studied: young ice (YI). Additionally, there are studies (Comiso, 2006b) categorizing sea ice into FYI, second-year ice (SYI), and MYI, where the definition of SYI and MYI is as described in Table 2.1. Some studies (Comiso, 2002; Nghiem et al., 2006; Stroeve et al., 2007) use the term perennial ice to represent old ice as defined in Table 2.1 (including SYI and MYI), while seasonal ice means new ice, YI, FYI and their sub-types. All the studies presented in this thesis use the former definition of MYI.

2.3 Physical properties of sea ice

The physical properties of sea ice are the basis to detect it with microwave remote sensing. As to be described in Chapter 2.4, emissivity is the electromagnetic characteristic of interest for passive microwave remote sensing. It is a function of reflectivity and scattering (Tucker et al., 1992). The reflectivity depends on the dielectric properties, which are functions of the distribution of brine, air, and solid salt within the sea ice. Scattering depends on the surface roughness, inhomogeneities within the ice, and the dielectric constant. Active microwave sensors measure the backscatter, which is determined by surface and volume scattering, and again depends on the roughness and spatial variation of the dielectric properties (Tucker et al., 1992).

Physical properties of sea ice differ with ice types. In general, MYI is thicker than FYI. Arctic FYI grows to a maximum thickness of about 2 m in one winter, while the equilibrium thickness of undeformed MYI is $3 - 4$ m (Maykut and Untersteiner, 1971), although the thickness of MYI varies greatly. Additionally, the surface appearances of FYI and MYI are quite different. Undeformed FYI is flat with little freeboard. After deformation, ridges of FYI consist of distinct angular blocks. In contrast, MYI typically has a rolling hummocky appearance. Even undeformed MYI has a surface relief of

$10 - 20$ cm due to the differential melting. Ridges of MYI are distinct from those of FYI since the former are weathered and rounded, with little or no sign of the original block structure evident. The major differences of physical properties between FYI and MYI are in salinity, crystal texture, and porosity. MYI is much less saline and contains more air bubbles of considerably larger size than in FYI. Unlike FYI, salinity of MYI is nearly constant with values of $0 - 2$‰. For FYI, the bulk salinity (i.e. the average salinity over the entire thickness of ice) is significantly high at the initial stage of formation, and decreases at a relatively high rate during the early ice growth (Nakawo and Sinha, 1981) then at a rather low rate. In Shokr and Sinha, (1994) and Shokr and Sinha, (1995), the authors introduced a scenario of bubble formation in MYI, which was later confirmed by Perovich and Gow, (1996). They explained that the air bubbles at or near the surface of MYI are formed from the remaining of water drainage channels established in the summer, which means that the origin of air bubbles in MYI are from the evolution of the brine pockets during the transition from FYI to MYI.

To sum up, MYI is characterized by its low salinity, density, surface and sub-surface temperatures, thermal conductivity, and dielectric constant. The properties of MYI are almost independent of weather conditions, although these conditions highly affect the snow cover, which influences the radiometric properties. For seasonal ice, the physical properties depend not only on the ice age but also on the history of ice formation and deformation, and most importantly on the current atmospheric temperatures. The properties of four ice types can be roughly estimated according to the values summarized in Shokr and Sinha, (2015) (shown in Table 2.2). However, there is a wide range of each parameter under different meteorological, oceanic, and climatic conditions.

TABLE 2.2: Typical physical and electrical properties of four ice types.

	New ice	Young ice	First-year ice	Multiyear ice
Thickness (m)	< 0.1	$0.1 - 0.3$	> 0.3	> 2.0
Bulk salinity (‰)	14	9	4	0.5
Density (kg/m^3)	920	900	900	$750 - 910$
Dielectric constant (10 GHz)	$5.65 - j2.25$	$4.0 - j0.81$	$3.32 - j0.23$	$2.77 - j0.03$
Thermal conductivity (W/m·K)	2.14	2.14	2.09	1.88
Brine volume fraction	0.20	0.08	0.05	0.0

2.4 Physical basis for microwave remote sensing

2.4.1 Physical basis for microwave sensors

The physical basis for microwave remote sensing of sea ice is the interaction of microwaves with the sea ice layer (Hallikainen and Winebrenner, 1992). The two main instruments for microwave remote sensing are radiometer and radar.

Radiometers are passive microwave sensors. They measure the radiation emitted and reflected by the target. According to the Planck equation, the radiation flux density $R_B(f)$ from a black body at a given frequency f and physical temperature T (in Kelvin) is expressed as

$$R_B(f) = \frac{2hf^3}{c^2} \left[\frac{1}{e^{hf/kT} - 1} \right], \tag{2.1}$$

where h is Planck's constant, k is Boltzmann's constant, and c is the speed of light. In the range of microwave frequencies ($1 - 300$ GHz), $hf/kT \ll 1$ and the Planck equation can be well approximated by the first-order Taylor polynomial, which is known as Rayleigh-Jean equation:

$$R_B(f) = \frac{2hkTf^2}{c^2}. \tag{2.2}$$

For a grey body, the radiation flux density $R_G(f)$ is a portion of that from the black body $R_B(f)$, determined by the emissivity e. Equation 2.2 can be therefore written as a linear relationship between the brightness temperature $T_b = c^2 R_G(f)/2hkf^2$ and the

physical temperature T of the radiating layer of sea ice:

$$T_b(p, f) = e(p, f) \cdot T, \tag{2.3}$$

where the emissivity e is dependent on the polarization p and frequency f.

In active microwave remote sensing, there are three types of radar systems: imaging radar, profile radar (scatterometer), and radar altimeter. The antenna of the monostatic radar system transmits radar pulses and receives the backscatter. The received power is related to the transmitted power through the radar equation (Ulaby, Moore, and Fung, 1982; Ulaby, Moore, and Fung, 1986). The result is expressed as the differential backscatter coefficient σ^0 (referred to as backscatter coefficient).

The backscatter coefficient σ^0 is defined in terms of the incident and scattered electric fields E_t^i and E_r^s:

$$\sigma_t^0 r(\theta_i, \phi_i) = \frac{4\pi R^2 |E_r^s|^2}{A|E_t^i|^2}, \tag{2.4}$$

where t and r are the polarizations of the transmitted and received field, respectively; R is the distance from the antenna to the target; and A is the effective aperture of the antenna. Angles θ_i and ϕ_i define the incident direction of the transmitted power. The backscatter coefficient is determined by the surface roughness, the physical and electrical properties of the scattering elements, as well as the radar parameters, including the wavelength, polarization, and the incident angle. Since values of σ^0 are usually very small, they are expressed in decibels using the equation:

$$\sigma^0(dB) = 10 \log_{10} \sigma^0. \tag{2.5}$$

2.4.2 Definition of electromagnetic quantities

The dielectric properties of sea ice determine the microwave emission and scattering. The complex dielectric constant is defined as

$$\epsilon = \epsilon' - j\epsilon''. \tag{2.6}$$

The real part ϵ' is the permittivity, whereas the imaginary part ϵ'' is the loss factor, which is a function of the electrical conductivity. Generally speaking, permittivity determines the percentage of energy penetrating the material (the rest will be scattered off the surface), while electrical conductivity determines the portion of energy that is lost as heat or scattering inside the material (Shokr and Sinha, 2015). Higher permittivity indicates less penetration of energy (hence more reflection/scattering at the surface), while larger loss factor means more energy dissipation inside the material.

For an electromagnetic plane wave propagating in the $z-$direction, the intensity of the electromagnetic field at point z can be written as

$$E(z) = E(0) \cdot \exp(-\gamma z), \tag{2.7}$$

where $E(0)$ is the field intensity at $z = 0$. The complex propagation constant γ of a medium is given by

$$\gamma = \alpha + j\beta, \tag{2.8}$$

with $\alpha = k_0 \|\Im(\sqrt{\epsilon})\|$ as the absorption coefficient and $\beta = k_0 \Re(\sqrt{\epsilon})$ as the phase constant. $k_0 = 2\pi/\lambda$ is the wave number in free space. The power absorption coefficient κ_a is defined as

$$\kappa_a = 2\alpha. \tag{2.9}$$

The total electromagnetic loss is determined by the extinction coefficient κ_e. It consists of absorption loss and scattering loss. The absorption loss indicates the portion of energy transformed into other forms of energy, such as heat. The scattering loss means the energy travelling in directions other than that of the incident radiation, which is caused by particles of different dielectric constant ϵ embedded in a host medium. The extinction coefficient is expressed as

$$\kappa_e = \kappa_a + \kappa_s, \tag{2.10}$$

with κ_s as the scattering loss. The penetration depth δ_p into a medium is defined as

the depth at which the amplitude of the incident radiation decreases by a factor $1/e$. It means that at the depth δ_p

$$\frac{P(\delta_p)}{P(0+)} = \frac{1}{e},\tag{2.11}$$

or

$$\int_0^{\delta_p} \kappa_e(z)dz = 1,\tag{2.12}$$

where z it the direction normal to the surface, $P(\delta p)$ is the transmitted powder at δ_p, and $P(0+)$ is the transmitted power just beneath the surface (Ulaby, Moore, and Fung, 1986). If κ_e is assumed to be approximately constant with depth z, then the penetration depth can be expressed as

$$\delta_p = \frac{1}{\kappa_e} = \frac{1}{\kappa_a + \kappa_s}.\tag{2.13}$$

If scattering in the medium is ignored, $\kappa_e \equiv \kappa_a = 2\alpha$, the penetration depth δ_p can be described as (Hallikainen and Winebrenner, 1992):

$$\delta_p = \frac{1}{\kappa_a} = \frac{1}{2\alpha}\tag{2.14}$$

When $\epsilon'' \ll \epsilon'$, the penetration depth can also be expressed as

$$\delta_p = \frac{\epsilon'}{k_0\epsilon''},\tag{2.15}$$

2.5 Microwave signatures and scattering of sea ice and seawater

According to Kirchhoff's law, passive microwave signature, i.e. the emissivity, depends on both coherent and incoherent reflection and scattering (Peake, 1959):

$$e_j(\theta_i, \phi_i) = 1 - |R_j(\theta_i, \phi_i)|^2 - \frac{1}{4\pi \cos\theta_i} \int_0^{\pi/2} \int_{-\pi}^{\pi} \sin\theta d\theta d\phi \times [\sigma_{jh}^0(\theta, \phi; \theta_i, \phi_i) + \sigma_{jv}^0(\theta, \phi; \theta_i, \phi_i)],\tag{2.16}$$

where $e_j(\theta_i, \phi_i)$ is the emissivity for polarization $j = H$ or V, at nadir and azimuthal angles of the observation θ_i and ϕ_i, respectively; $|R_j(\theta_i, \phi_i)|^2$ is the Frensnel power reflection coefficient for the same polarization; and $\sigma_{jh}^0(\theta, \phi; \theta_i, \phi_i)$ and $\sigma_{jv}^0(\theta, \phi; \theta_i, \phi_i)$ are the differential scattering cross sections in the scattering direction (θ, ϕ) for H- and V-polarized radiation incident from the direction (θ_i, ϕ_i), respectively. By contrast, active signature observation depends only on the scattering, which includes surface and volume backscattering. When scattering is weak, the emissivity is determined by the reflection coefficient and thus the effective dielectric constant. When scattering increases, active signatures tend to increase while the emissivity typically decreases. A stronger scatterer typically makes a poorer absorber, thus also a poorer emitter. Additionally, multiple scattering tends to decrease the difference between vertically and horizontally polarized brightness temperatures due to the disorder it creates.

Being a mixture of ice, salt, brine pockets, and air bubbles, sea ice exhibits a complicated dielectric behaviour. The dielectric properties of sea ice determine (1) the reflection coefficient at the air-ice and ice-water boundaries, (2) the attenuation coefficient of sea ice, which in turn determines the penetration depth δ_p (defining the radiating layer of sea ice), and (3) the radiative transfer characteristics of sea ice (Ulaby, Moore, and Fung, 1986). The dielectric constant of sea ice ϵ_{si} varies with several sea ice parameters, most notably salinity and temperature. Over the frequency range between 1 and 40 GHz, most measured values of the permittivity ϵ' fall into a narrow range between 2.5 to 8 (Ulaby, Moore, and Fung, 1986). By contrast, the loss factor ϵ'' covers a much wider range, from less than 0.01 to more than 1.0. In general, the loss factor decreases rapidly with increasing negative temperature (Stogryn, 1987; Hallikainen and Winebrenner, 1992), and increases with increasing ice salinity (Ulaby, Moore, and Fung, 1986). Because of the much higher salinity of FYI (typically 5 times that of MYI), the loss factor for FYI is typically 3 to 10 times larger than that for MYI.

As described in Hallikainen and Winebrenner, (1992), the microwave signatures of seawater and several ice types can be characterized as follows.

(1) Seawater

Water is poor emitter in the microwave range. The brightness temperatures of seawater are typically on the order of half the physical temperature, and the horizontally polarized brightness temperatures are substantially below their vertically polarized ones (Ulaby, Moore, and Fung, 1982; Onstott et al., 1987). In active microwave remote sensing, the signatures from water are highly impacted by wind. The microwave intensity backscattered from water increases with increasing wind because wind roughens the water surface.

(2) New ice

Due to the high fraction of brine volume and a small effective dielectric constant (much smaller than that of seawater while large relative to that of thicker ice), new ice transmits more microwave radiation across its surface than seawater, but also strongly absorbs that radiation. The vertically polarized brightness temperatures of new ice are typically within a few percent of the physical temperature, even for ice only a few centimeter thick. Horizontally polarized brightness temperatures are $10 - 15\%$ lower, however they are much higher than those of water. In the absence of frost flowers, backscattering from new ice ranges from strong for deformed or rough ice to weak for bare, undeformed new ice.

(3) First-year ice

As the ice grows into the stage of FYI, it loses brine, its surface becomes colder and usually rougher, and the ice acquires a snow cover. Lower brine volume leads to lower electromagnetic absorption, while increased surface roughness results in increased scattering. Brightness temperatures decrease only a few percent as the ice grows to thick FYI, however the difference between vertically and horizontally polarized brightness temperatures becomes noticeably smaller. Backscattering cross sections for FYI are roughly 5 dB higher than that of new ice at frequencies $1 - 10$ GHz (Onstott et

al., 1987; Livingstone, Singh, and Gray, 1987). However, even a thin snow cover is observed to increase the backscattering and lower the brightness temperatures significantly (Kim, Onstott, and Moore, 1984).

(4) Multiyear ice

Passive signatures of MYI have a large variability due to the highly variable snow cover and the physical structure (bubbly, low-density upper layer and higher density, lower lying layers) (Grenfell, 1992). They show only small polarization differences and and decreasing brightness temperatures with increasing frequency, because of the increased strength of the scattering bubbles at shorter wavelength. The millimeter-size bubbles and low absorption in the upper layer of MYI lead to strong volume scattering. Therefore the average backscattering of MYI is much stronger than that of FYI at frequencies of 5 GHz and above (Kim et al., 1985).

Chapter 3

Data

Passive and active microwave remote sensing data are both used in monitoring sea ice because of their ability of working in the absence of sunlight. Passive microwave sensors, i.e., radiometers, measure the emitted radiation (in terms of brightness temperature). Active microwave sensors, e.g., scatterometers and the imaging radar, measure the backscatter radar signal after reflection off the surface (in terms of backscatter coefficient).

3.1 Radiometer data

The radiometer data used in this study includes data from the Special Sensor Microwave Imager (SSM/I), the Special Sensor Microwave Imager/Sounder (SSMIS), and the Advanced Microwave Scanning Radiometer - Earth Observing System (AMSR-E).

3.1.1 The SSM/I and SSMIS data from NSIDC

The SSM/I is a seven-channel, four-frequency, orthogonally polarized radiometer, operating on the sequential Defense Meteorological Satellite Programme (DMSP) satellites F8, F10, F11, F12, F13, F15 from July 1987 to April 2009. The next generation, SSMIS, was first launched aboard the platform DMSP-F16 in October 2003, and is currently flown aboard the DMSP-F16, -F17 and -F18. The DMSP satellites are in near-polar, sun-synchronous orbits at an altitude of approximately 830 km.

The DMSP SSM/I-SSMIS Daily Polar Gridded Brightness Temperatures from the National Snow and Ice Data Center (NSIDC) are used in the study of Chapter 5. Characteristics of the SSM/I and SSMIS data are shown in Table 3.1 and 3.2, respectively.

TABLE 3.1: Characteristics of SSM/I

Frequencies (GHz)	19.3	22.2	37.0	85.5
Polarization	V/H	V	V/H	V/H
Bandwidth (MHz)	250		1000	1500
Sensitivity (K)		0.6		1.1
Effective field-of-view (km×km)	69×43	60×40	37×28	15×13
Sampling size (km×km)		25×25		12.5×12.5

TABLE 3.2: Characteristics of SSMIS

Frequencies (GHz)	19.3	22.2	37.0	91.7
Polarization	V/H	V	V/H	V/H
Bandwidth (MHz)	400	450	1500	1500
Sensitivity (K)		0.7	0.5	0.9
Effective field-of-view (km×km)		74×45	45×28	16×13
Sampling size (km×km)		25×25		12.5×12.5

3.1.2 The AMSR-E data from BYU

The AMSR-E on board the NASA Aqua satellite is a six-frequency, dual-polarized radiometer, operating from May 2002 to October 2011. It measures horizontally and vertically polarized brightness temperatures at 6.9 GHz, 10.7 GHz, 18.7 GHz, 23.8 GHz, 36.5 GHz, and 89.0 GHz.

The AMSR-E data obtained from the Microwave Earth Remote Sensing (MERS) laboratory of Brigham Young University (BYU) are resampled to grids of 8.9 km and

TABLE 3.3: Characteristics of AMSR-E

Frequencies (GHz)	6.9	10.7	18.7	23.8	36.5	89.0
Polarization	V/H	V/H	V/H	V	V/H	V/H
Bandwidth (MHz)	350	100	200	400	1000	3000
Sensitivity (K)	0.3	0.6	0.6	0.6	0.6	1.1
Effective field-of-view (km×km)	74×43	51×30	27×16	31×18	14×8	6×4
Sampling size (km×km)		8.9×8.9				4.45×4.45

4.45 km (characteristics are shown in Table 3.3). The data are enhanced and reconstructed using the Scatterometer Imager Reconstruction (SIR) resolution enhancement algorithm. The technique is presented in Long and Daum, (1998) for the passive microwave data. It takes advantage of the spatial overlap made at different times of one day to enhance the imaging resolution, which is equivalent to the antenna-pattern deconvolution (Long, Hardin, and Whiting, 1993; Long and Daum, 1998). It also uses multiple passes from different orbits during one day to reduce pixel noise. The dataset is reconstructed onto a 4.45 km grid in a polar stereographic projection. The enhanced AMSR-E data includes ascending (mid-day) and descending (mid-night) passes products. The descending passes product is used to be consistent with the QuikSCAT data, which will be introduced in the next subsection.

3.2 Scatterometer data

3.2.1 The QuikSCAT data from BYU

The SeaWinds scatterometer onboard QuikSCAT is a 13.4 GHz conically scanning pencil-beam scatterometer, operating from July 1999 to November 2009. It has two beams, each with a wide range of azimuth angles. The inner beam is horizontally polarized at an incidence angle of of $46\,°$, whereas the outer beam is vertically polarized at an

incidence angle of $54°$ (Hoffman and Leidner, 2005). The sensor measures normalized cross section or backscatter coefficient (σ^0) values in dB over a swath width of 1800 km.

The QuikSCAT data, backscatter coefficients σ^0_{hh} and σ^0_{vv} (uncorrelated channels), from BYU are enhanced and reconstructed using the SIR algorithm with a technique presented in Early and Long, (2001). The data is reconstructed onto a 4.45 km grid, in a polar stereographic projection. Two versions of the data exist; called "slice" and "egg" measurements from SIR-enhanced QuikSCAT. Due to its low sensitivity to noise during the SIR process, the descending (evening) passes "egg" product from SIR-enhanced QuikSCAT is used.

3.3   Auxiliary data

3.3.1   Reanalysis air temperatures

Air temperature data at the level 2 m from the surface were obtained from the European Reanalysis (ERA-Interim) project, archived at the European Centre for Medium-Range Weather Forecasts (ECMWF). This is a global atmospheric reanalysis that dates back 1979 and has been continued to present. It provides a large variety of 3-hourly surface parameters, describing weather as well as ocean-wave and land-surface conditions, and 6-hourly upper-air parameters covering the troposphere and stratosphere (Dee et al., 2011). For the present study, data at $1.5° \times 1.5°$ latitude/longitude grid, acquired at 00:00 UTC, was resampled to the same grid as the QuikSCAT and AMSR-E data (4.45×4.45 km^2).

3.3.2   Ice drift data from NSIDC

Polar Pathfinder Daily 25×25 km^2 resolution Equal Area Scalable Earth Grid (EASE-Grid) Sea Ice Motion Vectors, Version 2 (Tschudi et al., 2010; Fowler, Emery, and Tschudi, 2013) from the National Snow and Ice Data Center (NSIDC) is used in this study. It provides daily gridded ice motion vectors and the estimated error variance

from November 1978 to December 2012. The vectors are obtained from a variety of remote sensing data such as the Advanced Very High Resolution Radiometer (AVHRR), the Scanning Multichannel Microwave Radiometer (SMMR), SSM/I and AMSR-E. The observations are merged with the buoy data from the International Arctic Buoy Program (IABP) and wind data from the National Centers for Environmental Prediction (NCEP) analysis, using a co-kriging estimation method described in Isaaks and Srivastava, (1989). The AVHRR data is only used until December 2004 and all passive microwave remote sensing data are used during their operation time (SMMR 1978–1987, SSM/I 1987–2006, SSMIS 2007–2012, AMSR-E 2002–2012). The ice drift data were resampled to the same grid spacing as the QuikSCAT and AMSR-E data (4.5×4.5 km^2).

3.3.3 Radarsat-1 SAR data

Radarsat-1 was a Canadian Earth Observation Satellite, operating from March 1995 to March 2013. It carried a synthetic aperture radar (SAR) instrument, working at 5.3 GHz (C-band). The Radarsat-1 SAR instrument transmitted and received signals for capturing images of the Earth night and day and in all-weather conditions. A wide variety of beam widths were available to capture swaths of $45 - 500$ km, with a range of $8 - 100$ m in resolution and incidence angles of $10° - 60°$ (Table 3.4).

TABLE 3.4: Characteristics of Radarsat-1 SAR data

	Fine Mode	Standard Mode	ScanSAR Mode
Polarization	HH	HH	HH
Spatial Resolution	8 m	30 m	50-100 m
Swath Width	45 km	100 km	300-500 km
Off-Nadir Angle	$37° - 47°$	$20° - 49°$	$20° - 49°$

Chapter 4

Methods to estimate MYI concentration

Many algorithms have been developed to estimate sea ice concentrations from passive and active microwave observations. A partial list is provided in Ivanova et al., (2014) with comparisons of their performances. Among them, only a few algorithms are able to distinguish different ice types and estimate their partial concentrations, e.g., MYI concentration. These are methods to derive concentrations of MYI as well as FYI (Cavalieri, Gloersen, and Campbell, 1984; Steffen and Schweiger, 1991; Lomax, Lubin, and Whritner, 1995; Comiso et al., 1997; Kwok, 2004; Wang et al., 2009; Ye and Heygster, 2015), a method that estimates thin ice and ice with snow layering types (Markus and Cavalieri, 2000), and a method that determines concentration of any given set of ice types based on the provided characteristics (Shokr, Lambe, and Agnew, 2008). This chapter introduces four commonly used algorithms for MYI concentration retrieval from microwave remote sensing data: the NASA Team algorithm (Cavalieri, Gloersen, and Campbell, 1984; Steffen and Schweiger, 1991), the Bootstrap algorithm (Comiso, 2012), the Lomax algorithm (Lomax, Lubin, and Whritner, 1995) and the ECICE algorithm (Shokr, Lambe, and Agnew, 2008). The NASA Team algorithm is used in Chapter 5, and the ECICE algorithm is used in Chapters 6 and 7.

4.1   The NASA Team algorithm

The NASA Team algorithm uses brightness temperatures of three channels, namely the 19 GHz horizontally (H) and vertically (V) polarized channels and the vertically

polarized 37 GHz channel to calculate sea ice concentration (including MYI and FYI concentration) from SSM/I data (Cavalieri, Gloersen, and Campbell, 1984; Swift, Fedor, and Ramseier, 1985; Gloersen and Cavalieri, 1986; Steffen and Schweiger, 1991). Two independent parameters are used in the algorithm: the microwave polarization ratio (PR) at 19 GHz and a spectral gradient ratio (GR), which uses the brightness temperature at vertically polarized channels of 37 GHz and 19 GHz. These ratios are:

$$PR = \frac{Tb_{19v} - Tb_{19h}}{Tb_{19v} + Tb_{19h}}, \tag{4.1}$$

$$GR = \frac{Tb_{37v} - Tb_{19v}}{Tb_{37v} + Tb_{19v}}, \tag{4.2}$$

where Tb is the brightness temperature of the indicated channel. By neglecting contributions from the atmospheric and cosmetic radiation, the brightness temperature for each frequency and polarization can be written as:

$$Tb = Tb_{OW} \cdot (1 - C_{MYI} - C_{FYI}) + Tb_{FYI} \cdot C_{FYI} + Tb_{MYI} \cdot C_{MYI}. \tag{4.3}$$

where Tb is the brightness temperature measured from the satellite; Tb_{OW}, Tb_{FYI} and Tb_{MYI} are those for 100% open water (OW), FYI and MYI, called tie points; C_{FYI} and C_{MYI} are the concentrations of FYI and MYI. With the substitution of (4.3) to 4.1 and 4.2, concentrations of the above surface types can be derived by solving the equations.

The precision of sea ice concentration from the NASA Team algorithm is sufficient to provide large-scale polar ice cover, however MYI concentration contains significant uncertainties (Cavalieri, Gloersen, and Campbell, 1984). In Cavalieri et al., (1991), the authors compared the retrievals from the NASA Team algorithm with that from the aircraft observation. It was found that the NASA Team algorithm overestimates MYI concentration by $12\% \pm 11\%$ on average in the Chukchi and Beaufort Seas.

4.2 The Bootstrap algorithm

The Bootstrap algorithm was first developed in Comiso, (1990) to derive MYI concentration with vertically polarized SMMR data at 18 GHz and 37 GHz. The MYI concentration maps are found to be qualitatively similar to those from other algorithms (e.g., Cavalieri, Gloersen, and Campbell, (1984)). But the spatial distribution of the derived MYI cover does not reflect the ice condition during the previous summer as the bias of the formulation and large footprint of the satellite sensors. In Comiso, (2012), the authors made an improvement on the algorithm by using the "dynamic tie points"from two channels of the AMSR-E data (i.e. Tb_{36h} and Tb_{36v}).

4.3 The Lomax algorithm

In Lomax, Lubin, and Whritner, (1995), the authors developed an algorithm (the Lomax algorithm) to retrieve MYI concentration with SSM/I data at 85.5 GHz. The algorithm utilizes the polarization corrected temperature (PCT) at 85.5 GHz to exploit the large differences in emissivity between FYI and MYI, since the PCT is an index for the influence of volume scattering on the satellite-measured brightness temperature and the volume scattering from MYI has a noticeable impact on 85.5 GHz brightness temperatures.

The PCT is defined in Spencer, Goodman, and Hood, (1989),

$$PCT = (\beta Tb_h - Tb_v)/(\beta - 1), \tag{4.4}$$

where

$$\beta = (Tb_{vc} - Tb_{vo})/(Tb_{hc} - Tb_{ho}). \tag{4.5}$$

Tb_{hc} and Tb_{vc} are the horizontally and vertically polarized brightness temperatures measured from space over a cloud-free ocean, respectively, whereas Tb_{ho} and Tb_{vo} are the horizontally and vertically polarized brightness temperatures measured at the

ocean surface. In Spencer, Goodman, and Hood, (1989), it is found that a model calculation of $\beta = 0.38$ is appropriate for dry atmospheres over polar oceans, which means $PCT = 1.613Tb_v - 0.613Tb_h$.

In the retrieval procedure of MYI concentration from Lomax, Lubin, and Whritner, (1995), first, total sea ice concentration (C_T) is calculated using the algorithm of Svendsen, Matzler, and Grenfell, (1987), and the 85.5 GHz PCT is computed with the satellite measured brightness temperatures. Second, the 85.5 GHz PCTs for 100% FYI and MYI (PCT_{FYI} and PCT_{MYI}, respectively) are estimated based on the near-linear relation between the PCT and MYI concentration from the NASA Team algorithm. These two PCT values are regarded as tie points for the Lomax algorithm. Thus MYI concentration can be derived from:

$$C_{MYI} = C_T \cdot \frac{PCT - PCT_{FYI}}{PCT_{MYI} - PCT_{FYI}}. \tag{4.6}$$

For nearly cloud-free winter conditions, results from this algorithm and those from NASA Team algorithm has a standard deviation of $\pm 6\%$, with slightly better agreement at low multiyear concentration (Lomax, Lubin, and Whritner, 1995).

4.4   The ECICE algorithm

The Environment Canada's Ice Concentration Extractor (ECICE) algorithm starts with a linear mixing model that decomposes each radiometric observation into contributions from each surface type (in our case YI, FYI, MYI, and OW) weighted by the concentration of the surface type within the sensor's field of view. The set of linear equations is incorporated with a set of constraints to construct a cost function, in which the partial concentration of each ice type is an explicit parameter. The constraints include an equality condition, which stipulates that the sum of all partial concentrations must be 100%, and a set of inequality constraints, which stipulate that partial concentration of each surface type must be between 0 and 100%. The optimal solution minimizes

the cost function (Shokr, Lambe, and Agnew, 2008). Instead of using a single set of tie points in the linear mixing model, the algorithm uses a large number of sets of characteristic values (typically in the order of 1000), and each set represents a possible (but not necessarily a typical) value of the given radiometric parameters for each surface type. A random number generator is used to generate each set of characteristic values with the known distribution. It then serves to obtain a possible optimal solution. The final optimal solution (concentration of ice types for each pixel) is generated from the 1000 possible solution using a weighted average of all solutions.

In Chapters 6 and 7, the ECICE algorithm is used with four input parameters: backscatter coefficients σ^0_{hh} and σ^0_{vv} from QuikSCAT and brightness temperatures at the 36.5 GHz horizontal and vertical polarization channels (Tb_{37h} and Tb_{37v}) from AMSR-E. In addition, a linear combination of brightness temperature from the 18.7 GHz and 23.8 GHz channels is used to filter the open water pixels.

Chapter 5

MYI concentration retrieval with the NASA Team algorithm using dynamic tie points

5.1 Motivation

Sea ice concentration can be derived reliably using the NASA Team algorithm. However, the MYI concentration retrievals have much larger uncertainties (Cavalieri et al., 1991; Lomax, Lubin, and Whritner, 1995) due to the reasons below. First, variability of tie points (typical brightness temperatures of each surface type at all the channels) is not accounted. Second, microwave signatures of MYI and FYI are highly influenced by snow and weather conditions, which leads to erroneous retrievals of partial ice concentration (Shokr and Agnew, 2013; Tonboe, Andersen, and Toudal, 2003; Mathew, Heygster, and Melsheimer, 2009; Ye, Heygster, and Shokr, 2015). In this chapter, a modified version of the NASA Team algorithm with dynamic tie points is presented to compensate the temporal impact of brightness temperature variations. To assess the performance of the original and modified NASA Team algorithm (using fixed and dynamic tie points, respectively), MYI concentration retrievals from both methods are analysed for all the winters from 1989 to 2012. In addition, influence of each tie point on the MYI concentration retrieval is investigated in the sensitivity study.

5.2 Methods

As described in Chapter 4, the NASA Team algorithm uses brightness temperatures of three channels, namely the 19 GHz horizontally (H) and vertically (V) polarized channels and the vertically polarized 37 GHz channel. The brightness temperatures for 100% MYI, FYI and open water (OW) are regarded as tie points. For the original NASA Team algorithm, the tie points are a set of fixed values, based on experimental and statistical studies. However, the temporal and spatial variability in brightness temperature of the three surface types introduces errors in the estimates of MYI and FYI concentrations. We propose to use dynamic tie points to minimize the error associated with this variability.

The brightness temperatures of sea ice and open water at different frequencies and polarizations vary considerably as shown in the scatter plot in Figure 5.1, which shows SSM/I 19 and 37 GHz brightness temperatures at vertical polarization. For the dynamic NASA Team algorithm, dynamic tie points are derived daily using the following technique:
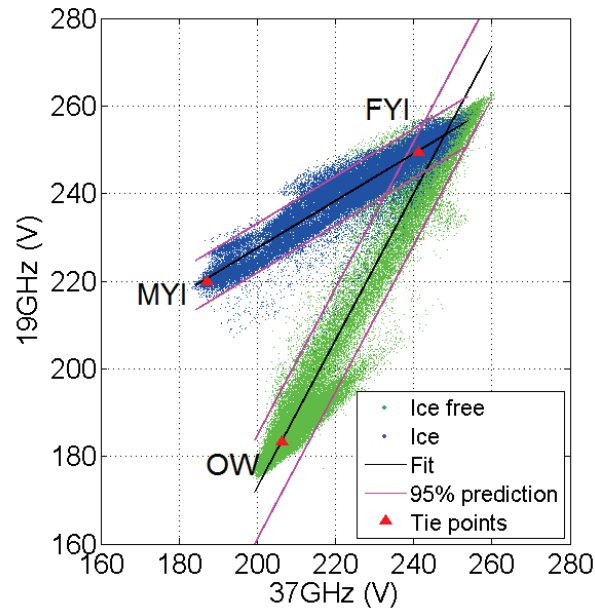

FIGURE 5.1: Scatter plot of brightness temperatures at 37 and 19 GHz vertical polarization on January 1, 2007. Green data points are taken from the region which is ice free in summer, blue data points from the region that has ice in summer, red triangle points are the dynamic tie points derived from the scatter plot.

First, two regions are defined for taking samples. One is generally ice covered, the other one is partly open water. The ice covered region is the region of the minimum ice extent of the previous September. The "ice free" region is not without ice the whole year but the region where monthly total ice concentration is zero for at least one month from the previous October to that September. Thus, it may be partly or completely ice covered in other months. This region is assumed to contain a mixture of OW and FYI. Data from each day along with the previous and following three days are taken from the defined regions and plotted as shown in Figure 5.1. In order to exclude noisy data points, the number density is calculated in each 1 K by 1 K bin, in a 2-D histogram of the 19 GHz and 37 GHz V channels. Data points in the grid where the number density is below 5 are eliminated. With a linear regression, data points that are outside 95% prediction of the regression lines are removed. It is assumed that the data points are randomly sampled from a Gaussian distribution. 95% of the samples will lie within the 95% prediction lines.

Second, another line is regressed based on the remaining data points. A set of lines perpendicular to the regression line are generates. For each data point, there is a corresponding perpendicular line with a certain intercept on the 19 GHz V axis. The average of the ice region data points of which the intercept is between 0.1% and 0.4% (threshold range for MYI tie points) of the largest intercept are regarded as the tie points for MYI. The average of the ice free data points of which the intercept is between 20% and 25% (threshold range for OW tie points) of the largest intercept are regarded as the tie points for OW. The average of the ice region data points located between the lines that are parallel to the regression line of ice free data points and have an intercept between 90% and 110% (threshold range for FYI tie points) of the regression intercept are regarded as the tie points for FYI. Another possible solution of deriving tie points for FYI could be the intercept of the two regression lines. However, the latter method will lead to big difference between the dynamic and fixed tie points.

The fixed tie points of OW correspond to calm water under dry atmosphere. Tie points of FYI and MYI correspond to 100% FYI and MYI respectively. Dynamic tie

TABLE 5.1: Average difference between dynamic tie points and fixed tie points.

Surface type	Threshold range	19 GHz H (K)	19 GHz V (K)	37 GHz V (K)	Sum of absolute difference
OW	15%-20%	-1.85	-2.83	0.17	4.85
	20%-25%	0.53	-1.6	1.23	3.36
	25%-30%	3.13	-0.24	2.43	5.8
MYI	0.1%-0.4%	2.56	-2.5	-0.36	5.42
	0.4%-0.7%	3.18	-1.82	0.87	5.87
	0.7%-1%	3.65	-1.36	1.71	6.72
FYI	85%-115%	-4.08	-2.45	-2.5	9.03
	90%-110%	-2.11	-0.86	0.74	3.71
	95%-105%	0.08	0.97	4.28	5.33

points are derived with the empirical method described above. Threshold ranges of the method are selected according to the idea that averages of the dynamic tie points in all the winter months from 1998 to 2007 are close to the fixed tie points. That means we select the threshold range for each surface type with the smallest average difference between dynamic and fixed tie points, which corresponds to the smallest sum of absolute differences at the three channels. More threshold ranges than those in Table 5.1 were tried in this study. We only show those with relatively small average difference.

Figure 5.2 shows the fixed and dynamic tie points for ice and open water at all the three channels from 1998 to 2007 (October to May). Compared to the dynamic tie points for FYI and MYI, those for OW have much less seasonal variations. It indicates that the influence of the atmosphere is much less than that of ice. In each year, the dynamic tie points of FYI and MYI have high values at the beginning of November and end of May, as the high temperature of air and ice increases the contribution to the observed brightness temperature through high snow wetness and high surface temperature. Dynamic tie points in October and May are shown in Figure 5.2 but not included in this study as the thin ice in October and the high air temperature in May would cause errors of MYI concentration retrieval. It is known that the influence of
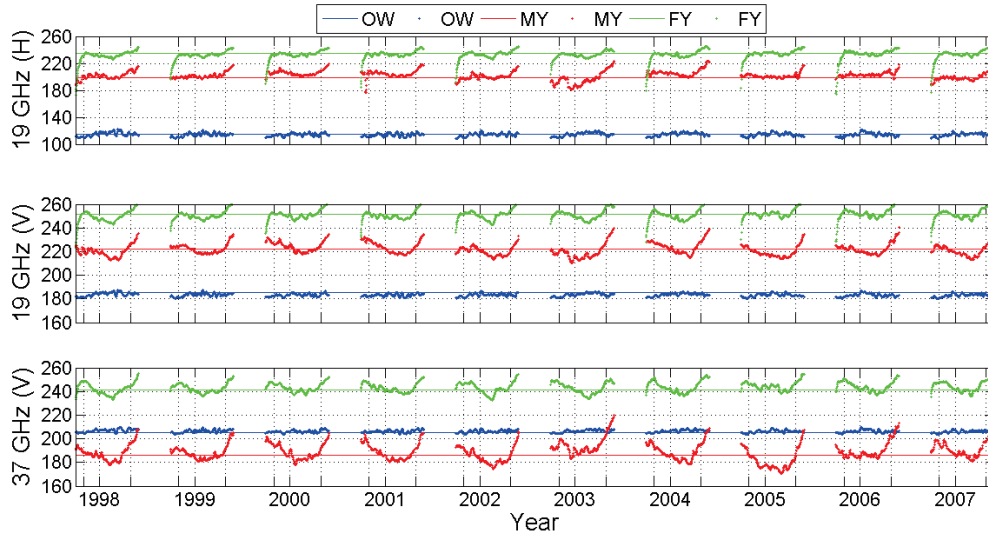
FIGURE 5.2: Dynamic tie points from 1998 to 2007 (October to May). Vertical bars show beginnings of November, January and May of each winter. Dynamic tie points are represented by dots, while fixed tie points are represented by the colored lines.

thin ice is much larger at 19 GHz H than that at 19 GHz V and 37 GHz V, with an increase of 45 K at 19 GHz H when ice thickness increases from 10 cm to 50 cm, while the increase is 9 K and 5 K at 19 GHz V and 37 GHz V, respectively. (Heygster et al., 2014). Therefore, large variations are expected for tie points of FYI at 19 GHz H, while those of MYI and OW have much smaller variations, leading to unexpected retrievals. Besides, the high air temperature in May could cause snow melt on ice, resulting in erroneous MYI retrievals.

In addition to the seasonal variations, the inter-annual variations of tie points for FYI and MYI are much larger than those of OW. In warm winters such as the winter of 2002/2003, 2005/2006 and 2006/2007, tie pointes for MYI at 37 GHz V channel are larger than those in other years, since the emissivity of ice increases when there is an increase of snow wetness on ice (Ulaby, Moore, and Fung, 1986). The warm weather could cause increasing snow wetness and lead to increase of brightness temperature consequently, which is more pronounced at 37 GHz than at 19 GHz (Drobot and Anderson, 2001).

The average absolute daily change Tb_{aag} of the dynamic tie points from 1998 to 2007 (November to April) are shown in Table 5.2. The small daily change of tie points in all

TABLE 5.2: Average daily change of dynamic tie points from 1998 to 2007.

Surface type	$Tb_{19h,aag}$ (K)	$Tb_{19v,aag}$ (K)	$Tb_{37v,aag}$ (K)
OW	0.51	0.26	0.22
MYI	0.41	0.26	0.37
FYI	0.24	0.2	0.24

channels and surface types confirms the tie points deriving procedure.

5.3   Time series results

Using fixed and dynamic tie points, both total and MYI concentrations are retrieved daily with the NASA Team algorithm for all winters (November to April) from 1989 to 2012. Figure 5.3 shows the MYI extent, defined as the sum of the area covered by grid cells that have 30% or higher MYI concentration (Comiso, 2012). Both MYI retrievals show lower MYI extent than the annual minimum of the total ice extent in September. There are two reasons for the differences. Firstly, the MYI extent is extracted by ignoring pixels with MYI concentration below 30%. Secondly, FYI is already formed at the time of the annual ice extent minimum in September.

In the NASA Team algorithm, polarization ratio (PR) and gradient ratio (GR) are calculated as below:

$$PR = \frac{Tb_{19v} - Tb_{19h}}{Tb_{19v} + Tb_{19h}}, \qquad (5.1)$$

$$GR = \frac{Tb_{37v} - Tb_{19v}}{Tb_{37v} + Tb_{19v}}, \qquad (5.2)$$

where Tb_{19v}, Tb_{19h} and Tb_{37v} are the brightness temperature at 19 GHz V, 19 GHz H and 37 GHz V channel. MYI concentration retrieval is mainly determined by GR in the GR/PR space because of its high sensitivity for MYI concentration retrieval. Based on the average brightness temperature differences between dynamic and fixed tie points
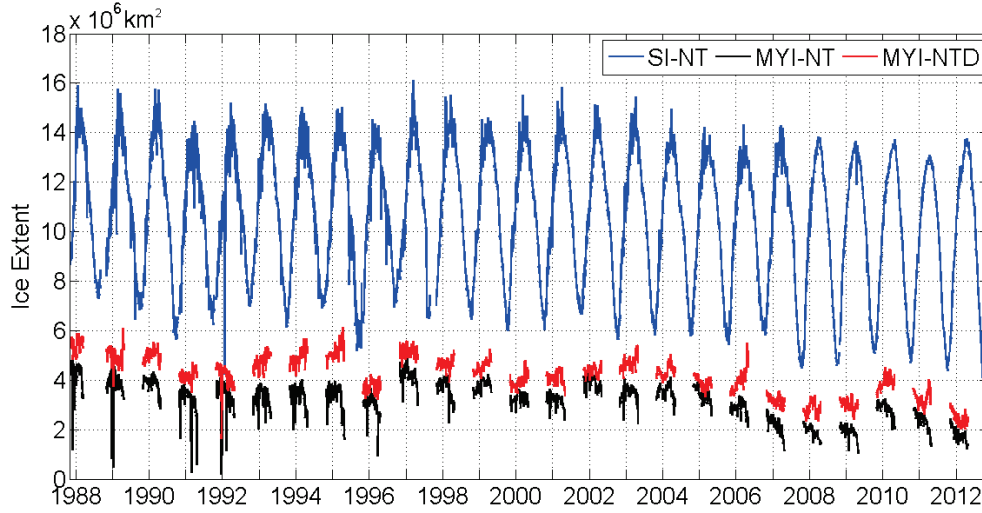
FIGURE 5.3: Total sea ice extent retrieved with NASA Team algorithm, MYI extent retrieved with NASA Team algorithm and dynamic NASA Team algorithm from 1989 to 2012. SI-NT: total sea ice extent retrieval with NASA Team algorithm, MYI-NT: MYI extent retrieved with NASA Team algorithm, MYI-NTD: MYI extent retrieval with dynamic NASA Team algorithm.

in Table 5.2, GR of averaged dynamic tie points for FYI and MYI are:

$$GR_{FY} = \frac{Tb_{FY,37v} - Tb_{FY,19v} + 0.74 + 0.86}{Tb_{FY,37v} + Tb_{FY,19v} + 0.74 - 0.86}, \tag{5.3}$$

$$GR_{MY} = \frac{Tb_{MY,37v} - Tb_{MY,19v} - 0.36 + 2.5}{Tb_{MY,37v} + Tb_{MY,19v} - 0.36 - 2.5}, \tag{5.4}$$

where $Tb_{FY,37v}$ and $Tb_{FY,19v}$ are the brightness temperature of fixed tie points for FYI at 37 GHz V and 19 GHz V, Tb_{MY} are those for MYI. They are larger than GR of the fixed tie points. In addition, the GR differences between that of fixed and dynamic tie points for MYI are bigger than those for FYI, which makes GR of second year ice closer to that of MYI. As a consequence, the method using dynamic tie points yields higher estimates than that using fixed tie points in most winters, which is shown in Figure 5.3.

There is a slightly declining trend of minimum ice extent as shown in Figure 5.1, which is consistent with the MYI extent retrieved from both methods. In most winters, MYI extent decreases as expected. One reason for the MYI reduction is the export to more southern regions. Figure 5.4 shows the reduction of MYI area and the ice outflow
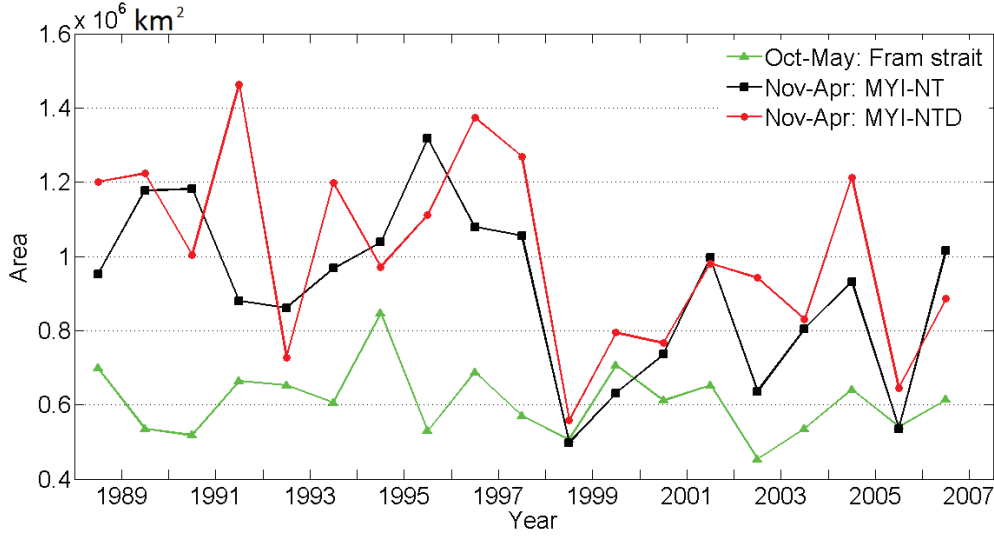
FIGURE 5.4: Arctic sea ice outflow through Fram Strait (October-May) (Kwok, 2009) and MYI reduction (November-April) from 1988 to 2007.

through Fram Strait (Kwok, 2009) from 1988 to 2007. It is noted that the MYI area takes the pixels with MYI concentration below 30% into account. In all, the MYI reduction is larger than however not highly correlated to the ice export through Fram, with a correlation coefficient of 0.15 and 0.22 for the retrieval from original and dynamic NASA Team algorithm respectively. The difference between Fram strait export and MYI area could be caused discrepancy in considered periods and the export through regions like Canadian archipelago.

Figure 5.3, MYI extent retrieved from both methods increases during some winters, such as the winter of 1999/2000. It could be caused by the ice drift from central Arctic, which is not covered by SSM/I data. Besides, the MYI extent changes rapidly from day to day, which could be caused by the sensor noise.

5.4 Sensitivity study and discussion

A sensitivity study was conducted to see the influence of each tie point on the MYI concentration retrieval. The standard deviation Tb_{std} and average difference Tb_{diff} are introduced to measure the stability of the dynamic tie points and the difference from

fixed tie points. Tb_{diff} is calculated as:

$$Tb_{diff} = avg(Tb_{dyn}) - Tb_{fix} \tag{5.5}$$

where Tb_{dyn} is the dynamic tie point, Tb_{fix} is the fixed tie point.

Table 5.3 lists the standard deviation and average difference of all the dynamic tie points in winters from 1998 to 2007. It shows that the average difference Tb_{diff} between the average dynamic tie point Tb_{dyn} and the fixed tie point Tb_{fix} for OW at 19 and 37 GHz V is larger than one standard deviation, which means tie points for OW at the two channels are not well estimated. Among all the tie points, those for MYI are most unstable. For FYI and MYI, the average difference Tb_{diff} is smaller than Tb_{std} in all channels, which means tie points for FYI and MYI are estimated well.

TABLE 5.3: Standard deviation and average difference of dynamic tie points.

Surface type	19 GHz H (K)		19 GHz V (K)		37 GHz V (K)	
	Tb_{diff}	Tb_{std}	Tb_{diff}	Tb_{std}	Tb_{diff}	Tb_{std}
OW	0.53	2.47	-1.6	1.3	1.23	1.12
MYI	2.56	4.65	-2.5	3.71	-0.36	5.6
FYI	-2.11	2.62	-0.86	2.8	0.74	3.53

In order to evaluate the sensitivity of ice concentrations to changes in the tie points, we define two parameters, the first one is

$$C_{SEN1} = \frac{avg(C_{MY+} - C_{MY-})}{2}, \tag{5.6}$$

this is half of the average of ice concentration if two modified sets of tie points are used, where C_{MY+} and C_{MY-} are the MYI concentration retrieved with the tie points increased and decreased by one standard deviation respectively. For three used channels and three surface types, this results in nine sensitivity parameters C_{SEN1} given in

Table 5.4. There, in addition the sensitivity C_{SEN2} is given,

$$C_{SEN2} = C_{SEN1} \times Tb_{diff}/Tb_{std}, \tag{5.7}$$

which describes the difference of MYI concentration caused by the difference of tie points.

TABLE 5.4: Sensitivity parameters of the dynamic tie points.

Surface type	19 GHz H (%)		19 GHz V (%)		37 GHz V (%)	
	C_{SEN1}	C_{SEN2}	C_{SEN1}	C_{SEN2}	C_{SEN1}	C_{SEN2}
OW	0.027	0.006	-0.26	0.32	0.07	0.08
MYI	0.26	0.14	-2.46	1.66	1.48	-0.1
FYI	0.39	-0.31	-6.32	1.94	2.94	0.61

Table 5.4 shows that MYI retrieval is most sensitive to the tie points at 19 GHz V channel and least sensitive to those at 19 GHz H channel. In the NASA Team algorithm, 19 GHz H is only used in PR. As mentioned above, MYI concentration retrieval is mainly determined by the gradient ratio (GR) in the GR/PR space. The low sensitivity of horizontal channel (shown in Table 5.4) confirms the weak influence of polarization ratio. Besides, tie points of MYI and FYI are more sensitive than those of OW as expected. To sum up, tie points of MYI and FYI at 19 GHz V are the most sensitive thus need to be determined as precisely as possible if the dynamic NASA Team algorithm is used.

To conclude, dynamic tie points improve the retrieval of MYI concentration with the NASA Team algorithm by taking the temporal variation of brightness temperature into account. However, because of the high sensitivity of tie points and the impact of spatial variation of brightness temperature, much work could be done to further improve the retrieval of MYI with the NASA Team algorithm. For example, we could define three regions for deriving tie points of OW, FYI and MYI instead of two (shown in Figure 5.1). Furthermore, better weather filters could improve the retrieval as well.

Chapter 6

Improving MYI concentration estimates with air temperatures

6.1 Motivation

MYI characteristics can be retrieved from passive and active microwave remote sensing observations. One of the algorithms that combine both observations to identify partial concentrations of ice types (including MYI) is the ECICE algorithm. However, cycles of warm-cold air temperature trigger wet-dry cycles of the snow cover on MYI surface. Under wet snow conditions, anomalous brightness temperature and backscatter, similar to those of first year ice (FYI) are observed. This leads to misidentification of MYI as being FYI, hence decreasing the estimated MYI concentration suddenly. The purpose of this chapter is to introduce a correction scheme to restore the MYI concentration under this condition. The correction is based on air temperature records. It utilizes the fact that the warm spell in autumn lasts for a short period of time (a few days). The correction is applied to MYI concentration retrievals from ECICE using an input of combined QuikSCAT and AMSR-E data, acquired over the Arctic region in a series of autumn seasons from 2003 to 2008.

6.2   Misclassification of MYI as FYI

As described in Shokr and Agnew, 2013, ECICE misclassifies MYI as being FYI in autumn during warm spells when the atmospheric temperature approaches the melting point. The correct classification is restored shortly after the cold temperature resumes. Based on the MYI concentration maps, a sudden decrease of MYI concentrations followed by restoration of previous-days concentration is regarded as an anomaly, the duration of which is examined and shown in Table 6.1 (only one such anomaly is observed beyond October). The most common duration is about 1–2 days. The same study shows also that during such periods the passive microwave brightness temperature from MYI increases and the backscatter from scatterometer decreases, approaching typical values from FYI. This anomaly has been examined in more detail in the present study. Apart from warm air spells, ice motion could also explain the rapidly changing radiometric signals. However, this explanation holds mostly within the marginal ice zone. MYI area and concentration in this zone is remarkably smaller than those within the pack ice. Therefore, ice motion is not considered in the correction scheme in the next section as the anomalies are mostly observed within the pack ice.

TABLE 6.1: Number of days with anomalies in September and October of each year (from the beginning of the drop in the retrieved MYI concentration until it recovers)

	Duration	2003	2004	2005	2006	2007	2008
	1-2 days	7	3	6	2	6	4
September	3-4 days	1	2	1	4	0	2
	5-6 days	0	1	0	0	0	2
	1-2 days	2	0	0	1	0	0
October	3-4 days	0	0	0	0	0	0
	5-6 days	0	0	0	0	0	0

In 2003, the retrieved MYI concentration from ECICE in the marginal MYI zones of Laptev Sea and Kara Sea decreased suddenly on September 24 and 25 and returned to its previously high value on September 27 (Figure 6.1a). The FYI concentration in the same region changed in the opposite direction (Figure 6.1b). However, physically it is

impossible for MYI to turn to FYI and it is very unlikely that MYI is replaced by FYI (due to ice motion) for two days in the shown large area before restoring its concentration two days later. Thus, the suddenly decreased MYI concentrations on September 24 and 25 must be wrong estimates. In comparison with the temperature maps (Figure 6.1c), the misclassification occurs when a warm spell (temperatures approaching melting point) prevails, and disappears when it abates. Therefore, the sudden (erroneous) decrease in MYI concentration should be interpreted in terms of the air temperature rise. The interpretation and correction offered later in Section 6.3 assumes that the MYI was snow-covered, which is practically always the case with MYI.
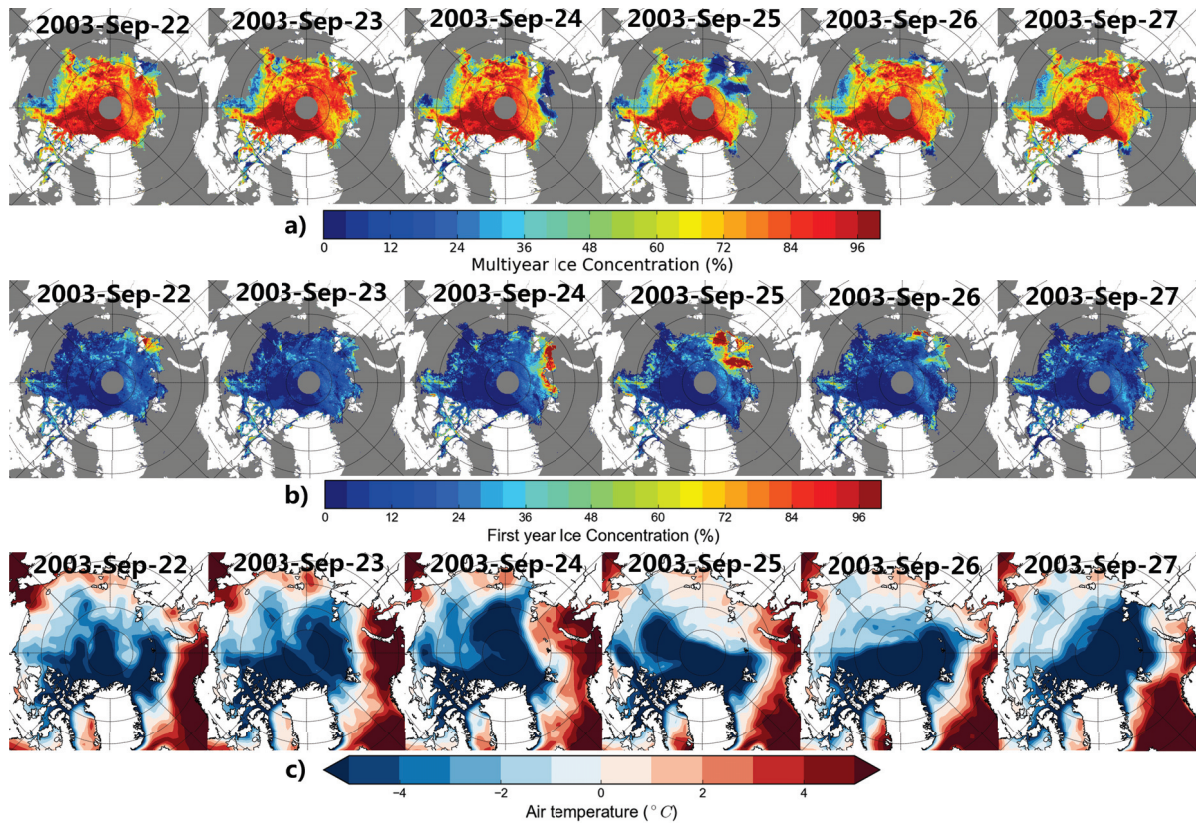
FIGURE 6.1: (**a**) Multiyear ice concentration retrieved from ECICE, (**b**) first year ice concentration also from ECICE and (**c**) surface air temperature from 22 to 27 September 2003.

Figure 6.2 shows the average concentration of MYI and FYI, air temperature, brightness temperature and backscatter records from all pixels within an area bounded by $83.75° - 84°$ latitude and $44° - 45°$ longitude in September 2008. This area and period have been selected to illustrate the influence of the air temperature when it approaches

the melting point. When air temperature rose to hover around 0 °C, the retrieved MYI concentrations dropped from near 100% to values below 40% (reaching 0% in some cases as shown in the figure). In contrast, the retrieved FYI concentrations increased, keeping the total sea ice concentration at values near or equal 100%. Changes of ice concentrations followed similar changes in brightness temperatures (Tb_{37v} and Tb_{37h}) as well as backscatters (σ_{hh}^0 and σ_{vv}^0). When air temperature approached 0 °C, Tb_{37h} and Tb_{37v} increased to attain typical values of FYI (230.0 K and 260.0 K, respectively). At the same time, σ_{hh}^0 and σ_{vv}^0 decreased from typical values of MYI (-6 dB and -8 dB, respectively) to those of FYI (-16 dB and -17 dB, respectively).
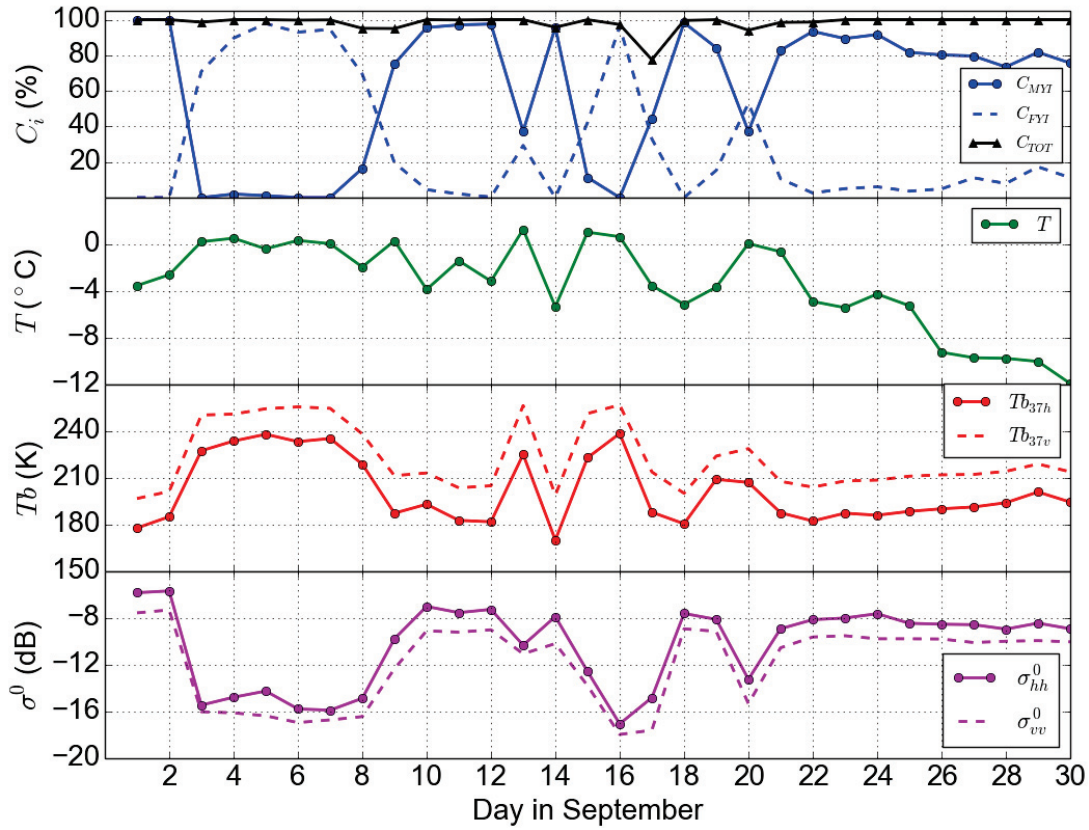

FIGURE 6.2: Averaged multiyear (C_{MYI}), first-year ice concentration (C_{FYI}) and total sea ice concentration (C_{TOT}), surface air temperature (T), brightness temperature (Tb_{37h} and Tb_{37v}) and backscatter (σ_{hh}^0 and σ_{vv}^0) of selected pixels (latitude: 83.75 ° - 84 °, longitude: 44 ° - 45 °) in September 2008.

From a physical point of view, microwave emission and scattering from snow is affected by a few factors including snow wetness, density, salinity, grain size (when

metamorphosed), layering of ice lenses, and surface crust. The overlain snow on MYI is nearly salt-free and is stable during the cold winter in the Arctic. Interpretation of the aforementioned anomaly should take into account the above-described microwave signature (both brightness temperature and backscatter) changes in response to the intrusion and retreat of warm air spells. The restoration of the microwave signature to their typical values after the end of the warm spell suggests the exclusion of any possible effect of snow metamorphism caused by melt-refreeze events. Snow metamorphism (taking a form of snow layering, and changes of grain shape and size) will cause an irreversible drop in brightness temperature and increase in backscatter (due to volume scattering). Without snow metamorphism the changes of snow wetness during the transition of air temperature (i.e. the increase during warm temperature and decrease when cold temperature resumes) change the emitted and scattered radiation, yet in a reversible manner (as observed in Figure 6.2). Therefore, it can be assumed that the wet/dry cycle of snow (associated with the warm/cold cycle of air temperature) does not add to the metamorphism of snow and that assures the restoration of the microwave signature.

As indicated in Comiso, 1985, the emissivity of snow-covered MYI increases as snow wetness increases (data were available up to 5% volumetric water content), causing the brightness temperature of MYI to approach values of FYI. The study by Rott and Nagler, 1994 shows that at 36 GHz and higher frequencies, the emissivity of the snow/ice pack increases to values above 0.9 compared to values around 0.8 for dry snow and 0.6 for frozen crust. A relevant finding was concluded by Mathew, Heygster, and Melsheimer, 2009 who estimated emissivity of Arctic sea ice using AMSR-E data. The authors reported an increase in MYI emissivity and a drop of FYI emissivity with high variability during summer months when ice surface or snow cover starts to melt. As for the corresponding changes of radar backscatter, it should be noted that wet snow is a lossy medium at microwave frequencies and therefore its dielectric constant (both real and imaginary parts) increases as wetness increases. The increase of the real part causes an increase in backscattering coefficient from surface scattering,

yet a decrease from volume scattering. The net effect is a decrease of backscattering co-efficient as snow wetness increases up to approximately 4% before it stabilizes. Results to confirm this scenario were verified by Koskinen, Pulliainen, and Hallikainen, 2000 with a snow backscattering model adapted from the Helsinki University of Technology (HUT) semi-empirical forest backscattering model.

The aforementioned drop of MYI concentration, which is associated with a rise of atmospheric temperature, is expected to be replicated by other MYI retrieval algorithms such as the NASA Team (NT) algorithm (Cavalieri, Gloersen, and Campbell, 1984). This algorithm employs the gradient ratio of the brightness temperature between 37 GHz and 19 GHz vertical polarization channels (GR_{37v19v}). Open water, Arctic FYI and MYI have typical values of GR_{37v19v} around 0.06, -0.02 and -0.09, respectively (Cavalieri, Gloersen, and Campbell, 1984). Shokr and Agnew, 2013 found that during warm air spells in the autumn, GR_{37v19v} from MYI approaches zero, which is close enough to the values from FYI. Hence the suggested correction in the current study can also be suitable for applications of NT or any other microwave-based ice retrieval algorithm which depends on radiometric parameters affected by warm air temperature.

6.3   The correction scheme

The correction is based on air temperature as well as the daily change of MYI concentration. It depends on a threshold of an air temperature that triggers the correction process when the daily change of MYI concentration reaches or exceeds another threshold. Additionally, a third threshold on air temperature is required to mark the termination of the correction process.

6.3.1   Outline of the correction

As shown in Figure 6.2, the sudden increase and decrease of MYI concentrations mark the beginning and end of a misclassification period. They correspond to the sharp

increase and decrease in ice surface temperature, respectively. Correction for the misclassification is performed in the following steps (see Table 6.2 for clarification):

First, two flags, F_1 and F_2, are defined. F_1 marks the MYI decrease caused by high air temperature, and F_2 marks the MYI increase due to the return to low air temperature. F_1 and F_2 are set to one when the conditions below are satisfied, respectively:

$$F_1 = 1 \text{ if: } T > T_1, \text{ and } \Delta C_{MYI} < -\Delta C_M \tag{6.1}$$

$$F_2 = 1 \text{ if: } T < T_2, \text{ and } \Delta C_{MYI} > \Delta C_M \tag{6.2}$$

where T is the surface air temperature, ΔC_{MYI} is the daily change of MYI concentration. T_1, T_2 and ΔC_M are the three thresholds used to determine the flags. When condition 6.1 and 6.2 are not satisfied, F_1 and F_2 are set to zero, respectively. The MYI correction starts when F_1 changes from zero to one, and it ends when when F_2 changes from zero to one. In Table 6.2, C_B and C_A denote the MYI concentrations immediately before and after the misclassification period (i.e., September 23 and 27). On the day that marks the start of the correction (September 24), the drop in MYI concentration ΔC_{MYI} (i.e., $C_1 - C_B$ on September 24) must be larger (in absolute value) than the threshold ΔC_M.

TABLE 6.2: An example of the correction in autumn

day in Sep	23	24	25	26	27
F_1	0	1	0	0	0
F_2	0	0	0	0	1
N_{Flag}	0	3	0	0	0
C_{MYI}	C_B	C_1	C_2	C_3	C_A
C'_{MYI}	C_B	C'_1	C'_2	C'_3	C_A

Second, let N_{Flag} be the number of the days of identified misclassification. Wrongly estimated MYI concentrations during this period are replaced by interpolated values based on C_B and C_A. The corrected concentration C'_i for day i is calculated as

$$C'_i = C_B + i * \frac{C_A - C_B}{N_{Flag} + 1}, \; i \in \{1, 2, ..., N_{Flag}\}. \tag{6.3}$$

With this correction, MYI concentrations are always higher than the values before correction.

6.3.2   Threshold adjustment

The three thresholds, T_1, T_2 and ΔC_M, used to define the flags (equation 6.1 and 6.2) in the correction procedure, are selected according to physical and statistical principles. T_1 and T_2 correspond to the temperature when sea ice emissivity (for radiometer data) and dielectric constant (for scatterometer data) both start to change due to snow wetness and freezing, respectively. ΔC_M refers to the sudden change of retrieved MYI concentrations that indicates misclassification due to air temperature rises.

In September, the MYI area in the Arctic may decrease when there is MYI export to more southern regions. On the other hand, it may increase when FYI transforms to be MYI. However, when there is MYI misclassification due to anomalous high air temperature, the calculated MYI area from this algorithm decreases sharply before it restores to its high value when the temperature becomes low again. This is shown by the dip in time series of MYI area as demonstrated in Figure 6.3 on 25 September 2003, reflecting the obvious misclassification shown in Figure 6.1. As a result, the optimal threshold of the aforementioned parameters should produce a temporal record of the corrected MYI area with least and mildest dips (Figure 6.3).

A parameter that represents the severity of misclassification of MYI is introduced, and hence can be an expression of the wrongly estimated MYI area, denoted with A_{mis}. It takes higher values as the number and severity of the dips in the time series increases. This parameter is calculated as shown in the following steps and can be employed as a criterion for optimal selection of the thresholds for T_1, T_2 and ΔC_M.
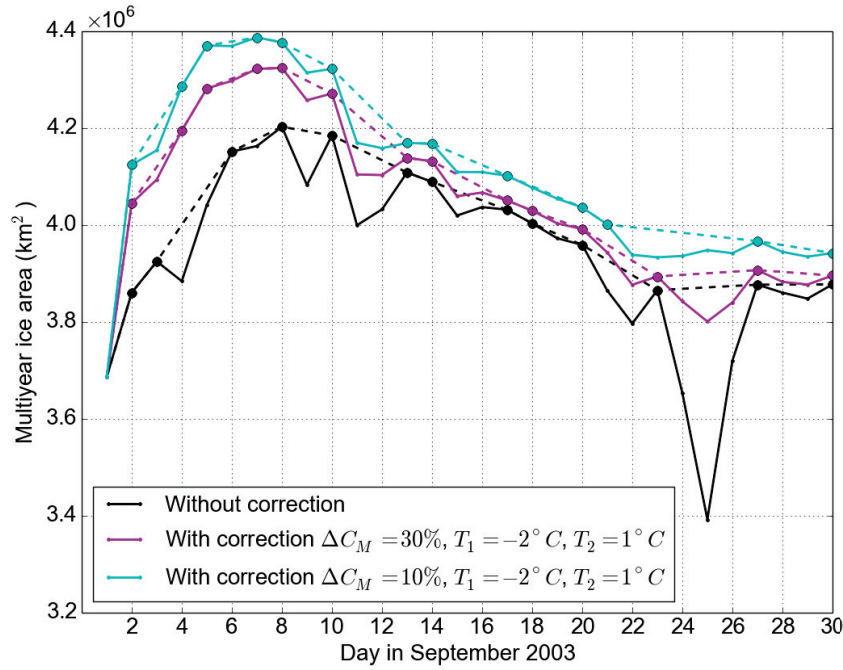
FIGURE 6.3: Multiyear ice area before and after corrections in September 2003. Solid circles denote local maxima in the MYI area time series. The dashed lines denote the MYI area after the linear interpolation based on the local maxima.

First, local maxima of the time series of uncorrected MYI area are identified when the following two inequalities are satisfied:

$$A_{MYI}(i) > \frac{A_{MYI}(i-1) + A_{MYI}(i+1)}{2}, \tag{6.4}$$

$$A_{MYI}(i) > \frac{A_{MYI}(i-2) + A_{MYI}(i+2)}{2}, \tag{6.5}$$

where $A_{MYI}(i)$ is the MYI area on day i. Local maxima in the MYI area time series are shown with solid circles in Figure 6.3.

Second, MYI area of the non-maxima days are linearly interpolated based on the neighbouring local maxima. The local maxima and the interpolated MYI areas constitute a possible upper envelope of the time series of MYI area. The sum of the differences between the upper envelope of the MYI area time series and the original values is the defined A_{mis}. Since the misclassification rarely occurs in October and other months

of autumn (see Table 6.1), A_{mis} in September is used for comparison of the misclassified MYI area in autumn. Smaller A_{mis} indicates less misclassification cases in September, thus it means better correction. This is the criterion used to determine the optimal thresholds.

An experiment was performed to calculate A_{mis} using three sets of thresholds T_1, T_2 and ΔC_M to correct the MYI concentration retrievals in September 2003. The optimal thresholds are those corresponding to smallest A_{mis} and lowest sensitivity to changes of the parameters. Table 6.3 shows the A_{mis} values obtained after corrections with the given combination of the three parameters. A_{mis} for the MYI without correction is 1.67×10^6 km² (not shown in the table), which is much larger than the presented values after corrections. For each set of the thresholds in the table, one parameter varies as shown while the other two parameters remain at the given fixed values. More thresholds were tried in this study and exhibited the same pattern as those in Table 6.3, hence are not shown.

TABLE 6.3: The misclassified MYI area indicator ΔC_M calculated for the MYI retrievals after corrections with different thresholds in September 2003. When ΔC_M varies between 10% and 30%, $T_1 = -2\,°C$, and $T_2 = 1\,°C$. When T_1 varies between $-6\,°C$ and $0\,°C$, $\Delta C_M = 10\%$, $T_2 = 1\,°C$. When T_2 varies between $-1\,°C$ and $3\,°C$, $\Delta C_M = 10\%$, and $T_1 = -2\,°C$.

$\Delta C_M(\%)$	$A_{mis}(10^6$ km²$)$	$T_1(°C)$	$A_{mis}(10^6$ km²$)$	$T_2(°C)$	$A_{mis}(10^6$ km²$)$
10	0.568	-6	0.248	-1	0.557
15	0.585	-5	0.303	0	0.590
20	0.638	-4	0.430	1	0.568
25	0.588	-3	0.482	2	0.567
30	0.663	-2	0.568	3	0.562
		-1	0.542		
		0	0.737		

According to the correction scheme, when smaller values of ΔC_M are used, there are more misclassifications identified and corrected, thus less misclassifications remain. The optimal ΔC_M should then be as small as possible. However, a value smaller than

the retrieval uncertainty leads to unreliable identification of misclassification. Uncertainty of the MYI retrieval from ECICE reaches $5\% - 10\%$. Therefore, 10% is selected as the threshold of ΔC_M.

Snow on top of MYI is nearly salt free, thus its melting point is close to $0\,^{\circ}\mathrm{C}$. Physically, T_2 is preferable to be selected close to $0\,^{\circ}\mathrm{C}$. As shown in Table 6.3, A_{mis} is generally smaller with higher T_2. In addition, A_{mis} becomes quite insensitive to T_2 when it is higher than $1\,^{\circ}\mathrm{C}$. Consequently, $1\,^{\circ}\mathrm{C}$ is selected as the threshold for T_2. As for the threshold for T_1, Table 6.3 shows that A_{mis} varies remarkably with T_1. $-6\,^{\circ}\mathrm{C}$ is the value resulting in smallest A_{mis}, however with strong sensitivity to the changes of T_1. Moreover, being much lower than the melting point of snow, air temperature of $-6\,^{\circ}\mathrm{C}$ does not cause snow wetness on MYI. Therefore, it does not appear to be an appropriate threshold for a parameter indicating snow wetness, i.e., T_1. Another criterion has to be employed instead.
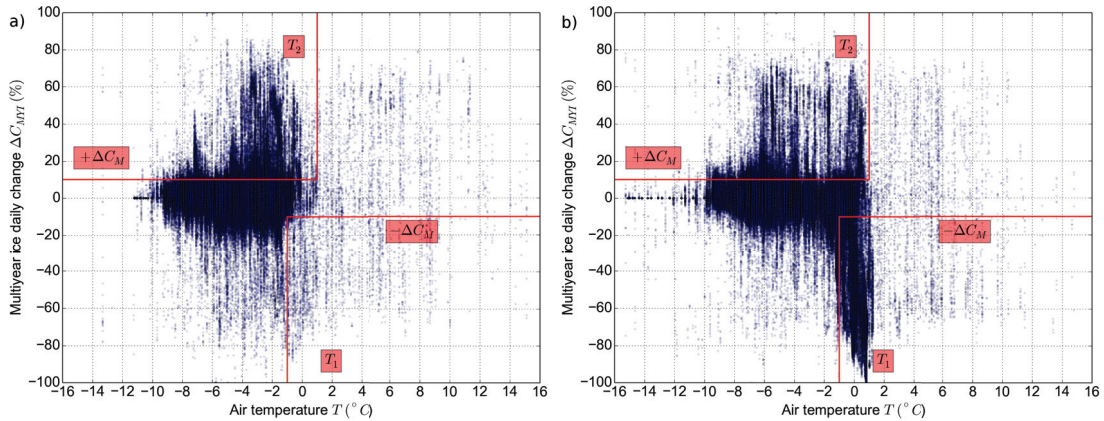

FIGURE 6.4: (**a**) Scatter plot of multiyear ice daily change (ΔC_{MYI}) versus air temperature (T) of September 23 and (**b**) September 25 in 2003

Scatter plots of MYI daily change from the ECICE algorithm (without correction) versus surface air temperature were studied in order to better determine the threshold T_1. Figure 6.4 shows the examples of September 23 and 25, 2003. The regions of pixels fulfilling conditions 6.1 and 6.2 for misclassified MYI pixels are marked by the lower and upper red rectangle, respectively. When there are wide areas of observed MYI anomalies, large amount of data points with high temperatures would appear in the scatter plot with $\Delta C_{MYI} < -\Delta C_M$. For instance, there is a large number of data points

in the lower right rectangle of Figure 6.4b, corresponding to the sudden decrease of MYI on 25 September 2003 (Figure 6.1). In comparison with the scatter plot on September 23 (Figure 6.4a), there are many more data points with large decreases of retrieved MYI concentrations ($\Delta C_{MYI} < -\Delta C_M$) on September 25 (Figure 6.4b). Additionally, the average air temperature for these data points in Figure 6.4b is higher than that in Figure 6.4a. This association leads to the identification of these data points as anomalies, hence warrants the correction. Figure 6.5 shows the normalized probability distribution of air temperature for selected anomalous MYI cases with $\Delta C_{MYI} < -\Delta C_M$ for September from 2003 to 2008 (about $170\,000$ data points in total, red histogram). The selection is based on visual interpretation of anomalies in MYI concentration maps (e.g., sudden decreasing MYI concentrations on 25 September 2003 in Figure 6.1). For comparison, the same pixels were selected from the adjacent days outside the anomalies period (about 4000 data points, blue histogram). For example, the same pixels were selected from September 26 to correspond to the MYI anomalies on September 25 in Figure 6.1). Since the non-anomalous MYI samples from the neighbouring days tend to be in the recovery phase of MYI concentrations (increase of MYI concentrations) or prior to the large decreases, the amount of data points with $\Delta C_{MYI} < -\Delta C_M$ is much smaller than that for the anomalous MYI samples. The value best separating the two clusters of anomalies and non-anomalies, $-1\,°\mathrm{C}$, is selected as the threshold for T_1.

To sum up, the correction with $T_1 = -1\,°\mathrm{C}$, $T_2 = 1\,°\mathrm{C}$ and $\Delta C_M = 10\%$ is regarded to be the best one.

6.4   Results and Discussion

6.4.1   General observations

The correction is applied to anomalies of the MYI concentration retrieval from ECICE from September to December for the six years from 2003 to 2008. Since the suggested correction is only associated with the drop of MYI concentration between consecutive
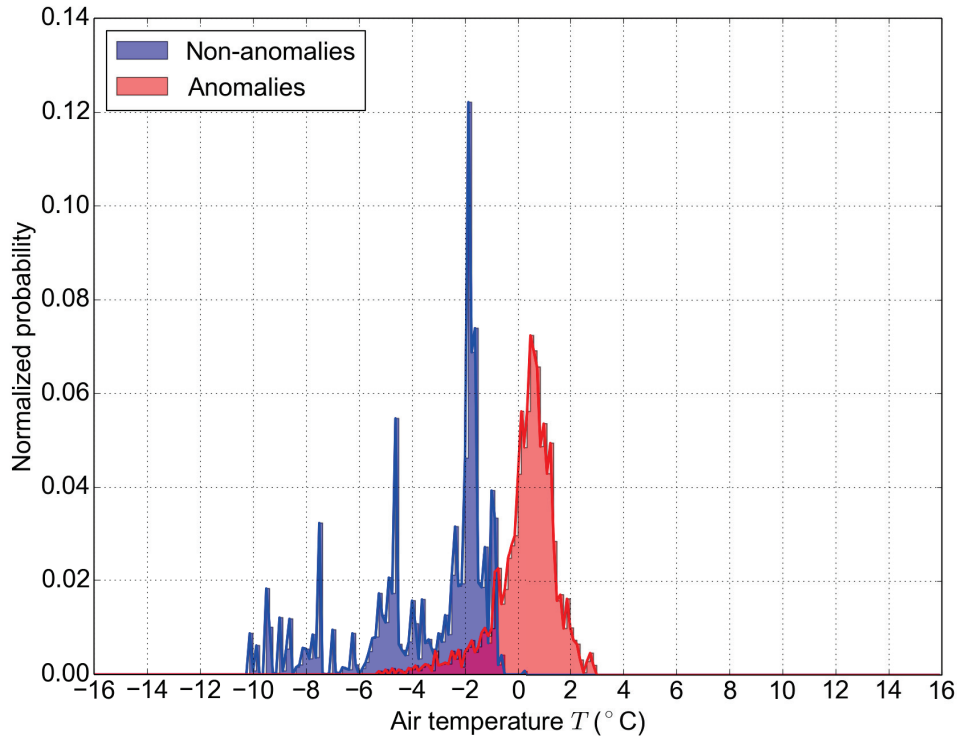
FIGURE 6.5: Probability distribution of air temperature for the non-anomalies and anomalies with $\Delta C_{MYI} < -\Delta C_M$ from 2003 to 2008.

days caused by warm air, it leads to an increase of MYI area. A temporal change in MYI area can also be caused by ice motion. Since there is much less ice motion in the Central Arctic, the identification of anomalies there becomes more authentic than near the ice edge. The identified anomalies are manifested as a switch from MYI to FYI concentration so that the total ice concentration remains unaltered. As shown in Table 6.1, most of the anomalies are found to last between one and two days. The extent of the anomalies inside the ice pack is determined by the extent of the warm temperature spell (Figure 6.1).

A case study of anomalous MYI concentration estimate is shown in Figure 6.6 for September 13, 14 and 15 of 2005. The top and bottom panels show the estimated MYI concentration before and after correction, respectively. In comparison, the correction is most pronounced north of Svalbard on September 14. An extensive area of low MYI concentrations appeared and penetrated into the Central Arctic. It lasted for one day and returned to an area of high concentrations afterwards. It is identified as the
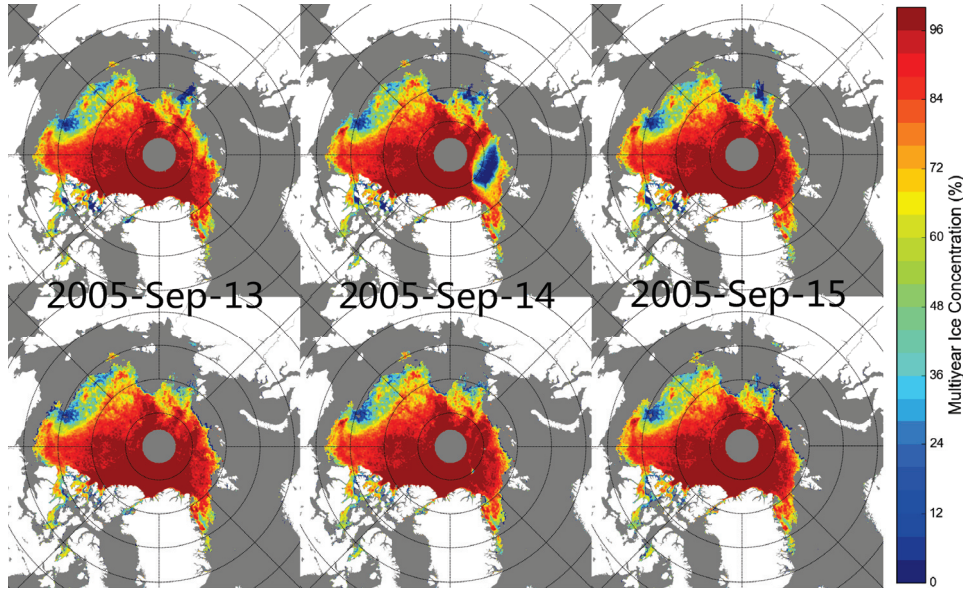
FIGURE 6.6: Maps of uncorrected MYI concentrations from ECICE algorithm (top) and the values after applying the correction scheme (bottom)

misclassification described in Section 6.2, thus the concentration restored after the correction.

6.4.2 Inter-annual variability over the entire Arctic

Figure 6.7 shows the MYI area over the entire Arctic in September before and after correction above latitude 60 °N. A few observations can be drawn from this data set. The difference between the uncorrected and corrected areas diminish by the end of September. This means that the conditions that trigger the correction, particularly the air temperature rise, become less likely to occur in late September and beyond. This was confirmed upon examining the data beyond September (not shown in the figure). For this reason, results from the month of September only are presented in this section.

Figure 6.7 shows also pronounced dips in the uncorrected MYI area that appear to be corrected using the aforementioned approach. The temporal evolution of the corrected area reveals smoother changes from day to day. The increase in MYI area due to the correction is not always associated with visible dips in the uncorrected MYI area, e.g., on September 3, 4 and 5 of 2005. This can be explained by the fact that the adverse effect of warm air temperature that leads to anomalous MYI concentration estimates
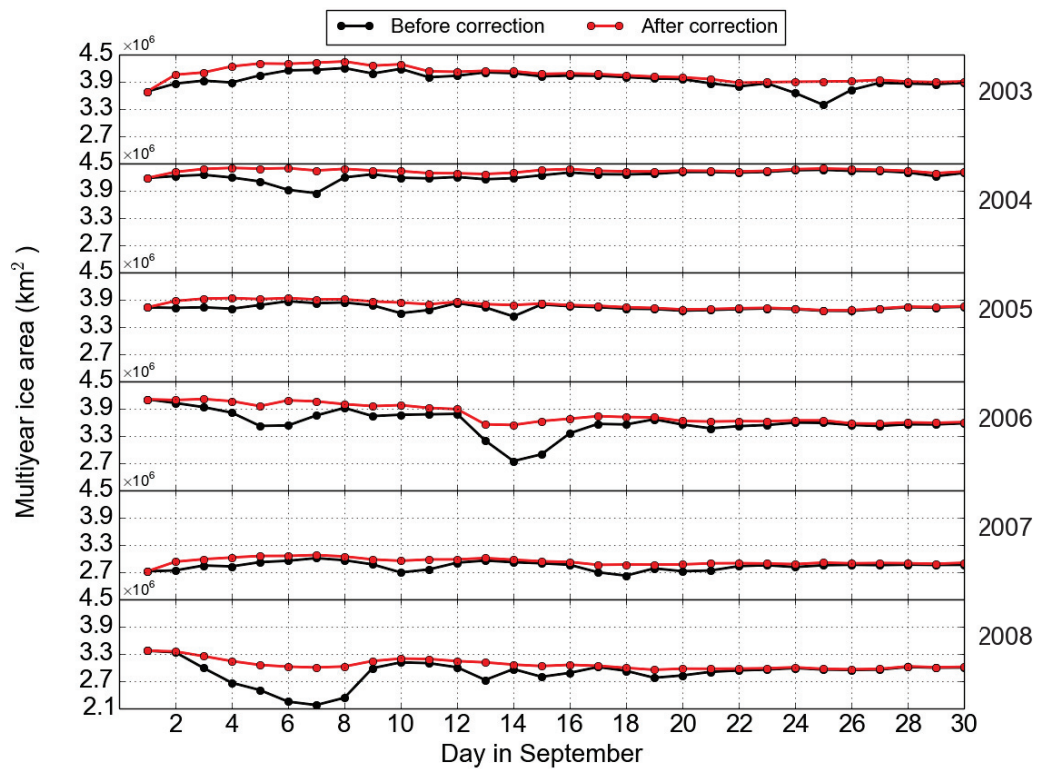
FIGURE 6.7: Arctic multiyear ice area before and after correction in
September 2003-2008

may occur over small regions, which is not manifested in visible dips in the uncor-
rected data averaged over the entire Arctic. In this case, the faulty decrease of the
MYI area due to anomalous temperature is outweighed by an increase in the area due
to the transformation of FYI to MYI. Another remarkable observation from Figure 6.7
is the gradual increase of MYI area during the first few days in September, followed
by an apparent decrease before the area stabilizes toward the end of September. The
increase is a manifestation of the transition of FYI to MYI. It occurs in the beginning
of September although the operational ice monitoring centers use October 1 to mark
this transition (Canadian Ice Service–personal communication). The subsequent de-
crease of the MYI area, noticeable during mid-September, is an indicator of the MYI
drift away from the pack ice (mainly being exported through the Fram Strait to lower
latitudes) (Kwok and Rothrock, 1999; Kwok, Cunningham, and Pang, 2004; Kwok,
2009). The pack ice remains relatively loose during this period before it becomes more
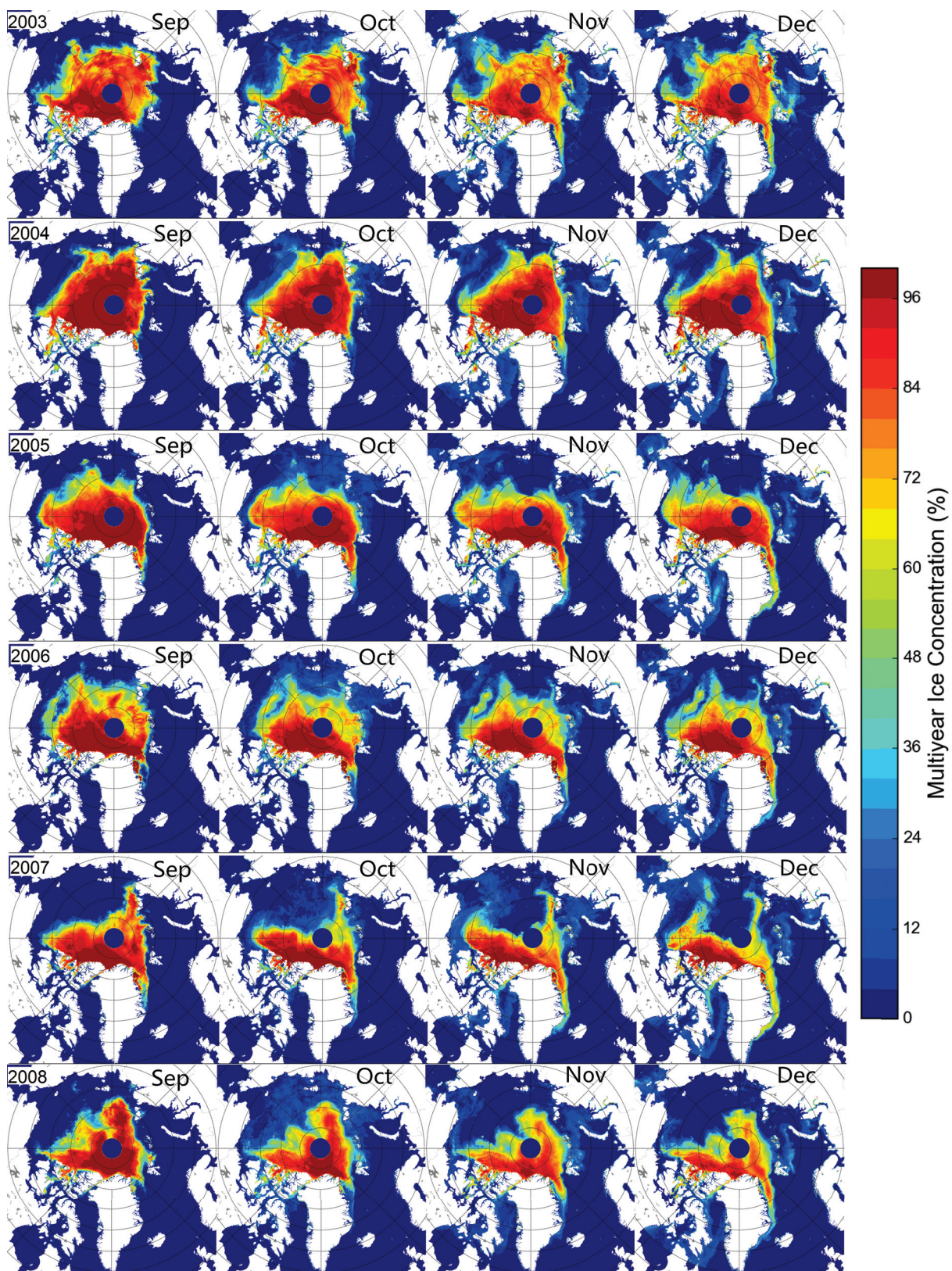consolidated as winter approaches.

FIGURE 6.8: Monthly average multiyear ice concentration after correction
in September, October, November and December of 2003-2008

The monthly average MYI concentration from September to December for the years from 2003 to 2008 is shown in Figure 6.8. In all the six years, the Arctic MYI decreased from September to December. Main cause of the MYI loss can be seen from the maps, which is the MYI export to southern regions through the Greenland Sea. In warm years such as 2005 and 2007, there is also MYI flowing out of the Central Arctic through the Baffin Bay. Among all the regions, MYI in the Beaufort and East Siberian Seas has the biggest inter-annual and seasonal variability, which is highly influenced by the Beaufort Gyre and the Transpolar Drift. This is reflected in the declining trend of the Arctic MYI coverage from 2003 to 2007. Contribution of melt in the Beaufort Sea to the decline in Arctic MYI coverage was studied by Kwok and Cunningham, 2010. It reveals that the net melt area in the Beaufort Sea between 2005 and 2008 accounts for nearly 32% of the net loss of Arctic Ocean MYI coverage over the same period. The MYI variability in September along with the ice climatology between different regions are presented in the next section.

TABLE 6.4: MYI area statistics before and after correction, the minimum and average total sea ice area in September 2003-2008, calculated over the entire Arctic ice cover

area (10^6 km^2)		2003	2004	2005	2006	2007	2008
avg.MYI	before correction	3.940	4.230	3.724	3.590	2.837	2.881
	after correction	4.060	4.339	3.791	3.786	2.937	3.069
	difference	0.120	0.109	0.067	0.195	0.101	0.188
max.MYI	before correction	4.203	4.362	3.869	4.110	3.011	3.372
	after correction	4.349	4.404	3.938	4.116	3.080	3.372
	difference	0.146	0.042	0.069	0.006	0.069	0
Total ice	minimum	4.989	4.961	4.575	4.816	3.470	3.709
	average	5.253	5.265	4.819	5.031	3.654	4.016
avg.Total ice - avg.MYI		1.193	0.926	1.028	1.245	0.717	0.948

Statistics of MYI area in September before and after correction over the entire Arctic (above latitude 60 °N) are presented in Table 6.4, along with the average and minimum total ice area for each of the years studied. The limited temporal data presented in the table reveals a declining trend of MYI area, which is particularly remarkable in 2007.

It agrees well with the studies by Maslanik et al., 2007; Nghiem et al., 2007; Kwok and Cunningham, 2010; Maslanik et al., 2011; Comiso, 2012. The average area dropped by 0.849×10^6 km^2 in 2007, compared to 2006. The difference between the uncorrected and corrected areas (average or maximum) does not suggest any inter-annual trend. Larger difference indicates more warm air spells and vice versa. Except for the year 2005, the correction reclassifies over 0.1×10^6 km^2 FYI as MYI. In 2005 this value reaches a minimum of 0.067×10^6 km^2. Data in the table shows that the maximum MYI area is always smaller than the minimum sea ice area. This is an evidence of correctness of the calculations. High correlation is found between the minimum area of total sea ice and the maximum area of MYI in September (0.986 before correction and 0.991 after correction). Such correlation is also found between the former parameter and the average area of MYI in September (0.950 before correction and 0.966 after correction). While there is an apparent inter-annual decline of both total sea ice and MYI area within the limited number of years in the data set, the difference between the two parameters is neither constant nor showing an identifiable trend. More data over the rest of the freezing season and for more years are needed to establish a record of the ratio between MYI and total ice area.

6.4.3   Temporal and Spatial variability between regions

As shown in Figure 6.8 the distribution of MYI varies across the Arctic domain. Statistics of MYI concentration and area are obtained in seven regions to provide a representative picture of climatological ice characteristics in relation to the trait of each region. The selected zones are shown in Figure 6.9. MYI usually concentrates around the center of the Arctic Basin. The MYI in the southern part is less concentrated and varies between regions. It should be noted that low air temperature in summer leads to large area of MYI, whereas high temperature in September leads to underestimation of the area. The influence of air temperature and the correction in each region is presented in this section.
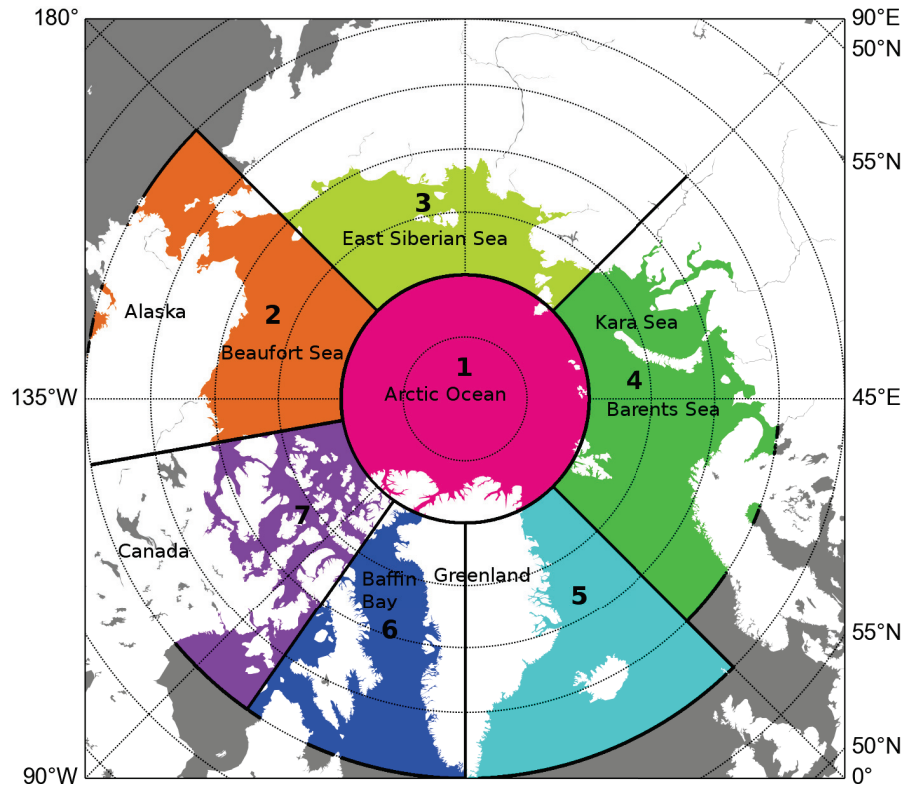
FIGURE 6.9: Map of the Arctic showing the seven regions selected for the MYI area study

Region 1 covers the Arctic Basin with latitude over $80\,°$N, including the major amount of the Arctic MYI. It features large scale circulation of sea ice, which is highly impacted by the North Atlantic Oscillation and the Arctic Oscillation (Kwok, 2000; Rigor, Wallace, and Colony, 2002). Region 2 includes the Beaufort and Chukchi Seas. It features a clockwise circulation, the Beaufort Gyre, caused by an average high-pressure system (McLaren, Serreze, and Barry, 1987; Serreze, Barry, and McLaren, 1989). Large scale (hundreds or thousands of kilometers) ice motion prevails, which causes continuous breakup and consolidation of the ice cover. This is reflected in continuous MYI concentrations throughout the freezing season. The effect of synoptic climatology of atmospheric forcing on sea ice motion in this region was studied by Asplin, Lukovich, and Barber, 2009. Lag correlations are found between synoptic weather types and sea ice vorticity. In Region 3, which covers the Laptev and East Siberian Seas, dynamic forcing triggered by wind or surface currents has equal influence on ice extent variability as thermodynamic forcing. The MYI does not extend very far south in this region.

Region 4 includes the Kara and Barents Seas. It has less ice cover in general and MYI in particular. This is because warm water is carried into this region by the Gulf Stream through the North Atlantic. The ice melt in summer is particularly extensive. Detailed record of winter sea ice extent in the Barents Sea (1967-2005) is presented in Sorteberg and Kvingedal, 2006. Region 5 features strong ice drift that originates in the Central Arctic and is triggered by another major atmospheric circulation, the Transpolar Drift Stream. It moves the ice from the Arctic Basin to the North Atlantic off the east coast of Greenland. Region 6 also features strong ice drift heading south parallel to the eastern coast of Ellesmere Island. In Region 7, which mainly encompasses the narrow passages in the Canadian Arctic Archipelago, MYI replenishment from FYI contributes to heavy sea ice conditions. The inter-annual variability of this ice from 1997 to 2013 is presented in Howell et al., 2015.
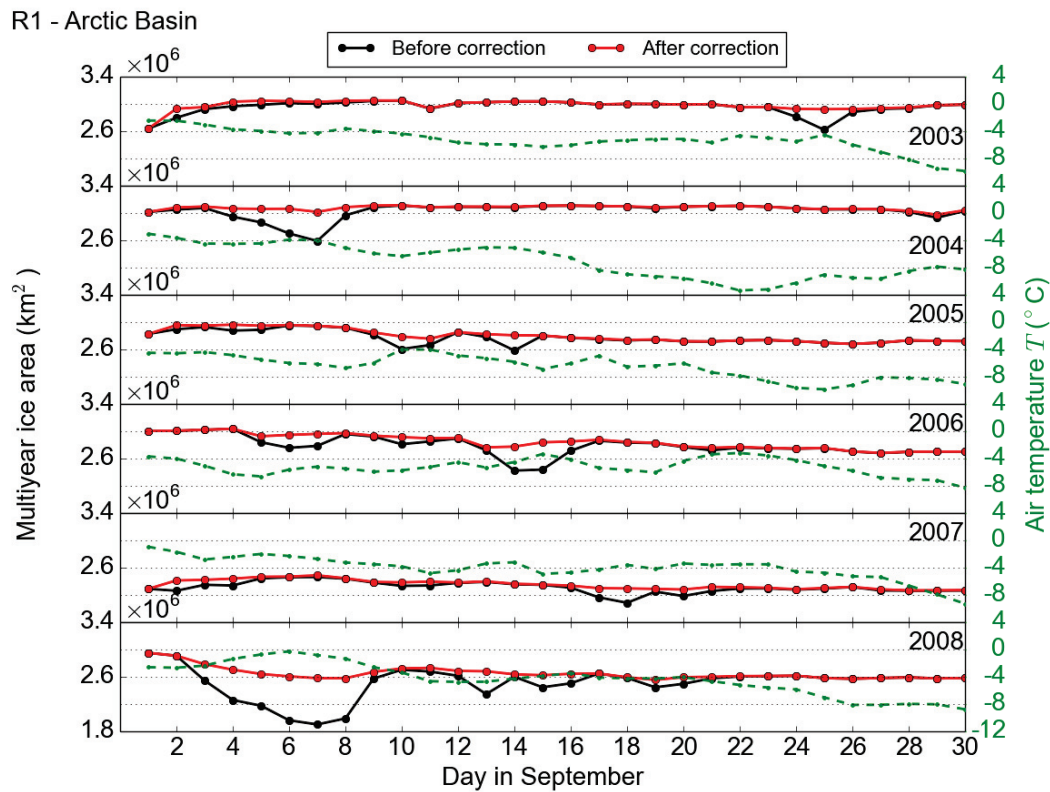

FIGURE 6.10: Daily evolution of MYI area in September in the Arctic Basin, showing the area before and after correction along with the average temperature.

Results of the daily MYI area during the month of September in each region are

presented in Figure 6.10 and Figure 6.11. Also shown are records of the average air temperature over ice. Major anomaly events (identified in the uncorrected data) are observed in all regions except Regions 5 and 6, which have remarkably fewer events and much smaller MYI area. The pertaining graphs show that even when the temperature rises to near melting degrees, anomalies may not be numerically apparent.

As mentioned before, the MYI area changes between different zones and from year to year. Two factors that contribute to the changes are the conversion of FYI to MYI (causing an increase) and the ice dispersion due to its mobility (causing a decrease). The MYI area in Region 1 highly determines changes of MYI in the entire Arctic. The data in Figure 6.10 shows a constant MYI area in September of 2003 and 2004 (about 3.0×10^6 km^2) and continuous decreases through the same month of other years. The decreases were between 0.1×10^6 km^2 and 0.4×10^6 km^2. Warm air spells were observed by the temperature record in the six years, leading to MYI area increases up to 0.6×10^6 km^2 due to the correction (e.g., on September 7 2008).

In Region 2 the area remained virtually unaltered except in 2006 when it decreased from about 7.0×10^5 km^2 to 5.0×10^5 km^2. The correction on 14 September 2006 did not completely restore the area to the value that matches those from the days before. In Region 3 a small gain in MYI area (around 1.0×10^5 km^2) was observed during the first few days in September of 2003 and 2005, followed by a gradual decrease. MYI area decreased at a moderate rate in each year expect for 2007 when it remained constant. The decrease was above 1.0×10^5 km^2. The MYI area in Region 4 was significantly smaller (below 0.2×10^5 km^2) except in 2003 and remained nearly constant throughout the month. In Region 5 the MYI area increased at a moderate rate except in 2008 when it was nearly constant throughout September. The MYI area in Region 6 was as small as that in Region 4 (except in 2003) and exhibited a continuous increase throughout the month. MYI in Region 5 and 6 is mainly imported from the Arctic Basin and transported further south by the Transpolar Drift.

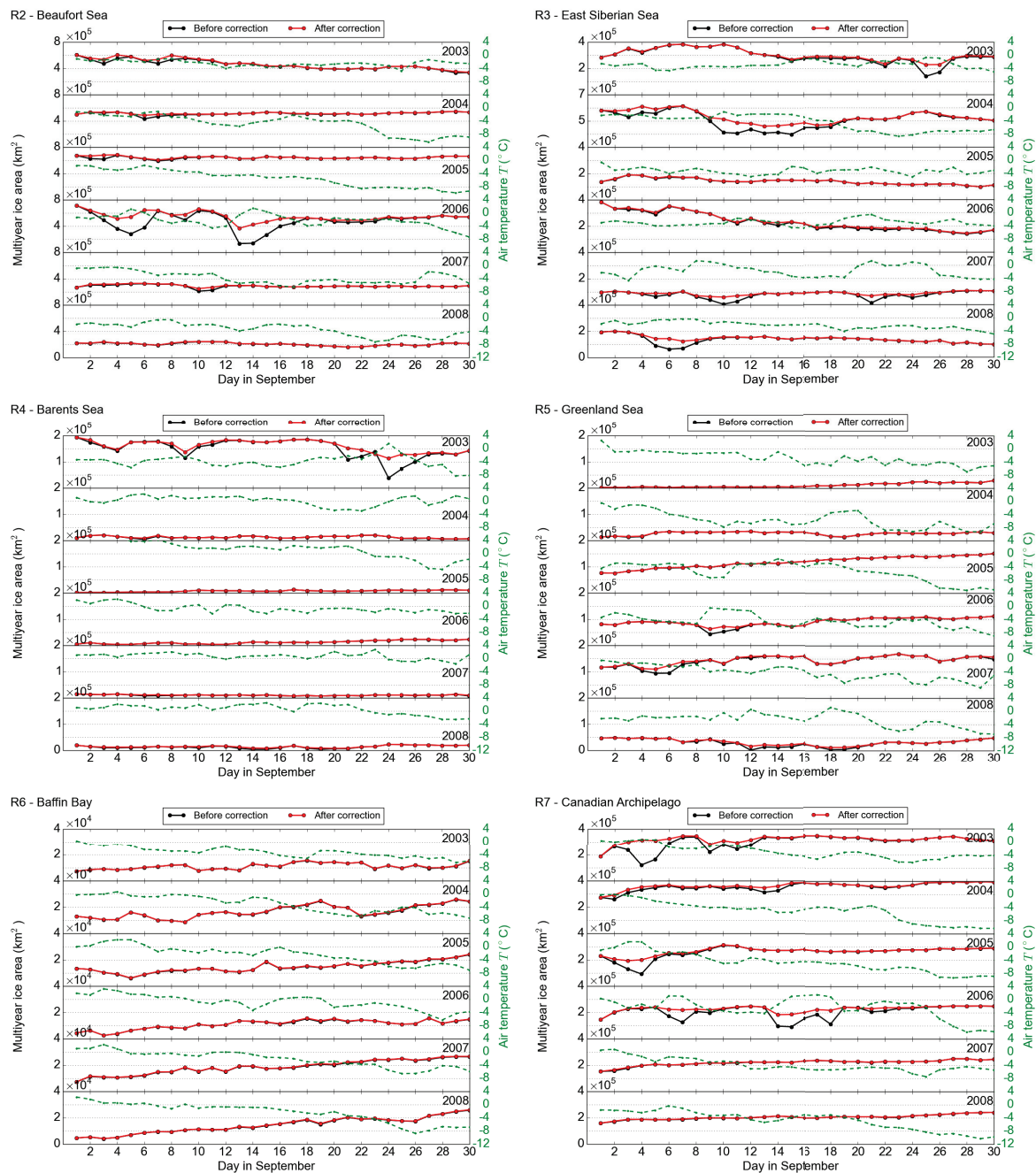Region 7 is particularly important because the presence of MYI, even with small

FIGURE 6.11: Daily evolution of MYI area in September in Regions 2 to 7 (Fig. 6.9), showing the area before and after correction along with the average temperature.

amount, represents the most significant hazard to marine navigation within the Northwest Passage. This passage is expected to be open for longer periods as a result of the Arctic climate warming. The extreme light years of MYI within the Canadian Arctic Archipelago are studied in Howell et al., 2013 and found to be associated with longer navigation seasons within the Northwest Passage. Figure 6.11 shows an increase of MYI area during the first week in September. This indicates import of MYI from the Central Arctic or local production of MYI from transformation of FYI. The MYI area then stabilizes when the ice becomes fully consolidated by mid-September. It is shown that the stable MYI area decreased gradually from about 4.0×10^5 km^2 in 2004 to about 2.5×10^5 km^2 in 2008. This impact of the well-recognized warming trend of the Arctic region has been confirmed in Howell et al., 2015. There are two obvious warm air spells in September 2006 as shown by the temperature record in the graph (September 7 and 15), resulting in MYI area increases of 1.0×10^5 km^2 after the correction.

As shown in Figure 6.12, the MYI area in Region 1 is the largest and undergoes an obvious trend of decline following the trend of the MYI area in the entire Arctic. The MYI in this region comprised about 75% of the MYI in the entire Arctic in years 2003 throughout 2006. This ratio increased to about 83% in 2007 and 2008, implying that the annual loss of MYI occurs more at the peripheral of the Arctic ice cover. In general, the MYI area in most regions (Regions 1, 2, 3 and 7) had a generally declining trend from 2003 to 2008. This confirms similar findings in previous studies (Kwok, 2007; Kwok and Cunningham, 2010; Comiso, 2012).

The MYI area in Regions 2 and 3 had the largest variability among the six regions in Figure 6.12 b. The effect of the correction is most pronounced in 2006 in Region 2. It should be noted that the MYI area in Regions 1, 2 and 3 had substantial decreases in 2007. The Arctic ice extent settled a record minimum in September 2007 (as confirmed in Table 6.4), yet its impact was mostly limited to the ice in the western Arctic regions (Regions 2 and 7) (Comiso, 2006a; Maslanik et al., 2007). Region 4 (the Barents Sea) had a limited MYI coverage (nearly 1.6×10^5 km^2) in 2003, which almost vanished in the following years. It makes this region similar to Region 6 (the Baffin Bay) in that both

are nearly MYI free. Region 5, on the other hand, had noticeable amount of MYI being exported from the Arctic Basin through the Fram Strait into the North Atlantic. Yet the amount varied between 0.1×10^5 km^2 and 1.3×10^5 km^2 as shown in Figure 6.12 b. The considerable increase on MYI area from 2003 to 2007 is an indicator of the increasing ice discharge through the Transpolar Drift. In Region 7, the MYI area increased from 2003 to 2004 because the imported FYI from the Central Arctic was promoted to MYI in late September (as confirmed in Figure 6.11). This replenishment virtually stopped from 2005 to 2008, resulting in monotonic decreases in MYI area, which is also found in Howell et al., 2008.
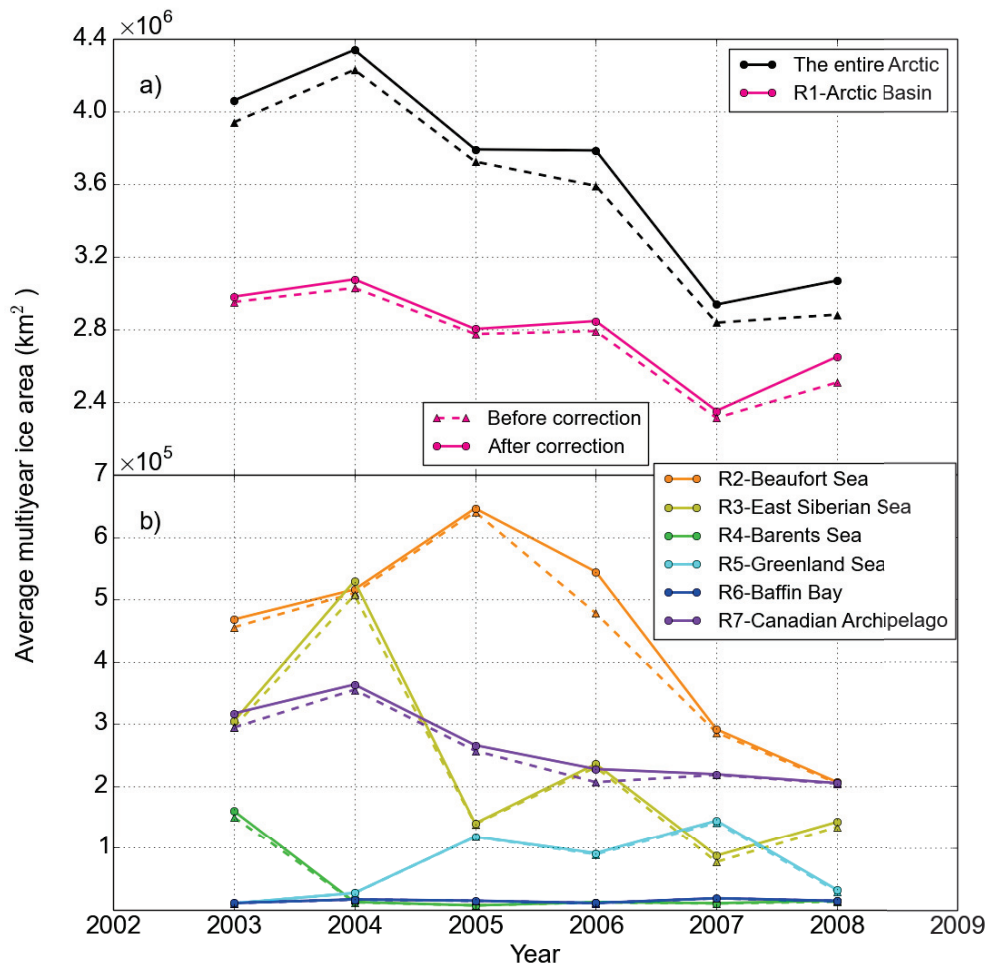

FIGURE 6.12: Average MYI area before (dash lines) and after correction (solid lines) in September of 2003-2008 in the entire Arctic and the seven regions.

6.5   Conclusions

During warm spells in autumn, anomalous brightness temperature and backscatter from MYI were observed, which are similar to those from FYI. The anomalous radiometric observations lead to misclassification of MYI as FYI, thus resulting in erroneous low MYI concentration retrieval under this situation. A correction based on air temperature is suggested and applied to the MYI concentration retrieval from the ECICE algorithm (output ice types and their concentrations) from September to December for the six years from 2003 to 2008.

As the correction is designed to restore the low MYI concentration to high values, MYI concentration after correction is overall higher than that before correction. For September of the six years, the correction introduces over 0.1×10^6 km^2 MYI area except for 2005. The difference between the uncorrected and corrected MYI areas diminishes by the end of each September.

The corrected MYI concentration maps confirm that the Arctic MYI area is generally declining from 2003 to 2008, and reaches a minimum in 2007. In each year, MYI export through the Greenland Sea is observed from September to December, leading to the MYI loss in the period. Due to the Beaufort Gyre and the Transpolar Drift, MYI in the Beaufort and East Siberian Seas has larger inter-month and inter-annual variability than other regions (except for the Arctic Basin).

To conclude, the correction works well by replacing anomalous MYI concentrations with interpolated ones. It could be applied as a post processing to all the microwave-based MYI retrieval algorithms, such as the NASA Team algorithm (Steffen and Schweiger, 1991; Ye and Heygster, 2015), the NORSEX algorithm (Svendsen et al., 1983), the UMass-AES algorithm (Swift, Fedor, and Ramseier, 1985) and the ECICE algorithm (Shokr, Lambe, and Agnew, 2008). As the influence of warm air spells is regionally limited, the correction might be much more important in operational applications where ice concentrations are crucial on small and meso scale, e.g., continued updating of safety guidelines for shipping routes.

Chapter 7

Improving MYI concentration estimates with ice drift

7.1   Motivation

MYI concentration can be retrieved from passive and active microwave remote sensing observations. One of the algorithms that combine both observations is the ECICE algorithm. However, factors such as ridging, snow wetness and metamorphism can cause significant changes in brightness temperature and backscatter, leading to misidentification of FYI as MYI, hence increasing the estimated MYI concentrations suddenly. This chapter introduces a correction scheme to restore the MYI concentrations under these conditions. The correction utilizes ice drift records to constrain the MYI changes and uses two thresholds of passive microwave radiometric parameters to account for snow wetness and metamorphism. The correction is applied to MYI concentration retrievals from ECICE with inputs from QuikSCAT and AMSR-E observations, acquired over the Arctic region in a series of winter seasons (October to May) from 2002 to 2009. The Radarsat-1 SAR images and ice export from Fram Strait are compared with the MYI concentrations before and after correction to assess the performance of the correction.

7.2   Misclassification of FYI as MYI

As described in Shokr and Agnew, (2013), when the atmospheric temperature approaches the melting point, the MYI concentration retrieval from ECICE shows a sharp increase. Moreover, sudden appearance of MYI near the ice edge is frequently observed in the output maps. These observations cannot be explained by the motion of MYI because the large distance renders it infeasible. Formation of MYI in new locations is also not possible in the spring. Hence, the sharp increase of MYI concentration (accompanied with an equal drop in FYI concentration) is regarded as misclassification. These anomalies are observed mainly in late winter and early spring (from February to May) and may last for a few days or weeks or sometimes for the rest of the season. During such periods, the brightness temperature from FYI decreases and the backscatter increases to values close to those of MYI. Unlike the radiometric effect of warm spells on the snow-covered MYI (Tonboe, Andersen, and Toudal, 2003; Shokr and Agnew, 2013; Ye, Heygster, and Shokr, 2015), which ends after the low temperature returns, the effect on the snow-covered FYI shows long-term or irreversible behaviour even when the warm spell abates. One explanation can be that the snow on FYI retains some salty solute, which is partly or totally drained when the snow becomes wet. Such irreversible processes renders the misclassification of FYI as MYI in winter/spring more durable even when the warm spell abates. A correction scheme based on ice motion is suggested and described in the next section.

An example of the described anomaly is presented in Figure 7.1. On 7 April 2003, warm air is advected over the Barents Sea. On 8 April, non-zero MYI concentration appears suddenly west of Novaya Zemlya and the concentration approaches 100% on 9 April, whereas the corresponding FYI concentration decreases to near 0%. The identification of MYI in this region is not correct since it can not have grown locally or been advected from the main pack to such a far distance in two days. Thus the increasing MYI concentrations from 8 April to 21 April west of Novaya Zemlya must be incorrect. This anomaly stays in the region for over three weeks and disappears
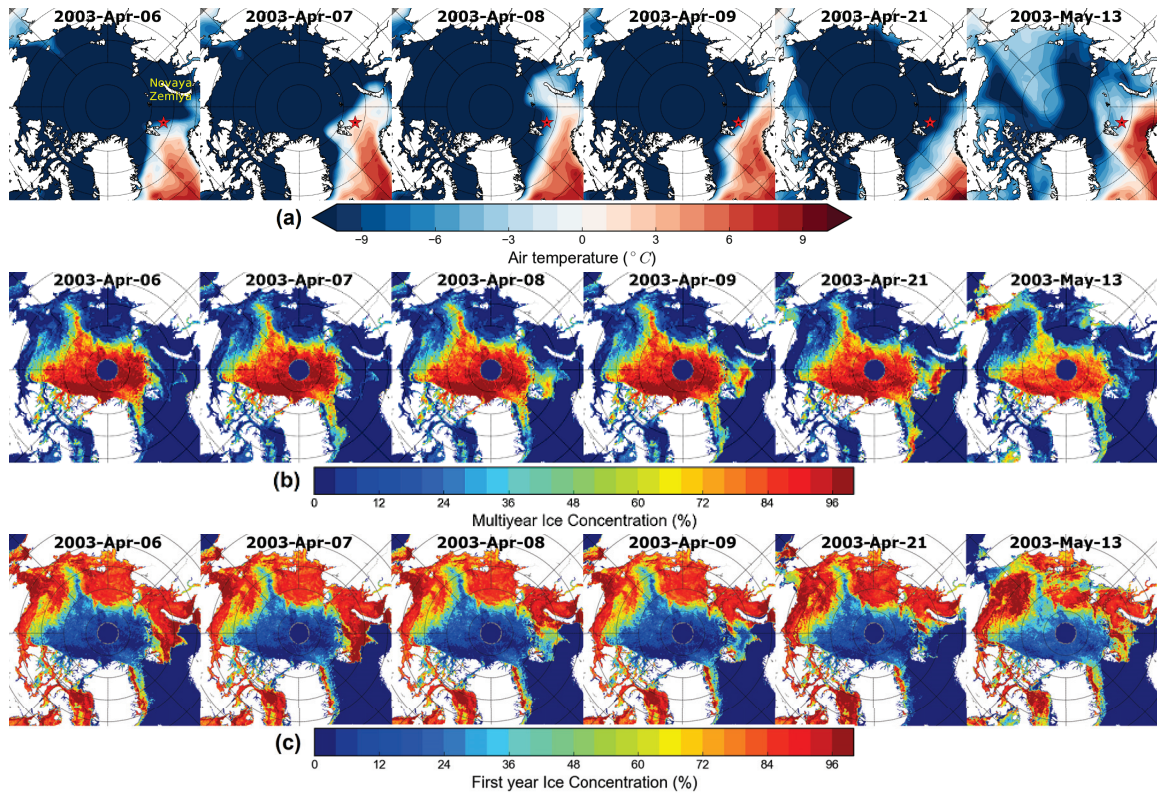
until 13 May.

FIGURE 7.1: (**a**) Surface air temperature from the ERA-Interim reanaly-
sis (Dee et al., 2011), (**b**) multiyear ice concentration, and (**c**) first-year ice
concentration retrieved from ECICE from April 6 to May 13, 2003. The red
stars indicate the sample region that will be mentioned in Figure 7.2.

Figure 7.2 shows the daily records of MYI and FYI concentrations, air tempera-
ture, brightness temperature and backscatter from all pixels within an area bounded
by 76.75°–77°N latitude and 29°–30°E longitude (red start in Figure 7.1a) in the Bar-
ents Sea from 1 October 2002 to 31 May 2003. The five vertical blue lines in the figure
correspond to the days with sudden increases of MYI concentration. The first case oc-
curs at the end of October, when concentration of MYI and FYI both increases from 0%
to about 20%. This increase is not caused by misclassification but ice advection from
nearby regions. From 1 December to 9 December, the MYI concentration increases by
about 50%. Shortly before this MYI increase event, air temperatures rise above 0 °C and
drop to cold temperatures again when the event starts. This melt-refreeze cycle leads to
persistently increasing QuikSCAT backscatters, while the AMSR-E brightness temper-
atures strongly increase from one day to the next before the event but return to values

similar to the ones before the event on 9 December. A potential explanation for this situation is the combined effect of ice deformation and snow melt-refreeze cycle. As confirmed from the daily sea ice drift product of NSIDC, direction of ice drift changes abruptly from one day to the next, which is likely to cause ice deformation in the studied area and can be considered as an evidence for the hypothesis. The third case happens on 15 February, when the MYI concentration increases from 0% to 20% and the total ice concentration keeps unaltered. Again, the air temperature rises to near zero shortly before the event and is followed by cold temperatures (about $-10\ °C$), which indicates a melt-refreeze episode on FYI. This results in decreased brightness temperatures and increased backscatters, which causes the false MYI concentration increase. Similar conditions can be found in the cases of 8 April and 16 May.

The described increase of MYI concentration is expected to be replicated by other MYI concentration retrieval algorithms. For example, Voss, Heygster, and Ezraty, (2003) noted that increased volume scattering after the melt-refreeze episodes in late winter results in unrealistic high estimates of MYI concentration from the NASA Team algorithm, which uses radiometer measurements only. The radiometric responses to the melt-refreeze events lead to overestimates of MYI concentration from other microwave-based ice retrieval algorithms as well. Hence the suggested correction in the current study is also suitable for applications of any other microwave-based ice retrieval algorithm.

Microwave emission and scattering from snow is affected by snow density, salinity, temperature, wetness and grain morphology (Fuhrhop et al., 1998). Snow on FYI is characteristically (and therefore radiometrically) different from snow on MYI. The FYI surface is usually saline, and the overlain snow wicks up the brine through capillary action. When air temperature approaches sub-zero values during the freezing season, snow becomes wet. If the temperature decreases again, liquid water in the snow will aggregate small crystals to coarsely grained clusters with larger voids between the grains. These are permanent changes. On the other hand, snow on MYI is saline-free and has mostly metamorphosed into crystalline structure since it has been

exposed to cycles of high and low temperatures. In this case, the effect of a warm spell will be manifested in measurable wetness, and if the temperature decreases again the snow will retain its physical structure and composition. This makes it easier to account for the effect of warm air temperature on snow on MYI as described in details in Ye, Heygster, and Shokr, (2015).
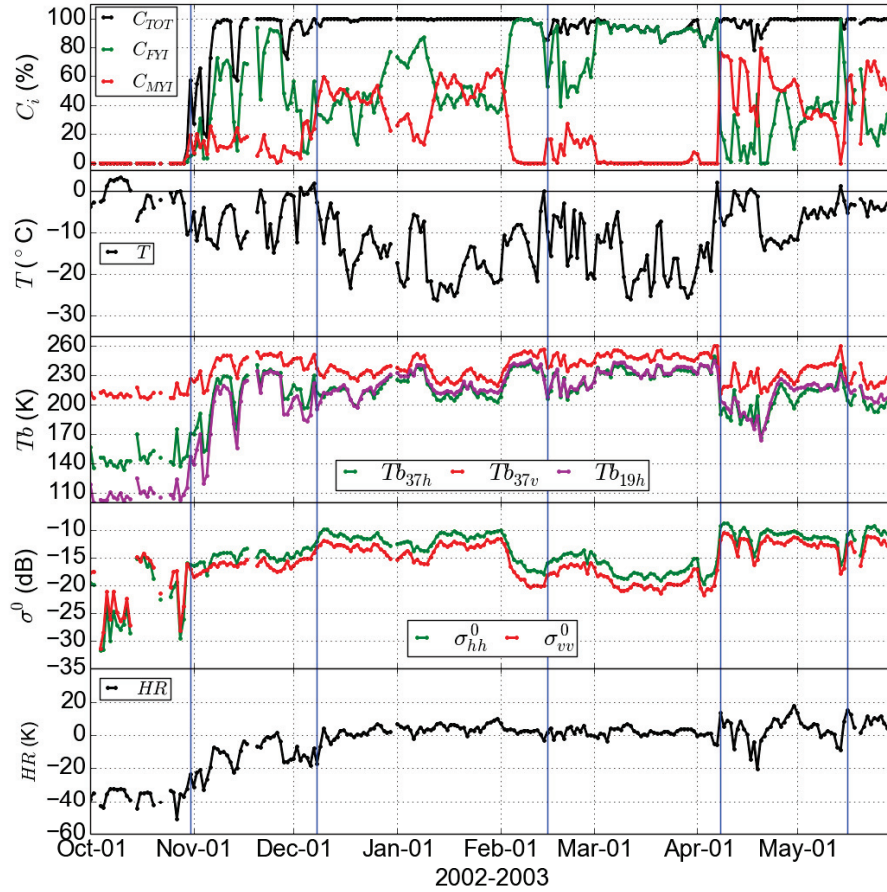

FIGURE 7.2: Averaged multiyear (C_{MYI}), first-year ice concentration (C_{FYI}) and total sea ice concentration (C_{TOT}), surface air temperature (T), brightness temperature (Tb_{37h}, Tb_{37v} and Tb_{19h}), backscatter (σ^0_{hh} and σ^0_{vv}) and horizontal range ($HR = Tb_{19h} - Tb_{37h}$) of a selected region in the Barents Sea (latitude: $76.75° - 77°$N, longitude: $29° - 30°$E, as the red stars shown in Figure 7.1a) from October 2002 to May 2003. The five vertical blue lines correspond to the five events of sudden increases in MYI concentration as described in the text.

The impact of air temperature changes (warm/cold cycles) on the microwave observations is complex and remains unclear. Findings from the many studies of snow on sea ice continue to raise questions more than providing answers (Shokr and Sinha, 2015). A few guiding notions to assist in the interpretation of the above-mentioned

anomalies of microwave-based ice concentration retrieval are summarized below. Two factors are addressed: snow wetness and snow metamorphism into larger grain size.

When there is wet snow on sea ice, the emitted radiation is less at the horizontally-polarized channel of 19 GHz than 37 GHz (Comiso, Ackley, and Gordon, 1984; Shokr, Asmus, and Agnew, 2009). The difference can be used as an indicator of the amount of snow wetness (Anderson, 1997; Drobot and Anderson, 2001). For radar backscatter, snow wetness affects both surface and volume scattering. Surface scattering increases and volume scattering decreases as snow wetness increases. The net effect is a significant decrease of backscatter as the snow wetness increases to about 3% then it stabilizes (Koskinen, Pulliainen, and Hallikainen, 2000). A study presented in Barber, (2005), however, shows that the melt onset of FYI is marked by a rapid increase in backscatter as the wet snow becomes more reflective of the microwave energy. Therefore, the observed misidentification of FYI as MYI would probably be attributed to wet snow with its combined effect on both emitted microwave and radar backscatter signal (recall that both observations are used in the retrieval). Snow metamorphism increases the volume scattering, resulting in decrease of emissivity (and therefore brightness temperature) and increase of radar backscatter. The effect of snow grain size on radar backscattering has been studied by Du, Shi, and Rott, (2010) using a multiple scattering model. The authors showed an increase of backscatter coefficient at vertical polarized Ku-band from -15 dB to -2 dB as the radius of snow grains increases from 0.5 mm to 1.5 mm. This brings the backscatter up to typical values of MYI and that is what triggers the observed anomalies. The correction scheme accounts for the effects of snow wetness and metamorphism with two different parameters as will be shown in the next section.

7.3 The correction scheme

7.3.1 Outline of the correction scheme

As described in Section 7.2, ice deformation, snow wetness and metamorphism can cause significant changes in microwave brightness temperature and backscatter, leading to misidentification of FYI as being MYI, the effects of which are considered here. In many situations the affected pixels are found to be located far from the main pack ice, particularly in the eastern Arctic such as the Laptev Sea, the Barents Sea, and the Greenland Sea. This is expected because near- or above-freezing temperatures are more frequently encountered in these regions. Warm temperatures enhance the possibility of the anomalous microwave signatures. For a given day, pixels with MYI concentration over 15% are identified. These pixels constitute the so-called MYI domain (the red box in Figure 7.3a) of the given day. With the daily ice motion vector, this MYI domain is expanded accordingly to produce a new MYI domain (the purple contour in Figure 7.3b). For pixels that are located outside the new domain (the yellow region in Figure 7.3c), MYI concentrations of the second day are corrected without checking any radiometric indicator of snow wetness and metamorphism (described later in this section). For pixels within the new domain (the purple region in Figure 7.3c), the indicators should be checked to confirm that the originally-estimated concentrations (in our case from the ECICE algorithm) are indeed anomalous (pixels have abrupt increases of MYI concentrations on the two successive days) and therefore needs correction. The correction proceeds as follows.

First, for each pixel, a flag, F_i, is defined. $F_i = 1$ when the MYI concentration is over 15% on day i. Otherwise, $F_i = 0$. Pixels with $F_i = 1$ constitute the originally-estimated MYI domain of day i (the red box in Figure 7.3a). For pixels within the domain, daily ice drift is used to calculate the expected displacement after one day (*i.e.*, on day $i + 1$). The MYI domain is expanded according to the displacement, consequently generating a new MYI domain. It should be noted that the MYI domain is only expanded when the examined pixel inside the original MYI domain is advected out of it. Pixels within
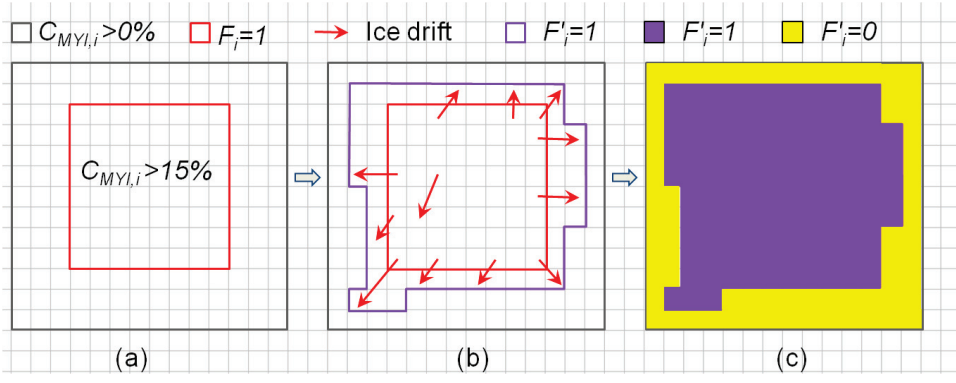
FIGURE 7.3: Flowchart of the correction procedure.

the new domain are indicated with $F_i' = 1$ (the purple region in Figure 7.3c), whereas those outside the domain have $F_i' = 0$ (the yellow region in Figure 7.3c). $F_i' = 0$ means that there should be no MYI on day $i + 1$, whereas $F_i' = 1$ implies that there could be MYI on the next day (*i.e.*, day $i + 1$) based on the estimation from ice motion and previous concentrations. The explicit correction procedures for pixels with $F_i' = 0$ and $F_i' = 1$ are described in the second and third step, respectively.

Second, for pixels outside the new MYI domain ($F_i' = 0$), the correction starts with the examination of the distance from the pixel to the boundary. We calculate the distances from this pixel to all the pixels within the estimated domain ($F_i' = 1$). If the minimum distance is more than 4.45 km (one pixel), presence of MYI is not allowed and the MYI concentration on day $i + 1$ is replaced with 0%. If the minimum distance equals to 4.45 km, the MYI concentration is replaced with that of the previous day but only if the difference between the concentration from day $i + 1$ and day i ($\Delta C_{MYI} = C_{MYI,i+1} - C_{MYI,i}$) exceeds a certain threshold (ΔC_M). The value of ΔC_M will be determined in Section 7.3.2. This margin is introduced to account for uncertainties of the ice drift product from NSIDC, which range from $1 - 2$ cm/s (about $1 - 2$ km/day) (Sumata et al., 2014; Sumata et al., 2015).

Third, for pixels that are located within the expected MYI domain ($F_i' = 1$), a correction that accounts for snow wetness and metamorphism is applied to the pixels that have $\Delta C_{MYI} > \Delta C_M$. In Anderson, (1987) and Drobot and Anderson, (2001), the authors used a spectral difference, the horizontal range ($HR = Tb_{19h} - Tb_{37h}$), to

detect snow melt onset on sea ice. When HR is less than -10 K, liquid water is assumed to be present in the snowpack, leading to overestimation of MYI concentration. In the correction procedure, the MYI concentration is replaced with that of the previous day when $HR < -10$ K. In addition, as mentioned before, larger grain size in the snowpack causes decreases of brightness temperature. In previous studies (Anderson, 1997; Drobot and Anderson, 2001), the authors interpreted an abrupt decrease in brightness temperature from one day to the next (ΔTb_{37h}) as being caused by snow metamorphism. In the present correction scheme, if the decrease in Tb_{37h} exceeds another threshold (ΔTb_0), the MYI concentration is replaced with that of the previous day when $\Delta C_{MYI} > \Delta C_M$.

The correction scheme involves two phases. The first phase modifies the anomalous MYI concentration when the pixel is located far enough outside the expected MYI boundary. This is referred to as correction prompted by ice drift. The second phase is applied to pixels inside the expected boundary and referred to as correction prompted by snow wetness/metamorphism. The relative weight of these two components is presented in Section 7.4.1. It should be mentioned that the scheme is applied to the MYI concentration retrieval from ECICE after the application of an earlier correction (Ye, Heygster, and Shokr, 2015) that accounts for sudden drop of MYI concentration (*i.e.*, negative MYI concentration anomaly). These two correction schemes are independent regarding the different MYI anomalies that are accounted for: negative anomaly for the earlier one and positive anomaly for the correction presented here. In the earlier correction (Ye, Heygster, and Shokr, 2015), it has been found that this negative MYI anomaly occurs mainly in September-October, which is triggered by the atmospheric temperature that approaches the melting point of snow and is restored by interpolation of the concentrations before and after the anomaly events.

7.3.2   Threshold adjustment

Two thresholds, ΔC_M and ΔTb_0, are used in the correction procedure. ΔC_M indicates the sudden increases of MYI concentrations beyond which the increase can probably be anomalous, whereas ΔTb_0 is the value above which the sudden decreases in Tb_{37h} is considered to be caused by snow metamorphism.
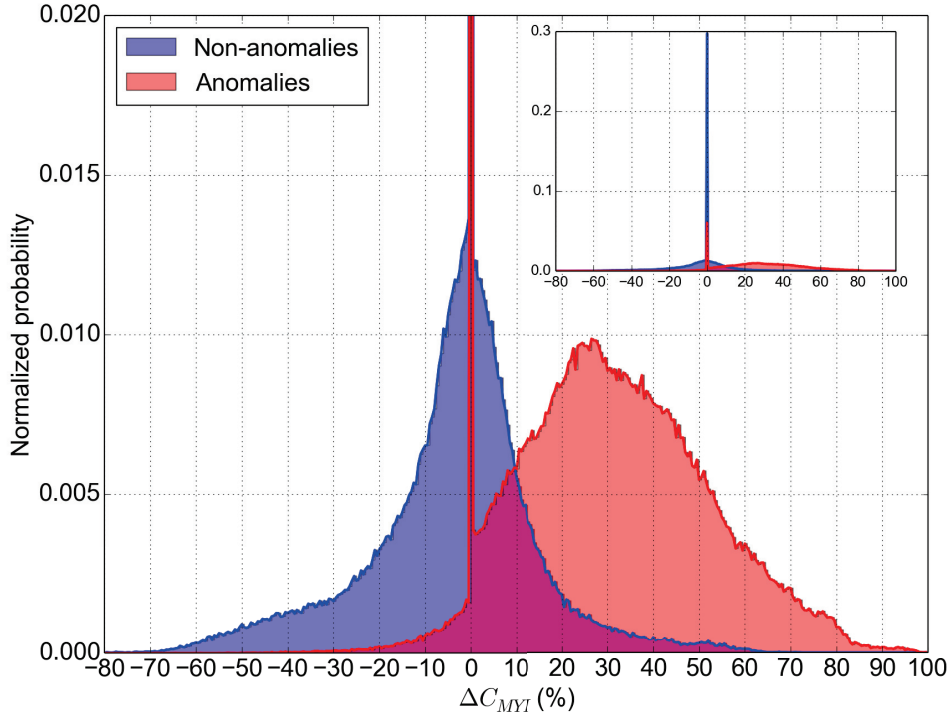

FIGURE 7.4: Probability distribution of ΔC_{MYI} for the non-anomalies and anomalies from 2002 to 2009.

In order to determine the thresholds, we selected samples for anomalies under the condition of unrealistic large increases of MYI concentration along with abrupt decreases of brightness temperatures (about 260 000 data points in total). The selection is based on visual interpretation for maps of MYI concentration and brightness temperature. For comparison, the same pixels were selected from the adjacent days outside the anomalies period. Probability distributions of ΔC_{MYI} and ΔTb_{37h} from these samples from 2002 to 2009 are shown in Figures 7.4 and 7.5, respectively. Red curves represent the distribution of the anomalies, and blue of the non-anomalies.

In Figure 7.4, the value best separating the two clusters of anomalies and non-anomalies is approximately 10 percent (ΔC_{MYI}). In the second step of the correction procedure, ΔC_M is used to account for uncertainties of the MYI concentration retrieval and the ice drift product. Uncertainty of the MYI retrieval from ECICE can reach $5 - 10$ percent, which asserts that ΔC_M should be larger than 10 percent. Among the non-anomalies, 11.9% of the samples have ΔC_{MYI} over 10 percent, while only 5.0% of them have ΔC_{MYI} more than 20 percent. We consider 5% of the non-anomaly values to be falsely corrected (false positives) by the scheme to be acceptable. Therefore, 20 percent is selected as the threshold ΔC_M.
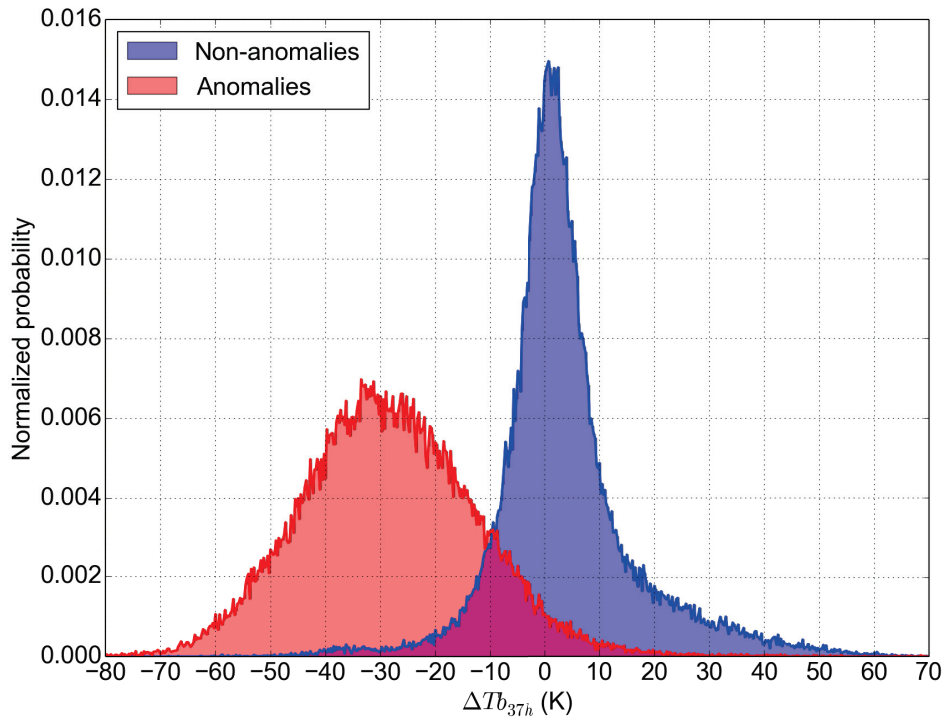

FIGURE 7.5: Probability distribution of daily changes of brightness temperature at vertical polarized 37 GHz (ΔTb_{37h}) for the non-anomalies and anomalies from 2002 to 2009.

The same anomalies and non-anomalies samples are analyzed in Figure 7.5 to determine the threshold ΔTb_0. It is found that -10 K is the value that best distinguishes the anomalies from non-anomalies. Among the non-anomalies, 7.42% of the samples have decreases of Tb_{37h} more than 10 K from one day to the next, whereas only 2.17%

of them have ΔTb_{37h} below -20 K. Again, in order to constrain the amount of non-anomalies to be misidentified as anomalies and over-corrected by the correction (false correction), -20 K is selected as the threshold ΔTb_0.

7.4 Results and discussions

7.4.1 General observations

TABLE 7.1: Relative weight (%) of the two components involved in the correction scheme.

Correction phase	Oct	Nov	Dec	Jan	Feb	Mar	Apr	May
Ice drift	98.64	99.52	99.69	99.73	99.80	99.85	99.78	99.74
Snow wetness/metamorphism	1.36	0.48	0.31	0.27	0.20	0.15	0.22	0.26

As described in Section 7.3, the majority of the anomalous MYI pixels are found to be located far from the main MYI pack. The correction of these pixels is performed using the ice drift data. On the other hand, anomalous pixels within the ice pack are corrected based on the snow wetness/metamorphism radiometric conditions. The percentage of each correction phase is given in Table 7.1, averaged for each month over the seven studied years. It is apparent that most of the affected (anomalous) pixels are located far from the expected MYI boundary and can be corrected with the ice drift data. However, it should be noted that the ice drift correction is applied before the snow wetness/metamorphism correction, thus higher percentage values can be expected.

Examples of the anomalies and the results after correction are presented in Figure 7.6. The top and bottom panels show the estimated MYI concentration before and after correction, respectively. For the days shown in the figure, the MYI concentration maps after applying the temperature-based correction (Ye, Heygster, and Shokr, 2015) are almost identical to those generated from ECICE. This means that the radiometric anomalies that cause erroneous identification of MYI as FYI as discussed in Ye, Heygster, and Shokr, (2015) are rarely encountered in the shown dates. The figure shows
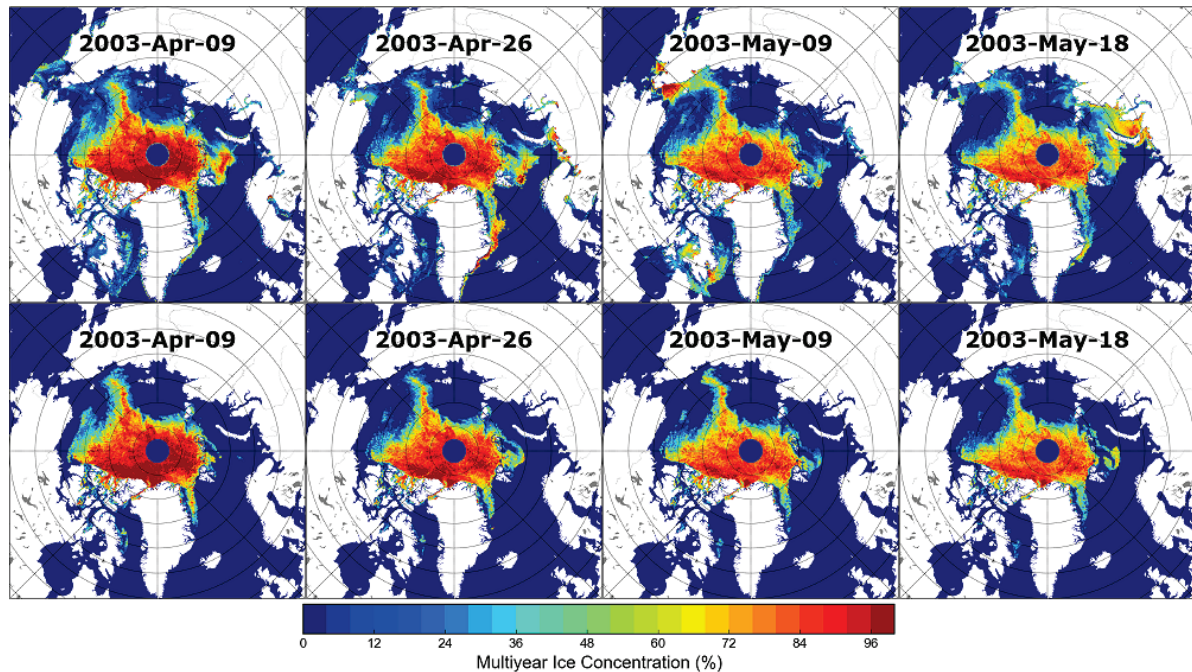
FIGURE 7.6: Multiyear ice concentrations from the ECICE algorithm (top)
and those after the correction on selected days in April–May 2003.

anomalous estimates of MYI (large concentration) in areas that should contain FYI only (based on observations from successive daily MYI concentration maps). The increase occurs usually suddenly between one day and the next (as demonstrated in Figure 7.1) and is attributed to the reasons explained in Section 7.2. In the first example of 9 April a pocket of high MYI concentration is shown between Novaya Zemlya and Svalbard islands. Same anomalies appear in the map of 26 April in addition to other anomalies along the southern coast of Greenland and the Asian coast (east of Scandinavia). The map of 9 May shows the anomalous MYI concentrations in the Chukchi Sea and around the southern area of the Baffin Island, while similar anomalies are apparent in the map of 18 May in the Barents Sea and Bering Strait. Many of such anomalies remain for several days and some continue for the rest of the season. Most of them are removed by the correction scheme presented here as shown in the bottom panel.

The correction preserves some MYI along the ice drift routs, from the central Arctic (where the core volume of MYI exists) to southern latitudes. One such route is Transpolar Drift Stream (TDS), which moves ice from the Siberian coast across the Arctic basin to drift along the east coast of Greenland. Other routes through the Canadian

Arctic Archipelago are also revealed in Figure 7.6. MYI remains also after correction in the Nares Strait between Greenland and Ellesmere Island (a well-known area usually blocked by MYI, leading to formation of the North Water Polynya (Mundy and Barber, 2001; Barber and Massom, 2007). Qualitatively speaking, these observations substantiate the reliability of the correction scheme. The correction scheme introduces a few scattered adjustments of MYI concentration in the central Arctic to account for the radiometric effects of snow metamorphism as explained before. These, however, are few and not readily visible when comparing the uncorrected against the corrected maps. In general, the correction is most pronounced in peripheral seas of the Arctic Basin. It is worth mentioning that the spatial distribution pattern of MYI concentration is preserved on all the dates in Figure 7.6, and the concentration decreases gradually towards the edge of the ice cover.

7.4.2   Inter-comparison with SAR images

This section presents qualitative comparisons of the MYI concentrations before and after corrections against information from the visual analysis of Radarsat-1 SAR images. Four case studies are presented.

Case study (1): ice around Svalbard

Data of 2 April 2003 are shown in Figure 7.7. On this day, the winds were blowing from the north and northeast to the south of Svalbard (the archipelago in the middle of Radarsat-1 frame overlaid on the MYI concentration map in Figure 7.7a) through the Barents Sea (about $5 - 10$ cm/s), and the air temperatures were below $-7°C$. Five areas are marked in the accompanying Radarsat-1 image. Area A contains MYI with its visible floe structure and relatively high backscatter. Areas B and E feature ice surface with relatively high backscatter and smooth texture, which appears to be FYI. Given the southward winds and the low temperatures, these three areas are most likely made up of ice that is advected from the Central Arctic. The MYI concentration maps after
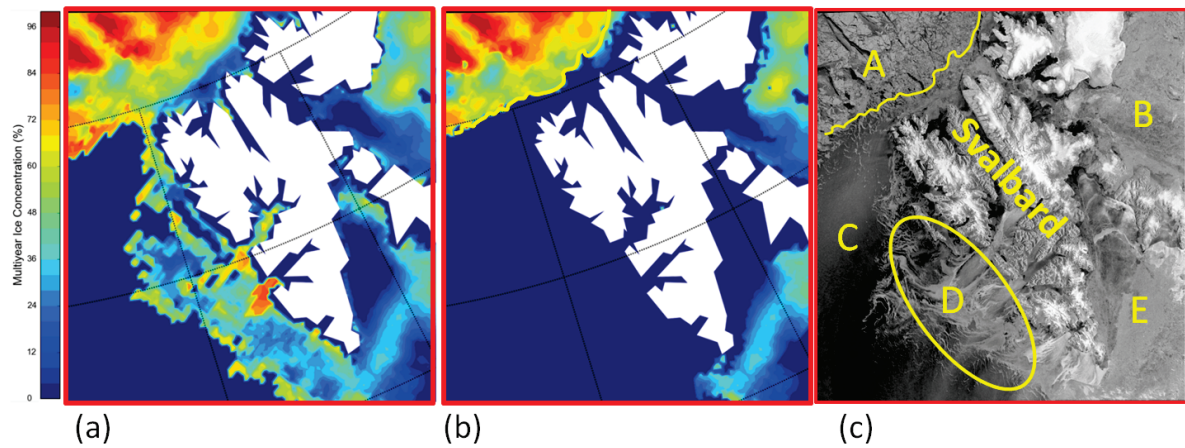
FIGURE 7.7: **(a)** MYI concentration map from ECICE for April 2, 2003 before correction; **(b)** the MYI concentration map after correction; **(c)** the Radarsat-1 image.

correction show values of $20\%-90\%$ in area A and of $10\%-60\%$ in areas B and E. These concentrations remain almost unchanged after correction (comparing Figure 7.7a,b in the figure). Area C appears to have open water, and it remains unaffected by the correction. The remarkable change resulted from application of the correction is visible in area D. Here, the Radarsat-1 image reveals high backscatter with streaks of low values, a typical signature of young ice streaks, which was probably generated locally due to low temperature and wind in this area. The passive microwave signature of young ice can be as low as that of MYI. Therefore, both passive and active microwave observations favored identification of MYI in this area (wrongly). This is removed after correction (Figure 7.7b) based on the fact that MYI in this area is found at far enough distance from the main pack ice.

Case study (2): ice in the Chukchi Sea

MYI concentration maps before and after corrections, along with a corresponding Radarsat-1 image of the Chukchi Sea are shown in Figure 7.8. Data are generated from observations of 6 May, 2003. The high MYI concentrations in the Chukchi Sea (Figure 7.8a) appeared suddenly on 29 April and continued with varying concentration levels until they abated on 17 May. The sudden appearance raises doubt about the authenticity, especially as the area is located far from the main MYI pack in the central Arctic. On

May 6, the temperatures were near $0°C$ and the winds were generally blowing from the southeast with low wind speeds (< 5 cm/s). The Radarsat-1 scene (Figure 7.8c) does not show any MYI with its typical attributes of high backscatter, texture and ice floe structure. Except for what appears to be a quasi-steady water surface with its dark backscatter signature (area A), the rest of the scene emerges as being of consolidated FYI sheet yet with different backscatters. Some linear pressure ridges appear against a background of darker signature in area B. The relatively high backscatter that covers the main scene (area C) can be linked to the wet snow as explained in Section 7.2. This area coincides with the high (and wrong) estimate of MYI concentrations from ECICE, an understandable consequence of the anomalous backscatter. Given the relative high temperatures and the minimum sea ice extent of the previous summer being distant from the Chukchi Sea, the only explanation for the possible appearance of MYI in this region is ice advection from the central Arctic. Yet, the sudden appearance of such high MYI concentration (as mentioned above) refutes this explanation. The correction scheme retained the zero MYI concentration in the region on account of its remoteness from the main MYI pack in the central Arctic.
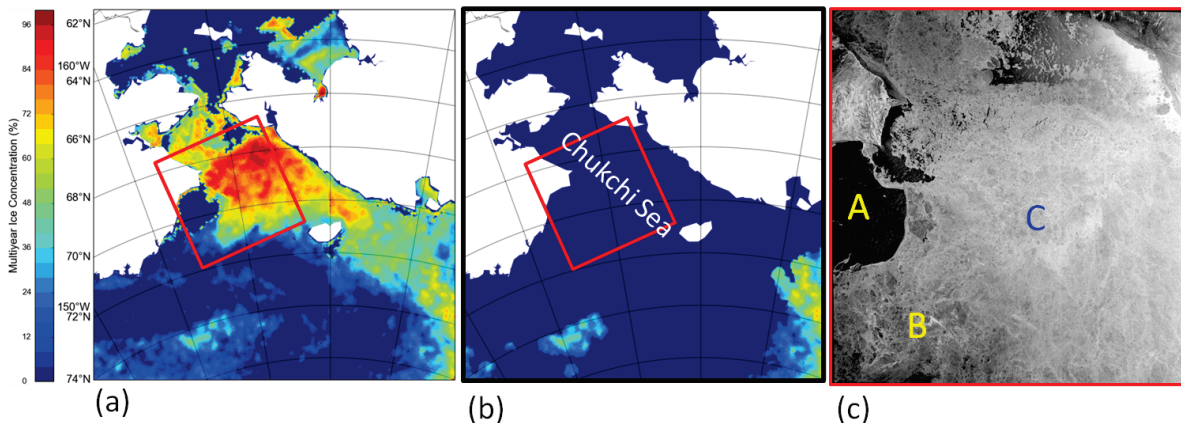

FIGURE 7.8: **(a)** MYI concentration map from ECICE for May 6, 2003 before correction, with the frame of Radarsat-1 image overlaid; **(b)** the same frame with the MYI concentration map after correction; **(c)** the Radarsat-1 image. The red box indicates frame of the Radarsat-1 image.

Case study (3) and (4): ice in the Greenland Sea

These two cases are most crucial because they present results from a highly dynamic ice regime, namely the Greenland Sea along the east coast of Greenland. This is a major route of sea ice drift from the Laptev Sea and East Siberian Sea southward, driven by the Transpolar Drift Stream (TDS) Hilmer, Harder, and Lemke, (1998) and Rigor, Wallace, and Colony, (2002). Since the speed of ice motion is employed in the correction scheme, the results should clearly be sensitive to its accuracy. Assessment of this accuracy in the Arctic region can be found in Sumata et al., (2015). The study presented uncertainties of ice drift for different ice concentrations and drift vectors. The latter were derived from two algorithms: KIMURA Kimura et al., (2013) and the National Snow and Ice Data Center (NSDIC). Uncertainty of monthly mean ice drift during May-July 2005 is found to be around 2 cm/s in the central Arctic, where the ice drift vector is $2 - 6$ cm/s and ice concentration is above 90%. No assessment is provided for the ice drift route along the east coast of Greenland but uncertainties are expected to be larger due to the reduced ice concentration and therefore the higher ice drift. The present algorithm adds one grid cell of 4.45 km to the ice drift advection mask in order to account for ice drift uncertainties (see Section 7.3.1). This corresponds to an uncertainty of about 5 cm/s for the ice drift product. However, assessment of the correction scheme in this area remains crucial because of the possibility of a higher uncertainty of the ice motion.

MYI concentration maps and the Radarsat-1 image of the Greenland Sea on 14 May 2003 are shown in Figure 7.9. On this day, air temperatures were below $-5°C$ within the region. The strong ice drift in the East Greenland Current that originates from the central Arctic was coming from the North. Area A in the Radarsat-1 scene encloses the distribution of MYI concentration as appears in the corrected map (Figure 7.9b). MYI floes are visible with their weathered contours and relatively high backscatter in this area. The correction reduces the MYI area, which is verified in the Radarsat-1 image. Area B feature ice surface with lower backscatter and smoother texture compared to
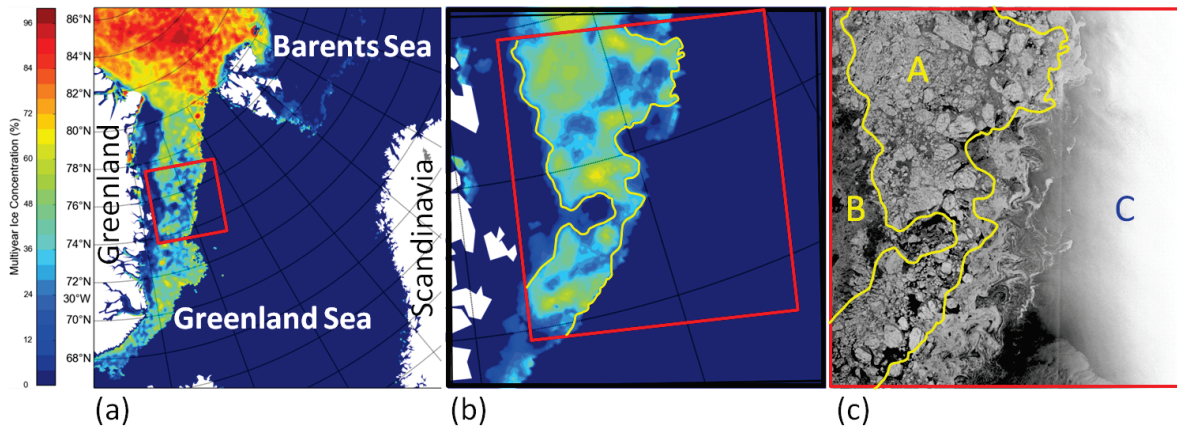
FIGURE 7.9: **(a)** MYI concentration map from ECICE for May 14, 2003 before correction, with the frame of Radarsat-1 image overlaid; **(b)** MYI concentration map after correction, with the same frame of the Radarsat-1 image; **(c)** the Radarsat-1 image. The red box indicates frame of the Radarsat-1 image.

area A, which appears to be FYI. Area C in the Radarsat-1 image features OW with remarkably high backscatter in near range of the satellite view (the right edge of the image). These near-zero MYI concentrations remain unchanged in areas B and C after correction.

A less promising case study is presented in Figure 7.10 (data of 20 May 2003). Here, the correction reduces much MYI concentration compared to the original ECICE output. The MYI distribution as enclosed in Figure 7.10b is confirmed in area B in the Radarsat-1 image with nearly the same average concentration (around 40%). However, some MYI floes are observed in area D, which are removed by the correction scheme. Areas A and C include FYI with relatively smooth texture, where the MYI concentration after correction can be well verified with the Radarsat-1 image in Figure 7.10c.

To conclude this section, it is worth noting that errors in the sea ice drift dataset can be the cause for some of the false removal of MYI (e.g., the case on 20 May 2003). Estimation of the ice drift from passive microwave observations is challenging in the East Greenland Current (EGC) due to the low resolution of the data. The grid resolution of the ice drift dataset is 25 km. Due to high drift speeds in the EGC and high amount of broken up ice without structure, it is, however, more challenging to identify ice patterns from successive images here, which is used for the ice drift retrieval.

The resulting gaps are interpolated in the ice drift dataset and therefore have higher uncertainties. This is happening more frequently in the Greenland Sea than in other areas of the Arctic Basin with lower ice drift speeds. For all the other three examples (Figures 7.7–7.9), the correction scheme provides a clear improvement of the accuracy of MYI concentration estimates.
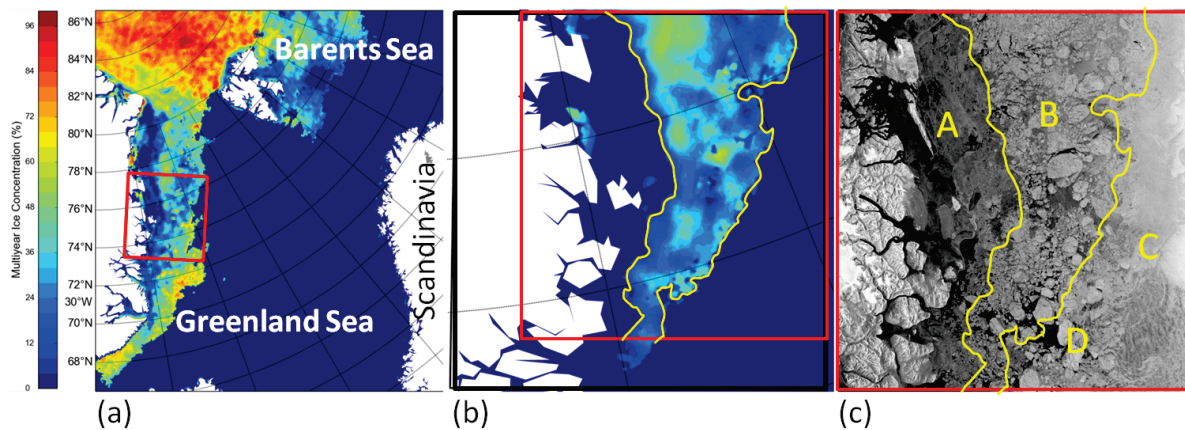

FIGURE 7.10: **(a)** MYI concentration map from ECICE for May 20, 2003 before correction, with the frame of Radarsat-1 image overlaid; **(b)** MYI concentration map after correction, with the same frame of the Radarsat-1 image; **(c)** the Radarsat-1 image. The red box indicates frame of the Radarsat-1 image.

7.4.3   Inter-annual variability over the Entire Arctic

The inter-annual variability of MYI within the Arctic region is presented here as a piece of evidence to support the validation of the correction algorithm. Physically speaking, the presence of MYI in the Arctic is governed by two processes, the aging of FYI to second-year ice and the ice export to southern regions through a few known routes. The first process dominates during September-November and the second continues throughout the year. Therefore, it is expected that MYI area in winter increases in the first two or three months, followed by continuous decreases. This criterion can be used to evaluate MYI area product from different methods.

Figure 7.11 shows the MYI area over the entire (over latitude $60°$N) Arctic before and after correction in winter months (October–May) for the period 2002–2009. As described in Section 7.2, the correction suggested in this study leads to a reduction of

MYI, which is obvious in the figure. On average, the reduction is about 5.2×10^5 km^2 (14.3%) but it exceeds this value in April–May as the warmer weather prompts the conditions of the anomalous snow radiometric signature (see Section 7.2). The data before correction reveals an increase in the MYI area during October-March before it decreases in April–May. This is unrealistic because the transformation of FYI to MYI is limited to October–November. The correction replaces this trend with a nearly constant value in October–January (about 3.75×10^6 km^2 in 2003–2004) or a drop in the area starting immediately in October. The latter is a manifestation of the dominant effect of ice export. It should be noted that the correction produces a larger drop in MYI area between October and May. It also results in less fluctuations (*i.e.*, better monotonic decrease) of the MYI area, which is physically more conceivable and a sign of success as explained above. The standard deviations of the estimated MYI area after correction are smaller than the corresponding values before correction in all the winter months except for May. Besides, the correction produces much higher standard deviation in April–May (1.7×10^5 km^2) than the rest of the season (0.77×10^5 km^2), which can be linked to the higher mobility of the ice cover during the spring months. The results of the MYI retrieval for May also have to be treated with more caution, as melting conditions start in parts of the Arctic which hampers reliable MYI retrieval. Potentially, this can lead to an exaggerated drop in MYI area in May.

Comiso, (2012) studied trends of the Arctic perennial ice during the winters of 1979–2011 using passive microwave observations. The study detected a rapid rate of decline of MYI area (-17.2% per decade). Part of the results is included in Figure 7.11 to compare with the results from this study. These two datasets confirm the inter-annual decay of MYI area at nearly the same rate. It should be noted that the results from Comiso, (2012) are not corrected for anomalous Tb. However they are closer to the corrected results than the uncorrected ones from the present study. The underestimation of Comiso, (2012) except for the winter of 2008-2009 should be attributed to the following two reasons: exclusion of the MYI with concentrations below 30% in Comiso, (2012), and the differences between the two algorithms. The retrieval in Comiso, (2012)

is based on solving the linear equations that decompose each observation into components from different surface types, weighted by the concentration of the surface within a resolution cell. A set of monthly varying tie points is used to account for the intra-winter variation of the MYI signature. This is conceptually different than the ECICE method as explained in Chapter 4.
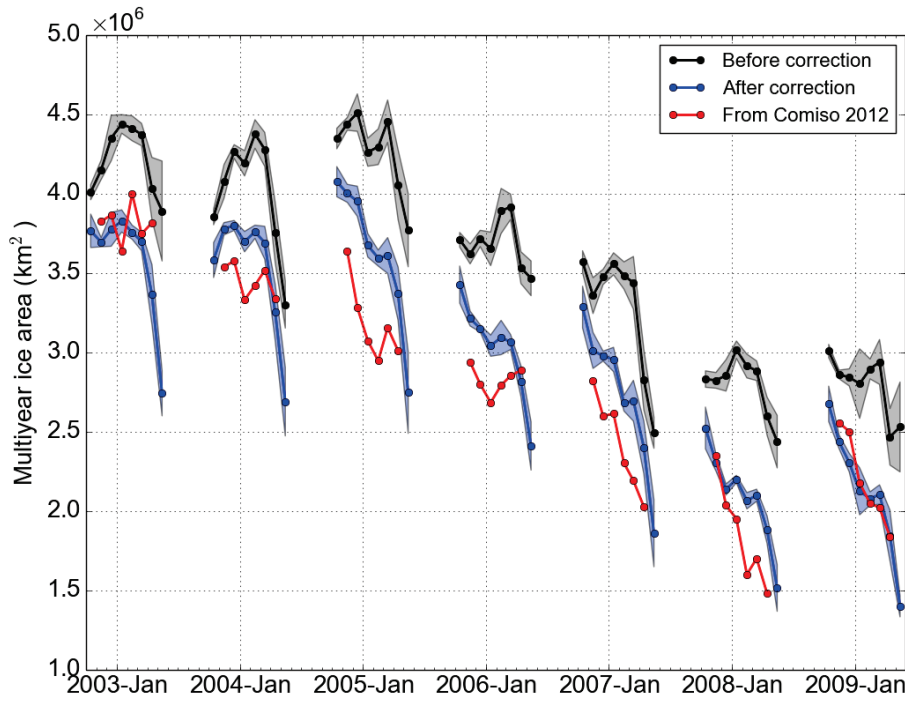

FIGURE 7.11: Monthly averaged Arctic multiyear ice area before and after correction in winters (October–May) from 2002 to 2009. The red line represents the monthly averaged multiyear ice area adapted from Comiso, (2012) (November–April). The gray and light blue areas indicate the standard deviation of the multiyear ice area of each month.

MYI drifts away from the pack ice in the Arctic to lower latitudes through a few routes but mainly through the Fram Strait located between the Greenland and Svalbard. During winter, the MYI area can only decrease due to ice export and ice deformation, *i.e.*, rafting/ridging. Therefore, it can be expected that on first-order the MYI area variability can be associated with sea ice export through the Fram Strait.

Sea ice export from the Fram Strait is compared to the variability of the MYI decrease in the Arctic Basin during winter. The area export is calculated by multiplying sea ice concentration and sea ice drift along a transect at about 79°N and 20°W–5°E

similar to Spreen et al., (2009), for area but not volume fluxes. The sea ice concentrations are calculated from SSM/I (the Special Sensor Microwave Imager) data using the ASI algorithm (Spreen, Kaleschke, and Heygster, 2008; Kaleschke et al., 2001). For sea ice drift, the 3-daily QuikSCAT-SSM/I dataset from IFREMER/Cersat, Brest, France (Girard-Ardhuin and Ezraty, 2012) is used. Both datasets were brought onto the same polar stereographic grid, and gaps in the ice drift dataset were interpolated before the sea ice area flux is calculated. The monthly Fram Strait sea ice export was calculated from the daily area fluxes.
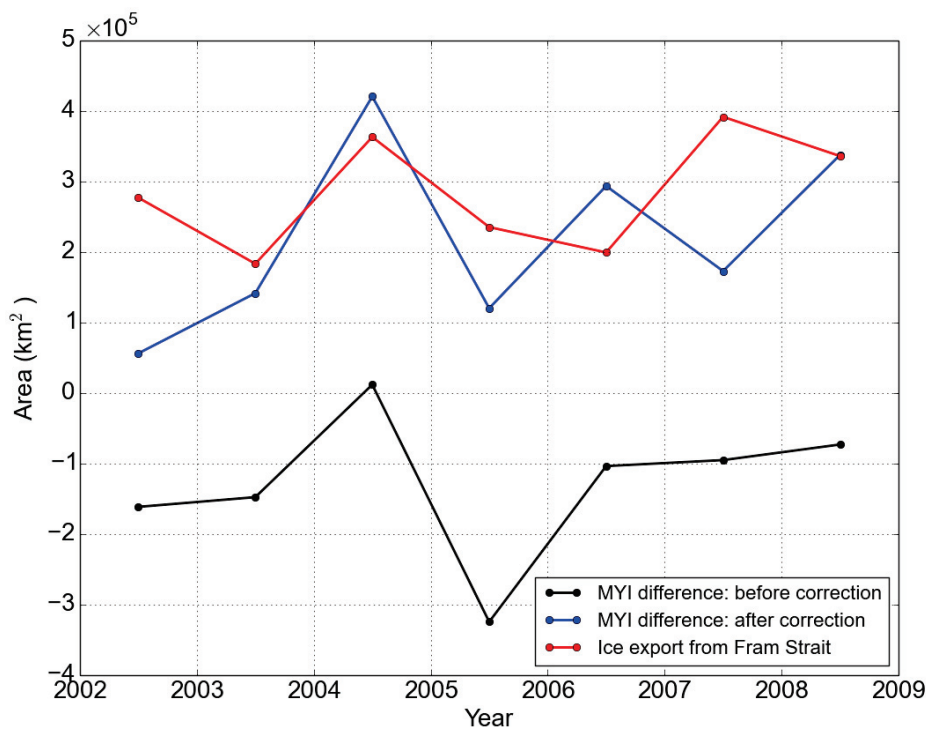

FIGURE 7.12: The MYI area difference between November and March (the area in November minus that in March) and the ice export through the Fram Strait from 2002–2003 to 2008–2009. The black and blue lines depict the decreases of the MYI area before and after correction, respectively. The calculation of MYI area excludes the Greenland Sea south of the Fram Strait (latitude: $60°N–80°N$, longitude: $45°W–0°W$)

Figure 7.12 shows the difference in MYI area between November and March (the area in November minus that in March) for the winters from 2002–2003 to 2008–2009, along with the ice area export through the Fram Strait for the same period. The MYI area difference is obtained for the Arctic Basin only by excluding the area between

$45°$W and $0°$W and below $80°$N. As investigated in Ye, Heygster, and Shokr, (2015), warm air spells leading to misidentification of MYI as FYI occur mostly in September and October. In order to exclude the impact of the temperature correction suggested in Ye, Heygster, and Shokr, (2015), the data of these two months are not included in the comparison. Data of April and May were not included also because of their large variations as discussed above.
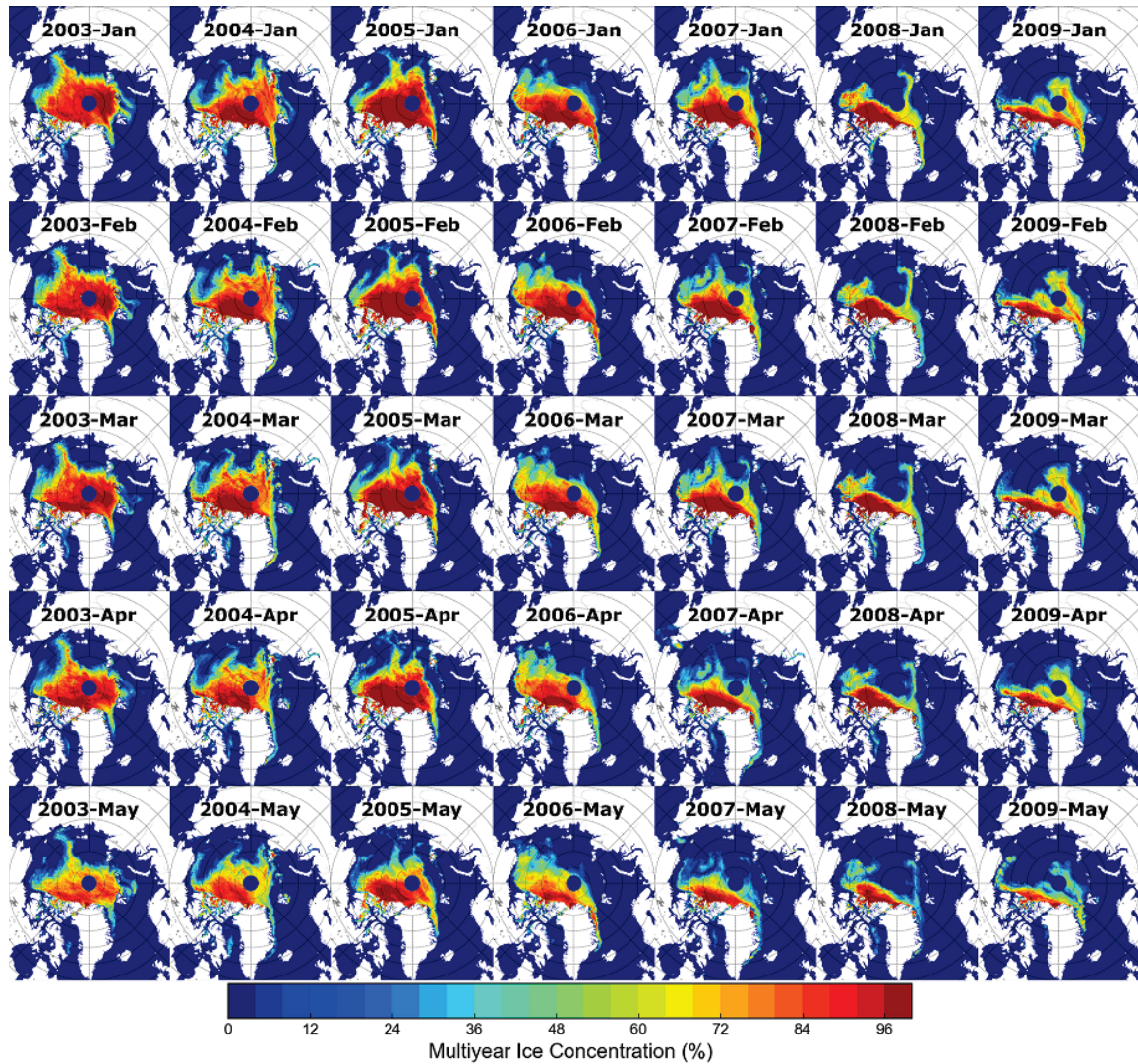

FIGURE 7.13: Monthly average concentration of multiyear ice after correction for January-May of the years 2003–2009.

In the seven winters, the MYI area before correction exhibits increases from November to March except for the winter of 2004–2005. This is physically not realistic because large areas of MYI can be formed during winter and it negates the ice export through

the Fram Strait. The correction scheme reverses this wrong trend and produces a decrease of the MYI area which fairly well agrees with the outflow through the Fram Strait, which makes up about 90% of the Arctic sea ice export. It is worth noting that the ice area flux is calculated regardless of ice type but the ice drifting from the central Arctic through the Fram Strait includes a high percentage of MYI. MYI export is the major cause for changes in MYI area during winter time. The only other possible mechanism is sea ice ridging, which also can reduce the MYI area but to a much smaller degree. Therefore some correspondence but no perfect match should be expected between the winter MYI area decrease and the winter Fram Strait ice area export. The two time series (blue and red curves in Figure 7.12) show good correspondence for several years. For example the above average decrease of MYI area in winter 2004–2005 is also visible in an enhanced ice export. The MYI decrease in winter 2006–2007 is the third highest of the seven-year time series but not very pronounced. The ice export in winter 2006–2007 is even the second lowest of the time series. Both hinting to the loss of MYI in the previous winter was not the major driver for the sea ice minimum in 2007. We consider the much better agreement of the winter MYI area decrease with the Arctic ice export after the correction as another evidence for the improvement, which can be attributed to the present correction scheme.

Figure 7.13 shows the monthly average MYI concentration maps from January to May for the years from 2003 to 2009. Within each year, the MYI coverage decreased as the freezing season progressed after January. This is mainly due to ice advection and a much less degree because of ridging. For the MYI area decrease from one year to the next, melt across the Beaufort Sea can also be an explanation. Kwok and Cunningham, (2010) studied the contribution of melt in the Beaufort Sea to the decline of sea ice area. It is found that the net melt area in the Beaufort Sea between 2005 and 2008 accounts for nearly 32% of the net loss of Arctic MYI coverage over the same period. Figure 7.13 shows two notable decreases of MYI area in January 2006 and January 2008 compared to the same month in the previous years. These should be linked to the findings of the first and second minima of the Arctic ice extent, observed in

September 2005 (5.56×10^6 km^2; a 0.94% drop relative to 1981–2010 average) and 2007 (4.29×10^6 km^2) (National Snow and Ice Data Center, website `https://nsidc.org/ cryosphere/sotc/sea_ice.html`). This figure confirms the trend established in previous studies (e.g., Kwok, (2006)) that MYI continues to be pushed against northern Greenland, Ellesmere Island and Queen Elizabeth Island, where it is either deformed or advected further southwards through passages in the Canadian Arctic Archipelago.

7.4.4   Regional sensitivity to the correction

As mentioned in Section 7.4.1, the correction incorporates two schemes. The first, which is based on records of atmospheric temperature, is used mainly to correct anomalies observed in September-October (Ye, Heygster, and Shokr, 2015). The second, which accounts for snow wetness/metamorphism and employs ice drift data, is the one described in Sections 7.2 and 7.3. Results from the second scheme only are presented in Figure 7.14. The figure shows maps of the difference between the corrected and the uncorrected MYI concentration. Each panel represents the average over the given month using all the available months from October 2002 to May 2009. The regional distribution where the correction scheme is applied can be clearly seen from the figure.

Minor differences are observed in the data of October and to some extent November before the differences become more pronounced in late winter and spring months. The differences are always restricted to the peripheral of the Arctic Basin, where atmospheric temperatures are higher than those in the central Arctic and ice deformation due to waves and storms is more prevalent. These areas usually feature FYI and younger ice that can be misidentified as MYI when snow conditions lead to anomalous radiometric signature. More differences are found along the ice drift routes in the Greenland Sea and the Baffin Bay. Lower latitudes of the Chukchi Sea and Bering Sea (associated with relatively higher winter temperature) reveal also larger differences after January when the region is covered with thick snow over FYI that will

metamorphose under favourable meteorological conditions. The largest differences are observed in May, which marks common dates of pre-melt and melt onset conditions (Markus, Stroeve, and Miller, 2009), hence extensive snow metamorphism. The dark blue color in the map of May indicates where discrimination between FYI as MYI can be problematic using microwave observations. This is noticeable in the Chukchi Sea, Bering Sea, Kara Sea, as well as the Baffin Bay and Hudson Bay. These areas should be carefully considered when evaluating performances of different MYI retrieval algorithms, which do not work during summer months and already can show degrading performance in May. It should be noted that the false estimate of MYI is common in the Barents Sea between Novaya Zemlya and Svalbard during the entire freezing season, though at a noticeably lower level in May when most of the ice has already melted or drifted away.
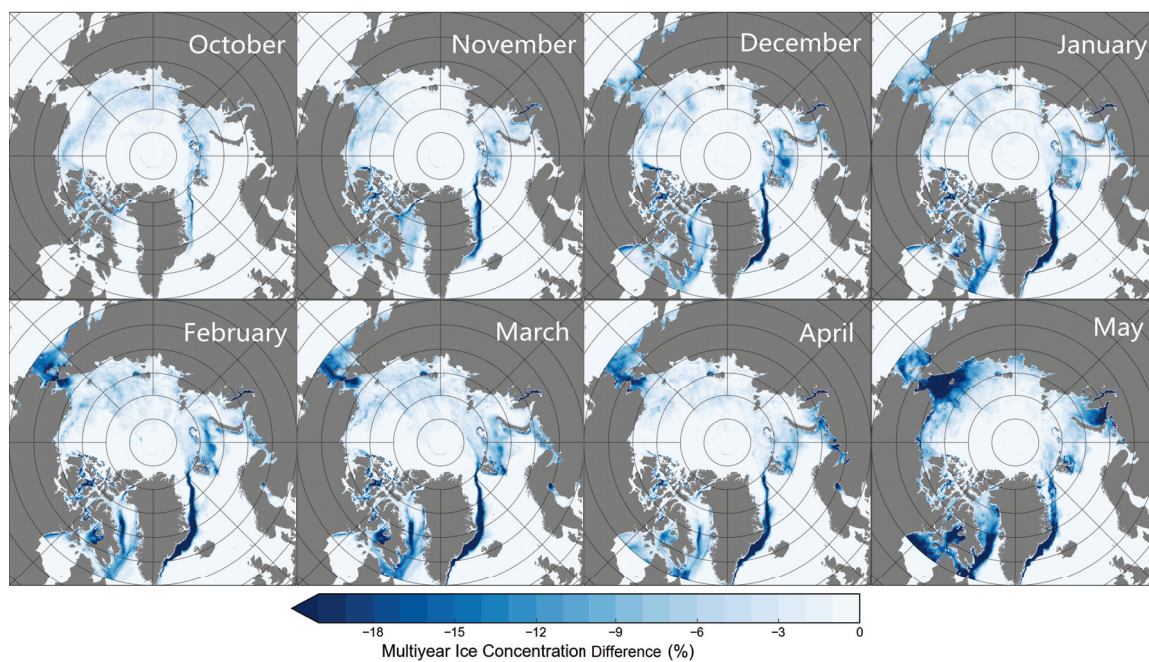

FIGURE 7.14: Corrected minus uncorrected MYI concentration maps resulting from the presented correction scheme. Data for each month are averaged over the winter months available from 2002–2003 to 2008–2009.

7.5 Conclusions

When the atmospheric temperature approaches the melting point, physical properties of snow on FYI change, triggering anomalous brightness temperatures and backscatters, which deviate from the typical values. These values from FYI become very similar to those from MYI. Deformation and roughening of the ice surface can have a similar effect. These radiometric observations lead to misidentification of FYI as MYI, resulting in erroneous high MYI concentration retrievals. A correction utilizing ice drift records, along with thresholds on the derived parameters from the passive microwave observations, is suggested and applied to the MYI concentration retrieval from ECICE. The correction is applied on the retrieval between October and May for the seven years from 2002 to 2009. The retrieval is preprocessed by another correction suggested in Ye, Heygster, and Shokr, (2015) to account for a different radiometric anomaly that leads to misidentification of MYI as FYI.

It is worth mentioning that the corrections presented here and in Ye, Heygster, and Shokr, (2015) take the spatial and temporal continuity of MYI into account, which was not considered in the MYI concentration retrieval algorithms.

The correction presented here, which leads to a reduction of the MYI area, is designed to constrain the MYI concentration changes within a plausible contour on a given day, when ice drift data is used to expand the contour of the previous day. On average, the reduction is about 5.2×10^5 km^2 (14.3%) but it exceeds this value in April–May as warmer weather prompts the conditions of the anomalous snow radiometric signature. In October–March, the MYI area without correction increases, which is physically not realistic. After correction, the MYI area stays fairly constant in October–January or decreases immediately in October. The corrected MYI time series shows a realistic decrease of MYI area during winter, which can be expected as MYI continues to be exported out of the Arctic Basin. The loss in MYI area between November and March is of the same magnitude and shows similar variability as the observed sea ice export through the Fram Strait. The much better agreement of the winter MYI area

decrease with the Arctic ice export after the correction gives evidence of the improvement, which is attributed to the present correction scheme.

Maps of the difference between the corrected and uncorrected MYI concentrations show that the difference is most pronounced in months between January and May, and prominent in the peripheral seas of the Arctic. Areas where the differences are larger and atmospheric temperatures are higher, e.g., the Greenland Sea, the Baffin Bay, the Kara Sea, the Chukchi and Bering Seas, should be carefully considered when evaluating performances of different MYI retrieval algorithm.

The comparison with Radarsat-1 SAR images shows that the correction works well by removing unexpected anomalous high MYI concentrations in the peripheral seas of the Arctic except for one case in the Greenland Sea, where assessment of the correction remains crucial because of the possibility of a higher uncertainty of the ice drift product.

To conclude, the correction works well by constraining the MYI concentrations from increasing suddenly and unrealistically in the peripheral seas of the Arctic. It can be applied as a post-processing to all the microwave-based MYI retrieval algorithms, such as the NASA Team algorithm (Steffen and Schweiger, 1991; Ye and Heygster, 2015), the NORSEX algorithm (Svendsen et al., 1983), the UMass-AES algorithm (Swift, Fedor, and Ramseier, 1985), and the ECICE algorithm (Shokr, Lambe, and Agnew, 2008). As warm air spells frequently occur in late winter and spring months and in the peripheral Arctic Seas, it is crucial to consider this situation when retrieving partial ice concentrations. The derived MYI time series after correction is more consistent and fluctuates less, therefore the correction can be important in climatological research and operational applications.

The fundamentally new aspect of the correction suggested here is the insight that instantaneous observations alone of sea ice may lead to ambiguities in determination of the concentration of sea ice types. Instead, the development in time, here of the ice motion, is also crucial for the retrieval. This approach may be applicable to the retrieval of other sea ice parameters, too, especially to sea ice emissivity. In principle,

for the retrieval, a forward model combined with an inversion procedure would be preferable, as it has been done over open ocean to retrieve surface and atmospheric parameters for many years (Wentz and Meissner, 2000). Similar procedures have also been suggested over sea ice (e.g., (Melsheimer et al., 2009)). However, their results are much less reliable. The reason is that we cannot predict sea ice emissivity at the scale of satellite sensor footprints due to the high horizontal and vertical variability of the sea ice microphysical properties, which are required as input for sea ice emissivity models but are difficult to measure. As long as this flaw persists, the approach forwarded in this paper may be the best possibility to more accurately determine the Arctic MYI concentration, which in turn is required for a more accurate description of the radiative and dynamic processes in the sea ice covered Arctic.

Chapter 8

Conclusions

This chapter summarizes the main findings and work done in Chapters 5 to 7.

In Chapter 5, a modified NASA Team algorithm with dynamic tie points was developed to compensate the impacts of temperature variation of brightness temperature variations. MYI concentration were retrieved with the original and modified NASA Team algorithm using SSM/I data in winters of the years 1989–2012. The method with dynamic tie points yields higher estimates in most years. Besides, both methods show a clear declining trend of the MYI area from 1989 to 2012, which is consistent with the decrease of the annual minimum ice extent. The MYI area in most years decreases during the winter, reflecting the expected loss of MYI by export to lower latitudes. The sensitivity of each tie point on the MYI concentration retrieval was investigated. For the NASA Team algorithm, the MYI retrieval is most sensitive to the tie points of MYI and FYI at 19 GHz vertical polarization. Therefore, these tie points need to be determined more accurately if dynamic tie points are used for MYI concentration retrieval with the NASA Team algorithm.

Chapter 6 introduced a correction scheme to restore the underestimated MYI concentration under warm air conditions. Warm-cold air temperature cycles trigger wet-dry cycles of the snow on MYI surface, leading to anomalous brightness temperature and backscatter from MYI, which are similar to those from FYI. The retrieved MYI concentrations are therefore underestimated and erroneous under such condition. Based on air temperature records and the fact that the warm spell lasts for a few days, the

correction is designed to restore the low MYI concentrations to high values. The correction was applied to the MYI concentration retrieval from the ECICE algorithm from September to December for the years from 2003 to 2008.

MYI concentration after correction is overall higher than that before correction. For September of the six years, the correction introduces over 1.0×10^5 km^2 MYI area, except for 2005. Additionally, the difference between the corrected and uncorrected MYI areas diminishes by the end of each September, reflecting the abatement of warm spells in the Arctic.

Chapter 7 introduced another correction scheme to correct the overestimated MYI concentration. When air temperature approaches the melting point, brightness temperature and backscatter from snow-covered FYI become similar to those from MYI, leading to erroneous high MYI concentration retrievals. Unlike the case in Chapter 6 where the effect of a warm spell on snow-covered MYI lasts for a few days, the effect on FYI lasts for much longer, typically from one to several weeks. A correction based on ice drift is developed to constrain the MYI concentration changes. It uses two thresholds of passive microwave radiometric parameters to account for snow wetness and metamorphism. The correction was applied to the MYI concentration retrieval from the ECICE algorithm for the winters (October to May) from 2002 to 2009.

Qualitative comparison with Radarsat-1 SAR images, quantitative comparison against results from previous studies (Comiso, 2012) and that with the ice export from Fram Strait show that the correction works well by removing the erroneous high MYI concentrations. On average, the correction reduces 5.2×10^5 km^2 (14.3%) of the estimated MYI area except for the April-May time frame, when the reduction is larger as the warmer weather prompts the condition of the anomalous snow radiometric signature. In addition, the difference between the corrected and uncorrected MYI concentration is prominent in the peripheral seas of the Arctic, indicating that the evaluation of MYI retrieval algorithms is crucial in this region.

In summary, three methods were developed to improve and correct MYI concentrations estimates from microwave satellite observations. The first method builds upon

the NASA Team algorithm, where only passive microwave remote sensing (radiometer) data is used for MYI concentration retrieval. The technique of deriving dynamic tie points can also be used in other radiometer-based MYI retrieval algorithms, e.g., the Bootstrap algorithm (Comiso, 2012). However the highly sensitive tie points should be treated with caution. The second and third methods (presented in Chapters 6 and 7) were used to account for radiometric anomalies that trigger the erroneous MYI concentration retrieval from microwave satellite observation. They can be applied as post-processings to all the microwave-based MYI retrieval algorithms, such as the NASA Team algorithm (Steffen and Schweiger, 1991; Ye and Heygster, 2015), the NORSEX algorithm (Svendsen et al., 1983), the UMass-AES algorithm (Swift, Fedor, and Ramseier, 1985), and the ECICE algorithm (Shokr, Lambe, and Agnew, 2008). It is worth mentioning that both corrections take the spatial and temporal continuity of MYI into account, which gives a new insight that instantaneous observations alone of sea ice may lead to ambiguities in determination of partial ice concentrations. This approach may be applicable to the retrieval of other sea ice parameters as well.

Acknowledgements

There are many people from whom I learned and benefited in these years, without their precious support this thesis would not have been possible. Thus I grateful acknowledge,

Prof. Dr. Thomas Jung for his willingness to review this thesis.

Prof. Dr. Justus Notholt for providing me an opportunity to conduct this thesis, for reviewing the thesis and for his support during my Ph.D. research.

Dr. Georg Heygster for giving me the initial idea for the Ph.D. project, for advising me on relevant literature and conferences, for constructive suggestions, for reviewing the manuscripts and for starting collaboration with Dr. Mohammed Shokr.

Dr. Mohammed Shokr for the fruitful collaboration and the continuous support, for the the useful discussions and inspiring advice, for reviewing the manuscripts and this thesis, and for hosting me during the research stay in Environment Canada.

Dr. Gunnar Spreen for the helpful discussions, for providing me an exceptional prolongation of funding, for reviewing the manuscripts and this thesis, and for supporting me to apply for post-doc positions.

Dr. Christian Melsheimer for many discussions and being my Ph.D. committee member, for his positive attitude and broad knowledge, and for helping me with administrative and scientific tasks.

Dr. Martin Losch for always participating in my Ph.D. committee meeting, for which he needs to travel, and for the valuable advice he gives.

List of Abbreviations

MYI	Multiyear ice
FYI	First-year ice
YI	Young ice
OW	Open Water
CAA	Candian Arctic Archipelago
ECICE	Environment Canada Ice Concentration Extractor
WMO	World Meteorological Organization
SYI	Second-year ice
SSM/I	Special Sensor Microwave Imager
SSM/I	Special Sensor Microwave Imager/Sounder
AMSR-E	Advanced Microwave Scanning Radiometer - Earth Observation System
DMSP	Defense Meteorological Satellite Programme
NSIDC	National Snow and Ice Data Center
MERS	Microwave Earth Remote Sensing
BYU	Brigham Young University
SIR	Scatterometer Imager Reconstruction
ECMWF	European Center for Medium-Range Weather Forecasts
EASE	Equal Area Scalable Earth
AVHRR	Advanced Very High Resolution Radiometer
SMMR	Scanning Multichannel Microwave Radiometer
IABP	International Arctic Buoy Program
NCEP	National Centers for Environmental Prediction
SAR	Synthetic Aperture Radar
PR	Polarization Ratio
GR	Gradient Ratio
PCT	Polarization Corrected Temperature

References

Anderson, M. R. (1987). "The onset of spring melt in first-year ice regions of the Arctic as determined from scanning multichannel microwave radiometer data for 1979 and 1980". In: *Journal of Geophysical Research: Oceans (1978–2012)* 92.C12, pp. 13153–13163.

— (1997). "Determination of a melt-onset date for Arctic sea-ice regions using passive-microwave data". In: *Annals of Glaciology* 25, pp. 382–387.

Asplin, M. G., J. V. Lukovich, and D. G. Barber (2009). "Atmospheric forcing of the Beaufort Sea ice gyre: Surface pressure climatology and sea ice motion". In: *Journal of Geophysical Research: Oceans (1978–2012)* 114.C1.

Barber, D. G. (2005). "Microwave remote sensing, sea ice and Arctic climate". In: *Physics in Canada* 61, pp. 105–111.

Barber, D. G. and R. A. Massom (2007). "The role of sea ice in Arctic and Antarctic polynyas". In: *Elsevier Oceanography Series* 74, pp. 1–54.

Barber, D. G. et al. (2015). "Selected physical, biological and biogeochemical implications of a rapidly changing Arctic Marginal Ice Zone". In: *Progress in Oceanography* 139, pp. 122–150.

Blunden, J. and D. S. Arndt (2012). "State of the climate in 2011". In: *Bulletin of the American Meteorological Society* 93.7, 0_1.

Cavalieri, D. and C. Parkinson (2012). "Arctic sea ice variability and trends, 1979–2010". In: *The Cryosphere* 6.4, pp. 881–889.

Cavalieri, D. et al. (1991). "Aircraft active and passive microwave validation of sea ice concentration from the Defense Meteorological Satellite Program Special Sensor Microwave Imager". In: *Journal of Geophysics Research* 96.C12, pp. 21989–22008.

Cavalieri, D. J., P. Gloersen, and W. J. Campbell (1984). "Determination of sea ice parameters with the Nimbus 7 SMMR". In: *Journal of Geophysical Research: Atmospheres (1984–2012)* 89.D4, pp. 5355–5369.

Comiso, J. (1985). "Remote sensing of sea ice using multispectral microwave satellite data". In: *Advances in Remote Sensing Retrieval Methods. A. Deepak, Hampton, VA*, pp. 349–369.

— (1990). "Arctic multiyear ice classification and summer ice cover using passive microwave satellite data". In: *Journal of Geophysical Research: Oceans* 95.C8, pp. 13411–13422.

Comiso, J., S. Ackley, and A. Gordon (1984). "Antarctic sea ice microwave signatures and their correlation with in situ ice observations". In: *Journal of Geophysical Research: Oceans (1978–2012)* 89.C1, pp. 662–672.

Comiso, J. C. (2002). "A rapidly declining perennial sea ice cover in the Arctic". In: *Geophysical Research Letters* 29.20.

— (2006a). "Abrupt decline in the Arctic winter sea ice cover". In: *Geophysical Research Letters* 33.18.

— (2006b). "Impacts of the variability of second-year ice types on the decline of the Arctic perennial sea-ice cover". In: *Annals of Glaciology* 44.1, pp. 375–382.

— (2012). "Large Decadal Decline of the Arctic Multiyear Ice Cover." In: *Journal of Climate* 25.4, pp. 1176–1193.

Comiso, J. C. et al. (1997). "Passive microwave algorithms for sea ice concentration: A comparison of two techniques". In: *Remote Sensing of Environment* 60.3, pp. 357–384.

Comiso, J. C. et al. (2008). "Accelerated decline in the Arctic sea ice cover". In: *Geophysical Research Letters* 35.1.

Dee, D. et al. (2011). "The ERA-Interim reanalysis: Configuration and performance of the data assimilation system". In: *Quarterly Journal of the Royal Meteorological Society* 137.656, pp. 553–597.

Doronin, Y. P. and D. Kheisin (1977). *Sea Ice*. Amerind Publishing, New Dehli.

Drobot, S. D. and M. R. Anderson (2001). "An improved method for determining snowmelt onset dates over Arctic sea ice using scanning multichannel microwave radiometer and Special Sensor Microwave/Imager data". In: *Journal of Geophysical Research: Atmospheres (1984–2012)* 106.D20, pp. 24033–24049.

Du, J., J. Shi, and H. Rott (2010). "Comparison between a multi-scattering and multi-layer snow scattering model and its parameterized snow backscattering model". In: *Remote Sensing of Environment* 114.5, pp. 1089–1098.

Early, D. S. and D. G. Long (2001). "Image reconstruction and enhanced resolution imaging from irregular samples". In: *Geoscience and Remote Sensing, IEEE Transactions on* 39.2, pp. 291–302.

Fowler, C, W Emery, and M Tschudi (2013). *Polar Pathfinder Daily 25 km EASE-grid Sea Ice Motion Vectors, Version 2*. NASA National Snow and Ice Data Center Distributed Active Archive Center. Boulder, Colorado USA.

Fuhrhop, R. et al. (1998). "A combined radiative transfer model for sea ice, open ocean, and atmosphere". In: *Radio Science* 33.2, pp. 303–316.

Girard-Ardhuin, F. and R. Ezraty (2012). "Enhanced Arctic sea ice drift estimation merging radiometer and scatterometer data". In: *Geoscience and Remote Sensing, IEEE Transactions on* 50.7, pp. 2639–2648.

Gloersen, P. and D. J. Cavalieri (1986). "Reduction of weather effects in the calculation of sea ice concentration from microwave radiances". In: *Journal of Geophysical Research: Oceans* 91.C3, pp. 3913–3919.

Grenfell, T. (1992). "Surface-based passive microwave studies of multiyear sea ice". In: *Journal of Geophysical Research: Oceans* 97.C3, pp. 3485–3501.

Haas, C. and S. E. Howell (2015). "Ice thickness in the Northwest Passage". In: *Geophysical Research Letters* 42.18, pp. 7673–7680.

Hallikainen, M. and D. P. Winebrenner (1992). "The physical basis for sea ice remote sensing". In: *Microwave Remote Sensing of Sea Ice*. Ed. by F. D. Carsey. Wiley Online Library, pp. 29–46.

Heygster, G. et al. (2014). "Response of passive microwave sea ice concentration algorithms to thin ice". In: *Geoscience and Remote Sensing Symposium (IGARSS), 2014 IEEE International*. Quebec City, Canada: IEEE, pp. 3618–3621.

Hilmer, M., M. Harder, and P. Lemke (1998). "Sea ice transport: A highly variable link between Arctic and North Atlantic". In: *Geophysical Research Letters* 25.17, pp. 3359–3362.

Hoffman, R. N. and S. M. Leidner (2005). "An introduction to the near-real-time QuikSCAT data". In: *Weather and Forecasting* 20.4, pp. 476–493.

Howell, S. et al. (2015). "Multiyear ice replenishment in the Canadian Arctic Archipelago: 1997–2013". In: *Journal of Geophysical Research*.

Howell, S. E. et al. (2008). "Changing sea ice melt parameters in the Canadian Arctic Archipelago: Implications for the future presence of multiyear ice". In: *Journal of Geophysical Research: Oceans (1978–2012)* 113.C9.

Howell, S. E. et al. (2013). "Recent changes in the exchange of sea ice between the Arctic Ocean and the Canadian Arctic Archipelago". In: *Journal of Geophysical Research: Oceans* 118.7, pp. 3595–3607.

Isaaks, E. H. and R. M. Srivastava (1989). *An introduction to applied geostatistics*. Oxford University Press.

Ivanova, N. et al. (2014). "Retrieval of Arctic sea ice parameters by satellite passive microwave sensors: A comparison of eleven sea ice concentration algorithms". In: *Geoscience and Remote Sensing, IEEE Transactions on* 52.11, pp. 7233–7246.

Johannessen, O. M., E. V. Shalina, and M. W. Miles (1999). "Satellite evidence for an Arctic sea ice cover in transformation". In: *Science* 286.5446, pp. 1937–1939.

Kaleschke, L et al. (2001). "SSM/I sea ice remote sensing for mesoscale ocean-atmosphere interaction analysis". In: *Canadian Journal of Remote Sensing* 27.5, pp. 526–537.

Kim, Y.-S., R. G. Onstott, and R. K. Moore (1984). "Effect of a snow cover on microwave backscatter from sea ice". In: *Oceanic Engineering, IEEE Journal of* 9.5, pp. 383–388.

Kim, Y. et al. (1985). "Towards identification of optimum radar parameters for sea-ice monitoring". In: *Journal of Glaciology* 31.109, pp. 214–219.

Kimura, N. et al. (2013). "Influence of winter sea-ice motion on summer ice cover in the Arctic". In: *Polar Research* 32.

Koskinen, J., J. Pulliainen, and M. Hallikainen (2000). "Effect of snow wetness to C-band backscatter-a modeling approach". In: *Geoscience Remote Sensing Symposium, 2000. Proceedings. IGARSS 2000. IEEE 2000 International*. Vol. 4. IEEE. Honolulu, HI, USA, pp. 1754–1756.

Kwok, R (2004). "Annual cycles of multiyear sea ice coverage of the Arctic Ocean: 1999–2003". In: *Journal of Geophysical Research: Oceans (1978–2012)* 109.C11.

— (2009). "Outflow of Arctic Ocean sea ice into the Greenland and Barents Seas: 1979-2007". In: *Journal of Climate* 22.9, pp. 2438–2457.

Kwok, R and G. Cunningham (2010). "Contribution of melt in the Beaufort Sea to the decline in Arctic multiyear sea ice coverage: 1993–2009". In: *Geophysical Research Letters* 37.20.

Kwok, R, G. Cunningham, and S. Pang (2004). "Fram Strait sea ice outflow". In: *Journal of Geophysical Research: Oceans* 109.C1.

Kwok, R, G Spreen, and S Pang (2013). "Arctic sea ice circulation and drift speed: Decadal trends and ocean currents". In: *Journal of Geophysical Research: Oceans* 118.5, pp. 2408–2425.

Kwok, R et al. (2009). "Thinning and volume loss of the Arctic Ocean sea ice cover: 2003–2008". In: *Journal of Geophysical Research: Oceans (1978–2012)* 114.C7.

Kwok, R. (2006). "Exchange of sea ice between the Arctic Ocean and the Canadian Arctic Archipelago". In: *Geophysical Research Letters* 33.16.

— (2007). "Near zero replenishment of the Arctic multiyear sea ice cover at the end of 2005 summer". In: *Geophysical Research Letters* 34.5.

Kwok, R. (2000). "Recent changes in Arctic Ocean sea ice motion associated with the North Atlantic Oscillation". In: *Geophysical Research Letters* 27.6, pp. 775–778.

Kwok, R. and D. A. Rothrock (1999). "Variability of Fram Strait ice flux and North Atlantic oscillation". In: *Journal of Geophysical Research: Oceans* 104.C3, pp. 5177–5189.

Kwok, R. and N. Untersteiner (2011). "The thinning of Arctic sea ice". In: *Physics Today* 64.4, pp. 36–41.

Livingstone, C. E., K. P. Singh, and A. L. Gray (1987). "Seasonal and regional variations of active/passive microwave signatures of sea ice". In: *Geoscience and Remote Sensing, IEEE Transactions on* 2, pp. 159–173.

Lomax, A. S., D. Lubin, and R. H. Whritner (1995). "The potential for interpreting total and multiyear ice concentrations in SSM/I 85.5 GHz imagery". In: *Remote sensing of environment* 54.1, pp. 13–26.

Long, D. G. and D. L. Daum (1998). "Spatial resolution enhancement of SSM/I data". In: *Geoscience and Remote Sensing, IEEE Transactions on* 36.2, pp. 407–417.

Long, D. G., P. J. Hardin, and P. T. Whiting (1993). "Resolution enhancement of space-borne scatterometer data". In: *Geoscience and Remote Sensing, IEEE Transactions on* 31.3, pp. 700–715.

Markus, T. and D. J. Cavalieri (2000). "An enhancement of the NASA Team sea ice algorithm". In: *Geoscience and Remote Sensing, IEEE Transactions on* 38.3, pp. 1387–1398.

Markus, T., J. C. Stroeve, and J. Miller (2009). "Recent changes in Arctic sea ice melt onset, freezeup, and melt season length". In: *Journal of Geophysical Research: Oceans* 114.C12.

Maslanik, J. et al. (2007). "A younger, thinner Arctic ice cover: Increased potential for rapid, extensive sea-ice loss". In: *Geophysical Research Letters* 34.24.

Maslanik, J. et al. (2011). "Distribution and trends in Arctic sea ice age through spring 2011". In: *Geophysical Research Letters* 38.13.

Mathew, N., G. Heygster, and C. Melsheimer (2009). "Surface emissivity of the Arctic sea ice at AMSR-E frequencies". In: *Geoscience and Remote Sensing, IEEE Transactions on* 47.12, pp. 4115–4124.

Maykut, G. A. and N. Untersteiner (1971). "Some results from a time-dependent thermodynamic model of sea ice". In: *Journal of Geophysical Research* 76.6, pp. 1550–1575.

McLaren, A. S., M. Serreze, and R. Barry (1987). "Seasonal variations of sea ice motion in the Canada Basin and their implications". In: *Geophysical research letters* 14.11, pp. 1123–1126.

Melsheimer, C. et al. (2009). "Retrieval of sea ice emissivity and integrated retrieval of surface and atmospheric parameters over the Arctic from AMSR-E data". In: *Journal of the Remote Sensing Society of Japan* 29.1, pp. 236–241.

Mundy, C. and D. Barber (2001). "On the relationship between spatial patterns of sea-ice type and the mechanisms which create and maintain the North Water (NOW) polynya". In: *Atmosphere-Ocean* 39.3, pp. 327–341.

Nakawo, M. and N. K. Sinha (1981). "Growth rate and salinity profile of first-year sea ice in the high Arctic". In: *Journal of Glaciology* 27, pp. 315–330.

Neumann, G. and W. J. Pierson Jr (1966). *Principles of physical oceanography*. Englewood Cliffs, NJ (USA) Prentice Hall.

Nghiem, S. et al. (2006). "Depletion of perennial sea ice in the East Arctic Ocean". In: *Geophysical Research Letters* 33.17.

Nghiem, S. et al. (2007). "Rapid reduction of Arctic perennial sea ice". In: *Geophysical Research Letters* 34.19.

Notz, D. (2009). "The future of ice sheets and sea ice: Between reversible retreat and unstoppable loss". In: *Proceedings of the National Academy of Sciences* 106.49, pp. 20590–20595.

Onstott, R. G. et al. (1987). "Evolution of microwave sea ice signatures during early summer and midsummer in the marginal ice zone". In: *Journal of Geophysical Research: Oceans (1978–2012)* 92.C7, pp. 6825–6835.

Overland, J. et al. (2015). "The Melting Arctic and Midlatitude Weather Patterns: Are They Connected?*". In: *Journal of Climate* 28.20, pp. 7917–7932.

Peake, W. H. (1959). "Interaction of electromagnetic waves with some natural surfaces". In: *Antennas and Propagation, IRE Transactions on* 7.5, pp. 324–329.

Perovich, D. K. and A. J. Gow (1996). "A quantitative description of sea ice inclusions". In: *Journal of Geophysical Research: Oceans* 101.C8, pp. 18327–18343.

Perovich, D. K. and J. A. Richter-Menge (2009). "Loss of sea ice in the arctic". In: *Annual Review of Marine Science* 1, pp. 417–441.

Petrie, R. E., L. C. Shaffrey, and R. T. Sutton (2015). "Atmospheric response in summer linked to recent Arctic sea ice loss". In: *Quarterly Journal of the Royal Meteorological Society* 141.691, pp. 2070–2076.

Pickard, G. L. and W. J. Emery (1990). *Descriptive physical oceanography: an introduction*. Elsevier.

Rigor, I. G., J. M. Wallace, and R. L. Colony (2002). "Response of sea ice to the Arctic Oscillation". In: *Journal of Climate* 15.18, pp. 2648–2663.

Rott, H and T Nagler (1994). "Capabilities of ERS-1 SAR for snow and glacier monitoring in alpine areas". In: *Proceedings of the Second ERS-1 Symposium—Space at the Service of Our Environment*. Vol. 361. Hamburg, Germany: European Space Agency, pp. 965–965.

Serreze, M. C., R. G. Barry, and A. S. McLaren (1989). "Seasonal variations in sea ice motion and effects on sea ice concentration in the Canada Basin". In: *Journal of Geophysical Research: Oceans (1978–2012)* 94.C8, pp. 10955–10970.

Shokr, M. and T. A. Agnew (2013). "Validation and potential applications of Environment Canada Ice Concentration Extractor (ECICE) algorithm to Arctic ice by combining AMSR-E and QuikSCAT observations". In: *Remote Sensing of Environment* 128, pp. 315–332.

Shokr, M., K. Asmus, and T. A. Agnew (2009). "Microwave emission observations from artificial thin sea ice: the ice-tank experiment". In: *Geoscience and Remote Sensing, IEEE Transactions on* 47.1, pp. 325–338.

Shokr, M. and M. Dabboor (2013). "Interannual variability of young ice in the Arctic estimated between 2002 and 2009". In: *Geoscience and Remote Sensing, IEEE Transactions on* 51.6, pp. 3354–3370.

Shokr, M., A. Lambe, and T. Agnew (2008). "A new algorithm (ECICE) to estimate ice concentration from remote sensing observations: an application to 85-GHz passive microwave data". In: *Geoscience and Remote Sensing, IEEE Transactions on* 46.12, pp. 4104–4121.

Shokr, M. and N. Sinha (2015). *Sea Ice: Physics and Remote Sensing*. Hoboken, NJ, USA: John Wiley & Sons.

Shokr, M. E. and N. K. Sinha (1994). "Arctic sea ice microstructure observations relevant to microwave scattering". In: *Arctic* 47.3, pp. 265–279.

Shokr, M. E. and N. K. Sinha (1995). *Physical, electrical and structural properties of Arctic sea ice observed during SIMMS'92 experiment*. Research Report. Environment Canada, Atmospheric Environment Service.

Sorteberg, A. and B. Kvingedal (2006). "Atmospheric forcing on the Barents Sea winter ice extent". In: *Journal of Climate* 19.19, pp. 4772–4784.

Spencer, R. W., H. M. Goodman, and R. E. Hood (1989). "Precipitation retrieval over land and ocean with the SSM/I: Identification and characteristics of the scattering signal". In: *Journal of Atmospheric and Oceanic Technology* 6.2, pp. 254–273.

Spreen, G., L. Kaleschke, and G. Heygster (2008). "Sea ice remote sensing using AMSR-E 89-GHz channels". In: *Journal of Geophysical Research: Oceans (1978–2012)* 113.C2.

Spreen, G. et al. (2009). "Fram Strait sea ice volume export estimated between 2003 and 2008 from satellite data". In: *Geophysical Research Letters* 36.19.

Steele, J. H., S. A. Thorpe, and K. K. Turekian (2009). *Elements of physical oceanography: a derivative of the encyclopedia of ocean sciences*. Academic Press.

Steffen, K. and A. Schweiger (1991). "NASA team algorithm for sea ice concentration retrieval from Defense Meteorological Satellite Program special sensor microwave imager: Comparison with Landsat satellite imagery". In: *Journal of Geophysical Research: Oceans (1978–2012)* 96.C12, pp. 21971–21987.

Stogryn, A. (1987). "An Analysis of the Tensor Dielectnc Constant of Sea Ice at Microwave Frequencies". In: *Geoscience and Remote Sensing, IEEE Transactions on* 2, pp. 147–158.

Stroeve, J. et al. (2007). "Arctic sea ice decline: Faster than forecast". In: *Geophysical research letters* 34.9.

Stroeve, J. C. et al. (2012). "The Arctic's rapidly shrinking sea ice cover: a research synthesis". In: *Climatic Change* 110.3-4, pp. 1005–1027.

Sumata, H. et al. (2014). "An intercomparison of Arctic ice drift products to deduce uncertainty estimates". In: *Journal of Geophysical Research: Oceans* 119.8, pp. 4887–4921.

Sumata, H. et al. (2015). "Uncertainty of Arctic summer ice drift assessed by high-resolution SAR data". In: *Journal of Geophysical Research: Oceans* 120.8, pp. 5285–5301.

Svendsen, E et al. (1983). "Norwegian remote sensing experiment: Evaluation of the nimbus 7 scanning multichannel microwave radiometer for sea ice research". In: *Journal of Geophysical Research: Oceans (1978–2012)* 88.C5, pp. 2781–2791.

Svendsen, E., C. Matzler, and T. C. Grenfell (1987). "A model for retrieving total sea ice concentration from a spaceborne dual-polarized passive microwave instrument operating near 90 GHz". In: *International Journal of Remote Sensing* 8.10, pp. 1479–1487.

Swift, C., L. Fedor, and R. Ramseier (1985). "An algorithm to measure sea ice concentration with microwave radiometers". In: *Journal of Geophysical Research: Oceans (1978–2012)* 90.C1, pp. 1087–1099.

Talley, L. D. (2011). *Descriptive physical oceanography: an introduction*. Academic press.

Tonboe, R, S Andersen, and L Toudal (2003). *Anomalous winter sea ice backscatter and brightness temperatures*. Scientific Report. Danish Meteorological Institute. Copenhagen, Denmark.

Tschudi, M. et al. (2010). "Tracking the movement and changing surface characteristics of Arctic sea ice". In: *Selected Topics in Applied Earth Observations and Remote Sensing, IEEE Journal of* 3.4, pp. 536–540.

Tucker, W. et al. (1992). "Physical properties of sea ice relevant to remote sensing". In: *Microwave Remote Sensing of Sea Ice*. Ed. by F. D. Carsey. Wiley Online Library, pp. 9–28.

Ulaby, F. T., R. K. Moore, and A. K. Fung (1982). *Microwave remote sensing: active and passive, Vol. 2: Radar remote sensing and surface scattering and emission theory*. Addison-Wesley.

— (1986). *Microwave Remote Sensing Active and Passive, Vol. 3: From Theory to Applications*. Artech House, Inc.

Vihma, T. (2014). "Effects of Arctic Sea Ice Decline on Weather and Climate: A Review". In: *Surveys in Geophysics* 35.5, pp. 1175–1214.

Voss, S., G. Heygster, and R. Ezraty (2003). "Improving sea ice type discrimination by the simultaneous use of SSM/I and scatterometer data". In: *Polar Research* 22.1, pp. 35–42.

Wadhams, P. (2000). *Ice in the Ocean*. CRC Press.

Wang, H. et al. (2009). "Arctic multiyear ice concentration retrieval based on AMSR-E 89GHz data". In: *Chinese Journal of Polar Research* 21.3, pp. 186–196.

Wentz, F. J. and T. Meissner (2000). *AMSR Ocean Algorithm, Algorithm Theoretical Basis Document (ATBD), Version 2*. Technical Proposal 121599A-1. Santa Rosa, CA, USA.

Ye, Y. and G. Heygster (2015). "Arctic Multiyear Ice Concentration Retrieval from SSM/I Data Using the NASA Team Algorithm with Dynamic Tie Points". In: *Towards an Interdisciplinary Approach in Earth System Science: Advances of a Helmholtz Graduate Research School*. Ed. by G. Lohmann et al. Cham, Germany: Springer International Publishing Switzerland, pp. 99–108. DOI: `10.1007/978-3-319-13865-7_12`.

Ye, Y., G. Heygster, and M. Shokr (2015). "Improving multiyear ice concentration estimates with reanalysis air temperatures". In: *Geoscience and Remote Sensing, IEEE Transactions on*. DOI: `10.1109/TGRS.2015.2503884.`.

Ye, Y. et al. (2016). "Improving multiyear sea ice concentration estimates with sea ice drift". In: *Remote Sensing* 8.5, p. 397. DOI: `10.3390/rs8050397`.